Università degli Studi di Napoli "Federico II"

Facoltà di Scienze Matematiche Fisiche e Naturali

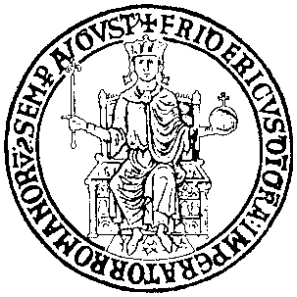

Tesi di Laurea Magistrale in Fisica

Study of $pp \to Z + X \to \mu^+\mu^- + X$ channel with the CMS detector at the LHC

Relatori
Ch.mo Prof. C. Sciacca

Ch.mo Dott. L. Lista

Candidata
Annapaola de Cosa
Matr. 358/65

Anno Accademico 2008/09

"The next reason that you might think you do not understand what I am telling you is , while I am describing to you *how* Nature works, you won't understand *why* Nature works that way. But you see, nobody undertands that. I can't explain why Nature behaves in this peculiar way.

[...] I'm going to describe to you how Nature is − and if you don't like it, that's going to get in the way of your understanding it. It's a problem that physicists have learned to deal with: they've learned to realize that whether or not the theory gives predictions that agree with experiment. It is not a question of whether or not a theory is philosophically delightful, or easy to understand, or perfectly reasonable from the point of view of common sense. The theory of quantum electrodynamics describes Nature as absurd from the point of view of common sense. And it agrees fully with experiment. So I hope you can accept Nature as She is − absurd.

I'm going to have fun telling you about this absurdity, because I find it delightful . Please don't turn yourself off because you can't believe Nature is so strange. Just hear me all out, and I hope you'll be as delighted as I am when we're through. "

Richard Feynman
QED, The strange Theory of Light and Matter

"−Cinquecento e un milione di che?− ripeté il piccolo principe che mai aveva rinunciato a una domanda una volta che l'aveva espressa. "

Antoine de Saint-Exupéry
Il piccolo principe

Contents

Introduction

This thesis presents a study of the inclusive production of the Z boson decaying in two muons in order to measure the inclusive cross section of the process $pp \rightarrow Z + X \rightarrow \mu^+\mu^- + X$ with the very first data taken at the Large Hadron Collider, LHC, with the Compact Muon Solenoid (CMS) experiment built at CERN (Centre Europeen pour la Rescherche Nucleaire) in Geneve. The Large Hadron Collider is a proton-proton collider which will accelerate proton beams up to a design energy of 7 TeV with a total centre of mass energy of 14 TeV and luminosity of $\mathcal{L} = 10^{34}\ cm^{-2}\ s^{-1}$. These features rapresent important challenges in physics accelerator technology and will open the search field of physics at the TeV scale. The goal of the LHC is to explore this range of high energy, never probed so far in a laboratory, in order to investigate behaviour of the Standard Model (SM), provide precision measurements in this sector, and search for new physics beyond the Standard Model. One of the main goals of the LHC and of the CMS experiment is the study the symmetry breaking mechanism giving rise to particle masses, in particular in the context of the Standard Model, and, hence, the search for the Higgs boson in the mass range 100 GeV/$c^2 < m_{\mathrm{H}} <$ 1 TeV/c^2 or look for alternative models.

The inclusive process analyzed in this thesis $pp \rightarrow Z + X \rightarrow \mu^+\mu^- + X$ has an high cross section, $\approx 2\ nb$, and a very clear signature provided by two isolated muons with high transverse momentum in the final state. It will be one of the first physics channels to be studied at the LHC from the early period of data-taking. An analysis of this channel will be useful for several reasons:

- it will provide a detector calibration tool and an extimate of the reconstruction efficiencies;

- being a well known electroweak channel, it will provide a validation of the Standard Model predictions at the TeV energy scale and it will be useful to unveil the potential presence of new physics at such energy range, such as triple neutral bosons couplings like ZZγ and Z$\gamma\gamma$, or the

existence of heavy neutral bosons (Z′) not predicted by the SM;

- from the start-up of the machine, it will provide a tool to monitor the LHC luminosity;
- in intermediate and high Higgs mass regions, the golden channel for Higgs boson observation is the Higgs boson decay into two Z and with four muons in the final state.

The purpose of this thesis is to complete the development and study of an entirly data-driven analysis model, in collaboration with the CMS Naples analysis group, in order to be ready to analyze first data taken at the LHC start-up. The analysis method is based on a simultaneous fit of the yield of $Z \rightarrow \mu^-\mu^+$ events and the average reconstruction muon efficiencies in the tracker and in the muon detector, together with the selection and trigger efficiencies without depending on Monte Carlo simulation estimates of these parameters. The fit strategy foresees a classification of events with at least one reconstructed $Z \rightarrow \mu^+\mu^-$ candidate in different categories. The yields of these samples are related in different ways to the efficiencies to determine. The Z peak shape model in each of these samples is not parametrized according to an empirical function, but is determined entirly from the data resulting in a reduction of fit parameters and uncertainties. I have completed this procedure within this work.

The *isolation* variable, defined as the sum of transverse momentum of tracks in the tracker, or as the sum of transverse energy of deposits in calorimeters, within a cone around the muon, is an useful parameter to discriminate muons coming from Z decay from background ones. In fact, muons coming from Z decay are isolated, i.e. they aren't accompained by nearby particles, differently from background muons. In this work of thesis I have investigated a new isolation variable which combines informations coming from the tracker and from the calorimeters. I have performed an optimization procedure in order to improve the background rejection. An event selection which considers a cut on this variable allows to achieve a greater rejection of the backgrounds, an increase of isolation efficiency, and, hence, a better signal to background ratio, with a subsequent decrease of statistical error of the the signal yield.

For the very first LHC data-taking, with few inverse picobarns of integrated luminosity, performing a least square fit could be quite difficult with very low sample statistics. For this reason, an Extended Unbinned Maximum Likelihood fit has been implemented in the final part of this work. This method allows to perform a good fit of parameters also in conditions of very low statistics.

In Chapter 1 an introduction to the Standard Model is presented with particular attenction to the Electroweak sector and the symmetry breaking mechanism.

After a brief description of the LHC machine, Chapter 2 reportes an overview of the CMS detector.

In Chapter 3 the physical purposes of the CMS experiment are presented. An introduction to Standard Model mesurements at CMS is reported together with a description of Higgs production mechanisms and decay channels at LHC and the search strategies for different mass ranges. The final part of the chapter deals with some aspects of physics beyond the Standard Model.

In Chapter 4 the analysis strategy is described in detail and the results of the test I performed on samples of different integrated luminosity are listed. Particular attention is made on muon isolation studies and on the performance of the new selection variable introduced. The last part of the chapter deals with the implementation of an Unbinned Maximum Likelihood fit for the analysis of the first few inverse picobarns of data.

Chapter 1

The Standard Model

The first evidence of the discrete nature of matter, just hypothesized by Democritus, was established after Mendeleev's studies of chemical properties of elements and their periodic behaviour according to the atomic weights. In the last two centuries the investigation of structure of matter has made progresses thanks to the improvement of the experimental techniques. That allowed a series of discoveries, such as the internal structure of atomic nuclei made of protons and neutrons. The description of matter became clearer in terms of elementary particles.

Thomson's discovery of electron and Maxwell's theory of electromagnetic field led to a modern view of the composition of matter, and of the forces. Electron is on one hand the source of the electromagnetic field through its electric charge, and, on the other, an elementary constituent of matter. Subsequently, with the discovery of two new forces, the *weak* and the *strong* forces, the search for more particle types was opened. A theory introduced in the late 1960's generalized the relationship between electron and electromagnetic field to the other force fields, treating particles that are constituents of matter (*fermions*, half-integer spin) and particles that are mediators of interactions (*bosons*, integer spin) with the same elegant formalism. This theory is a Quantum Field Theory known as Standard Model (SM). Today, the aim of particle physics is to try to identify these structurless units and to understand the nature of the fundamental forces acting among them.

1.1 The Standard Model

The development of particle accelerators allowed to design a simple as well as clearer picture of what are fundamental matter particles and what fundamental forces.

The elementary forces, responsible of the interaction among the particles, are four: gravity, weak interaction, electromagnetic interaction and strong interaction.

Fundamental matter particles known in nature are of two types : *leptons* and *quarks*. Both fermion types are arranged into three families each, three doublets associated to an isospin quantum number:

- Lepton doublets are constituted each by a charged particle interacting both electromagnetically and weakly – the electron e, the muon μ and the tau τ –, and by a neutral particle interacting only weakly – the electron neutrino ν_e, the muon neutrino ν_μ, the tau neutrino ν_τ.

- Quark doublets are composite each by a particle of charge $+\frac{2}{3}$ – up (u), charm (c), top (t) – and a particle of charge $-\frac{1}{3}$ – down (d), strange (s), bottom (b). The quarks interact via all three interactions: strong, electromagnetic and weak, differently from the charged leptons which do not interact via strong force and from neutral leptons which interact only weakly. The quarks are the costituents of hadrons, and are confined into them by the strong interaction.

	Families			**Charge**
Leptons	$\binom{\nu_e}{e}$	$\binom{\nu_\mu}{\mu}$	$\binom{\nu_\tau}{\tau}$	0 -1
Quarks	$\binom{u}{d}$	$\binom{c}{s}$	$\binom{t}{b}$	$+\frac{2}{3}$ $-\frac{1}{3}$

Table 1.1: Leptons and quarks generations.

A formal description of the three fundamental interactions (electromagnetic, weak and strong) can be given in terms of a gauge theory, in particular a description of the *strong interactions* can be provided by a gauge theory based on an $SU(3)_c$ symmetry group (see section 1.4), while an $SU(2)_L \otimes U(1)_Y$ gauge theory is associated to *weak* and *electromagnetic interactions.* The model which describes these interactions in terms of a gauge theory is known as the Standard Model (SM).

The SM provides the best description of the fenomenology of high energy particle interactions in the energy ranges probed up to now in laboratories. Its great success is due to the fact that its predictions are in very good agreement with experimental observations.

In the SM particle interactions arise from a *gauge principle*, i.e. the request of the invariance of the theory under a local gauge transformation. Force fields with their interactions are necessarily included by the introduction of a covariant derivative term in the Lagrangian to permit the local invariance.

Quantum Electrodynamics (QED), which describes electromagnetic interactions, derives from the imposition of gauge invariance under the symmetry group $U(1)_{em}$ involving the introduction of a Lagrangian term that couples the fermion field to the electromagnetic field. A generalization of this gauge invariance also underlies the theories of strong interactions (the *Quantum Chromodynamics*, QCD), generated by the symmetry group $SU(3)_c$, and electroweak interactions, generated by the symmetry group $SU(2)_L \otimes U(1)_Y$.

Matter particles interact in terms of exchange of quanta (*bosons*, integer spin) associated to the particular type of force. According to the quantum field theory, hence, particles interact by exchanging bosonic field quanta: the *gauge vector bosons*. These field quanta are identified as the *photon*, the $W^{\pm}$, the Z and the *gluons*:

- The photon is the mediator of electromagnetic interaction coupling to charged particles by a running coupling constant[1] α, which shows an increase with energy involved. The photon doesn't bring charge and it doesn't couple to neutral particles, like neutrinos. Moreover, it is massless, hence, the electromagnetic interaction has long range.

- The W^+, W^- and Z mediate the weak interactions, but unlike the photon, they are massive and the interaction is of short range type. It is noteworthy that while the photon doesn't carry charge, weak current are both charged and neutral.

- Strong forces are transmitted by the gluons, existing in 8 kinds. They couple with quarks and gluons. Unlike photon, the gluon brings "charge", the *color*, and it is possible a gluon selfcoupling. The running coupling strength α_s for strong interactions decreases with raising of the energy (we will see this feature in more details in the Section 1.4).

The electromagnetic and weak interactions were unified succesfully under a theory developed by Glashow[3], Weinberg[4] and Salam[5]: the Electroweak

[1] α is the electromagnetic coupling constant which runs with the momentum transfer due to a phenomenon called *polarization of the vacuum*. This running constant it is defined by:
$\alpha(Q^2) = \frac{\alpha}{[1-(\frac{\alpha}{3\pi})ln(\frac{Q^2}{Am^2})]}$, for $Q^2 \gg m^2$ and with Q^2=-q^2, where q is the transferred momentum and A=exp$\frac{5}{3}$.

Theory generated by the symmetry group $SU(2)_L \otimes U(1)_Y$. We will see this part of the SM in more details in the following section.

The first experimental confirmation of the Standard Model of electroweak interactions was the observation of neutral weak currents predicted by the theory. The discovery was made in 1973 at CERN using the Gargamelle bubble chamber exposed to a neutrino beam[2][1]. It was followed by a more direct confirmation occurred with the realization of a proton-antiproton collider at CERN with the discover of the W and Z bosons[2], the mediators of weak force, by the collaborations UA1 and UA2 in 1983.

A crucial point of SM is the presence of heavy particles. This implies a mass term destroying the gauge invariance, hence only massless particles have to appear in the Lagrangian. Peter Higgs, in 1964, introduced the "Higgs mechanism"[10] that allows vector bosons to acquire mass through the spontaneous symmetry breaking. This mechanism predicts the presence of a new scalar particle, the *Higgs boson*, whose coupling provides the vector boson masses as well as fermion ones. The Higgs boson is still undetected and its direct observation is one of the main goals of the LHC.

1.2 The Electroweak Theory

1.2.1 The GWS Theory

In a letter addressed to the group of "Radioactives"[11], in the winter 1930, Pauli suggested an interesting hypothesis solving the problem of the apparently lack of energy conservation in β decay. He explained the anomalus continuous spectrum observed in terms of emission of a neutral particle together with the electron (or positron). According to Pauli, the energy difference between the initial and final nucleus, that are well defined states, was shared by the two particles together. This neutral fermionic massless particle was given tha name *neutrino*.

From the neutrino hypothesis of Pauli, Fermi formulated the first quantum field theory for the weak process $\mathrm{n} \rightarrow \mathrm{p} + \mathrm{e}^- + \overline{\nu_e}$ (β decay) as a four point interaction described by the Lagrangian:

$$\mathscr{L} = \frac{G_F}{\sqrt{2}} \left[\overline{\psi}_e \gamma^\alpha (1-\gamma^5)\psi_{\nu_e}\right] \left[\overline{\psi}_p \gamma_\alpha (1-\gamma^5)\psi_n\right] \tag{1.1}$$

where the term $(1-\gamma^5)$ has been included later to take into account parity violation discovered later[12]. This form for current-current interaction is

[2]Neutrino and antineutrino beams were used in the experiment. The occurrence of events with only hadrons in the final states, i.e without muons or electrons, demonstrated the existence of neutral weak current.

called V – A (Vectorial minus Axial). The current structure V – A is the same for quarks and leptons. It indicates a form of "universality" of weak interactions.

Electromagnetic and weak interactions were described together in a unified way by Glashow basing on the symmetry group $SU(2)_L \otimes U(1)_Y$[3]: the *Electroweack theory* (EW). Building on Glashow's work, Weinberg[4] and Salam[5], indipendently, introduced the Higgs mechanism of the spontaneous breaking symmetry in the theory by adding to the Lagrangian a scalar potential that generates the vector boson and fermion masses in a gauge invariant way.

Looking at the leptonic transitions associated with the weak charged current, a particular structure of the lepton pairs emerges: they are regarded as *doublets* under the weak $SU(2)$ group, and the quarks show a similar structure (this is another evidence of the universality feature of the theory). Since the generators of fundamental representation of $SU(2)$ are the Pauli matrices, it is possible to adopt the same formalism as for the angular momentum. In the weak $SU(2)$ group a *weak isospin* quantum number T is associated to the leptonic fields:

$$T = \frac{1}{2}: \quad \begin{cases} T_3 = +1/2 \\ T_3 = -1/2 \end{cases} \quad L_e = \begin{pmatrix} \nu_e \\ e \end{pmatrix}_L \quad L_\mu = \begin{pmatrix} \nu_\mu \\ \mu \end{pmatrix}_L \quad L_\tau = \begin{pmatrix} \nu_\tau \\ \tau \end{pmatrix}_L , \tag{1.2}$$

where $e_L = \frac{1}{2}(1-\gamma_5)e$ is the left-handed component of the leptonic field. The same holds for μ and τ. At present, there is no evidence for any weak interactions coupling to right-handed field components, and it is a basic assumption of the electroweak theory that all 'R' components are singlets under $SU(2)$ group[3]:

$$T = 0: \qquad e_R \qquad \mu_R \qquad \tau_R \qquad \nu_{e\ R} \qquad \nu_{\mu\ R} \qquad \nu_{\tau\ R}\ . \tag{1.3}$$

For the quark fields the doublets are:

$$T = \frac{1}{2}: \qquad \begin{cases} T_3 = +1/2 \\ T_3 = -1/2 \end{cases} \qquad \begin{pmatrix} u_L \\ d'_L \end{pmatrix} \qquad \begin{pmatrix} c_L \\ s'_L \end{pmatrix} \qquad \begin{pmatrix} t_L \\ b'_L \end{pmatrix} \tag{1.4}$$

It is noteworthy that d', s', b' are a superposition of strong interaction eigenstates d, s, b given by CKM matrix (Cabibbo 1963[15], Kobayashi and Maskawa 1973[16]).

[3]The right-handed neutrinos are not involved in the interaction, since their quantum numbers are null.

Right quark components are also singlets as well as lepton ones:

$$T = 0 : \qquad u_R \qquad d_R \qquad s_R \qquad c_R \qquad b_R \qquad t_R \ . \tag{1.5}$$

The standard EW Lagrangian can be splitted into two parts: one involving fermions and gauge bosons, $\mathcal{L}_{\text{symm}}$, and one involving Higgs boson couplings, $\mathcal{L}_{\text{Higgs}}$:

$$\mathcal{L} = \mathcal{L}_{\text{symm}} + \mathcal{L}_{\text{Higgs}} \ . \tag{1.6}$$

Gauging an abelian theory consists of extending the global invariance of the Lagrangian density under $U(1)$ transformation group to a local invariance. According to Yang and Mills[17], this procedure can be applied to every continuous transformation group. The invariance of EW Lagrangian under local $SU(2)_L \otimes U(1)_Y$ transformation is recovered by replacing the ordinary derivative by the covariant derivative through the introduction of four gauge fields: W^i_μ $(i = 1, 2, 3)$ associated to $SU(2)_L$, and B_μ associated to $U(1)_{\text{Y}}$.

$$D_\mu = \partial_\mu + ig\frac{\boldsymbol{\tau}}{2}\mathbf{W}_\mu + i\frac{g'}{2}Y_W B_\mu \ . \tag{1.7}$$

In the Dirac Lagrangian:

$$\mathcal{L} = \bar{\psi}(i\partial\!\!\!/ - m)\psi \tag{1.8}$$

$\partial\!\!\!/$ has, therefore, to be replace by the covariant derivative $D\!\!\!/$:

$$\mathcal{L} = \bar{\psi}(iD\!\!\!/ - m)\psi \ . \tag{1.9}$$

The Dirac field can be expressed in terms of chirality eigenstate components[4] ψ_L and ψ_R. Right and left-handed components have different quantum numbers, hence, the mass term, which couples them in the Lagrangian, involves a breaking of gauge invariance:

$$\bar{\psi}(\mathrm{i}D\!\!\!/ - m)\psi = \bar{\psi}_L \mathrm{i}D\!\!\!/\psi_L + \bar{\psi}_R \mathrm{i}D\!\!\!/\psi_R - m(\bar{\psi}_L\psi_R + \bar{\psi}_R\psi_L) \ . \tag{1.10}$$

Neglecting the mass term of fermions and bosons the local invariance of the theory is preserved, and right and left components are treated indipendently. Fermion and boson masses will be introduced later in a gauge invariant way through the Higgs mechanism.

[4]The left-handed component ψ_L is given by the operation of the projection operator P_L on the field, and ψ_R by the projector P_R:

$$P_{\text{L}} = \left(\frac{1-\gamma^5}{2}\right) \qquad P_{\text{R}} = \left(\frac{1+\gamma^5}{2}\right) \ .$$

The fermionic Lagrangian describes the interaction of massless fermionic fields among them and with the gauge fields:

$$\mathcal{L}_{\text{fermionic}} = \sum_f \bar{\psi} i \not{D} \psi \ . \tag{1.11}$$

$\mathcal{L}_{\text{fermionic}}$ results to be invariant under rotations in weak isospin space:

$$SU(2)_L : \qquad \begin{cases} L_f \to e^{-ig\frac{\boldsymbol{\tau}}{2}\cdot\boldsymbol{\alpha}(x)} L_f \\ R_f \to R_f \end{cases} \ . \tag{1.12}$$

The right-handed fermionic components do not interact with gauge fields introduced within the Lagrangian by the covariant derivative, but they are sensitive to a local U(1) transformation:

$$U(1)_Y : \quad \begin{cases} L_f \to e^{-ig'\frac{Y}{2}\cdot\boldsymbol{\beta}(x)} L_f \\ R_f \to e^{-ig'\frac{Y}{2}\cdot\boldsymbol{\beta}(x)} R_f \end{cases} \ . \tag{1.13}$$

The abelian field $U(1)_Y$ is associated to a *weak ipercharge* Y, as well as the non abelian $SU(2)_L$ is associated to the *weak isospin* T. The relation between T and Y was extablished by the Gell-Mann-Nishijima relation:

$$Q = T_3 + \frac{Y}{2} \ , \tag{1.14}$$

where Q is the electric charge in units of e. Two different coupling constant g and g', were introduced correspondy respectively to $SU(2)_L$ and $U(1)_Y$, since the transformations under the two groups are indipendent.

In order to have the Lagrangian (1.9) invariant, the transformations of fermionic fields (1.12) and (1.13) must to be coupled to the gauge fields trasformations:

$$W^i_\mu(x) \to W' i_\mu(x) = W^i_\mu(x) - \partial_\mu \alpha^i(x) - g\epsilon^{ijk}\alpha_j(x) W_{k\mu}(x) \ , \tag{1.15}$$

$$B_\mu(x) \to B'_\mu(x) = B_\mu(x) - \partial_\mu \beta(x) \ . \tag{1.16}$$

The trasformations for the gauge fields W^i_μ is more complex than that for B_μ field, due to the non-abelian properties of the $SU(2)_L$ group. The additional term in the (1.15) is responsible for the self-interactions of $SU(2)_L$ gauge fields and also for the inclusion of the last term in strenght field tensor (1.33). We will see how this feature reappears in QCD Section 1.4.

In corrispondence to this invariance, four currents are preserved on three for $SU(2)_L$ and one for $U(1)_Y$: two charged currents and two neutral currents.

Coming back to the covariant derivative, it can be written so below:

$$iD_\mu = i\partial_\mu - \underbrace{g(W_\mu^1 T^1 + W_\mu^2 T^2)}_{charged\ current\ contribution} - \underbrace{gT^3 W_\mu^3 - g'\frac{Y}{2}B_\mu}_{neutral\ current\ contribution} \quad . \tag{1.17}$$

It is clear that R components couple also to neutral currents. The second term describes the electromagnetic field interaction A_μ and a new field Z_μ, both neutrals. It's convenient to perform an orthogonal transformation:

$$W_3^\mu = \sin\theta_W A^\mu + \cos\theta_W Z^\mu \ , \tag{1.18a}$$
$$B^\mu = \cos\theta_W A^\mu - \sin\theta_W Z^\mu \ , \tag{1.18b}$$

to produce the physical vector fields for $\mathrm{W}^\pm$, Z and photon:

$$Z^\mu = -\sin\theta_W B^\mu + \cos\theta_W W_3^\mu \ , \tag{1.19}$$

$$A^\mu = \cos\theta_W B^\mu + \sin\theta_W W_3^\mu \ , \tag{1.20}$$

$$\mathrm{W}^\pm{}_\mu = \frac{1}{\sqrt{2}}(\mathrm{W}_\mu^1 \pm i\mathrm{W}_\mu^2) \ , \tag{1.21}$$

where the mixing angle θ_W is known as the Weinberg angle, defined as:

$$cos\theta_W = \frac{g}{\sqrt{g^2 + g'^2}} \qquad \sin\theta_W = \frac{g'}{\sqrt{g^2 + g'^2}} \tag{1.22}$$

The interaction term of the Lagrangian due to the coupling with W_μ^3 and B_μ fields can be rewritten in terms of physical field Z_μ and A_μ according to (1.19) and (1.20) through the Weinberg angle. According to the Gell-Mann-Nishijima relation, the electromagnetic current can be expressed as the sum of weak isospin current and weak hypercharge current:

$$J_\mu^{em} = J_\mu^W + \frac{J_\mu^Y}{2} \ . \tag{1.23}$$

We demand that the gauge field A_μ is the electromagnetic field coupled to electric charges through the term $J_{em}^\mu A_\mu$. This yields a relation among the electromagnetic charge, the two coupling constants, g and g', and the Weinberg angle:

$$e = g\sin\theta_W = g'\cos\theta_W \ . \tag{1.24}$$

The fermionic Lagrangian term is now complete; it splits in a free Lagrangian term and an interaction part with gauge vector bosons:

$$\mathcal{L}_{\text{fermionic}} = \mathcal{L}_{\text{free}} + \mathcal{L}_{\text{int}} \ , \tag{1.25}$$

where $\mathcal{L}_{\text{free}}$ is given by:

$$\mathcal{L}_{\text{free}} = \sum_f \bar{\psi} i \not{\partial} \psi \ . \tag{1.26}$$

The interaction term is:

$$\mathcal{L}_{\text{int}} = \mathcal{L}_{\text{w}}^{\text{charged}} + \mathcal{L}_{\text{w}}^{\text{neutral}} + \mathcal{L}_{\text{int}}^{\text{e.m}} \ , \tag{1.27}$$

where the first term is:

$$\mathcal{L}_{\text{w}}^{\text{charged}} = -\frac{g}{2\sqrt{2}}[J^{\mu+} W_{\mu}^{-} + J^{\mu-} W_{\mu}^{+}] \ , \tag{1.28}$$

the second one is given by:

$$\mathcal{L}_{\text{w}}^{\text{neutral}} = -\frac{g}{\cos\theta_W}[J_3^{\mu} - \sin^2\theta_W J_{em}^{\mu}] Z_{\mu} \ , \tag{1.29}$$

and the last term can be expressed as:

$$\mathcal{L}_{\text{int}}^{\text{e.m}} = -e J_{em}^{\mu} A_{\mu} \ . \tag{1.30}$$

In order to complete the dynamics we need to build the kinematic terms for vector bosons. We define a strength field tensor, $B_{\mu\nu}$, related to the gauge field B_{μ}:

$$B_{\mu\nu} = \partial_{\mu} B_{\nu} - \partial_{\nu} B_{\mu} \ . \tag{1.31}$$

In analogy to electromagnetic case, the kinematic term is:

$$\mathcal{L}_B = -\frac{1}{4} B_{\mu\nu} B^{\mu\nu} \ . \tag{1.32}$$

The strength field tensor associated to gauge fields $\mathbf{W}_{\mu}$ is given by the equation:

$$F_{\mu\nu}^{\alpha} = \partial_{\mu} W_{\nu}^{\alpha} - \partial_{\nu} W_{\mu}^{\alpha} - g\epsilon^{\alpha\beta\gamma} W_{\mu}^{\beta} W_{\nu}^{\gamma} \ , \tag{1.33}$$

and the correspondly Lagrangian density is:

$$\mathcal{L}_W = -\frac{1}{4} \mathbf{F}_{\mu\nu} \mathbf{F}^{\mu\nu} \ . \tag{1.34}$$

We obtain the $SU(2)_L \otimes U(1)_Y$ gauge invariant Lagrangian:

$$\mathcal{L}_{\text{symm}} = \sum_f \bar{\psi} \text{i} \not{D} \psi - \frac{1}{4} B_{\mu\nu} B^{\mu\nu} - \frac{1}{4} \mathbf{F}_{\mu\nu} \mathbf{F}^{\mu\nu} \tag{1.35}$$

where the sum is done over all fundamental fermions, f.

1.2.2 Spontaneous broken local $SU(2)_L \otimes U(1)_Y$ symmetry

In order to preserve the Lagrangian invariance, fermionic and bosonic masses have been neglected, but the theory has to describe the fact that $W^{\pm}$ and Z have masses around 100 GeV, and that, as a consequence, weak interactions have short range. It is therefore necessary to introduce a new term that coherently represents the masses of the particles, and at the same time, preserves the gauge principle. The spontaneous symmetry breaking mechanism allows to generate such term by postulating the existence of a new scalar field doublet. The Higgs boson field is written as an $SU(2)$ doublet with two scalar components:

$$\Phi = \begin{pmatrix} \phi^+ \\ \phi^0 \end{pmatrix} \equiv \begin{pmatrix} \frac{1}{\sqrt{2}}(\phi_1 + i\phi_2) \\ \frac{1}{\sqrt{2}}(\phi_3 + i\phi_4) \end{pmatrix} \tag{1.36}$$

The Lagrangian for such boson includes a potential which is responsible of the symmetry breaking mechanism[5]:

$$\mathcal{L}_{\text{Higgs}} = (D^\mu \Phi)^\dagger D_\mu \Phi - V(\Phi) = (D^\mu \Phi)^\dagger D_\mu \Phi - \mu^2 \Phi^\dagger \Phi - \lambda (\Phi^\dagger \Phi)^2 \tag{1.37}$$

By requiring that $\mu^2 < 0$ and $\lambda > 0$, the minimum of the potential is not unique anymore, but it is located on a continuous ring on a complex plane, as seen in Figure 1.1. An easier form of scalar potential can be choosen appling an isotopic spin transformation:

$$\Phi = \begin{pmatrix} 0 \\ \phi(x) \end{pmatrix} \tag{1.38}$$

with ϕ(x) real. It can see that the degree of freedom in the Higgs field that are removed by this transformation can be absorbed into three longitudinal degrees of freedom of the new massive bosons.

There is therefore a degree of freedom for the choice of Higgs vacuum expectation value (v.e.v). The choice suggested by Weinberg was:

$$\Phi = \frac{1}{\sqrt{2}} \begin{pmatrix} 0 \\ v/\sqrt{2} \end{pmatrix} \tag{1.39}$$

where

$$v = \sqrt{-\mu^2/\lambda}\ . \tag{1.40}$$

[5]When energy minimum is not unique and invariant under symmetry group transformation but different configurations of minimum exist, it is said that the symmetry is spontaneously broken.

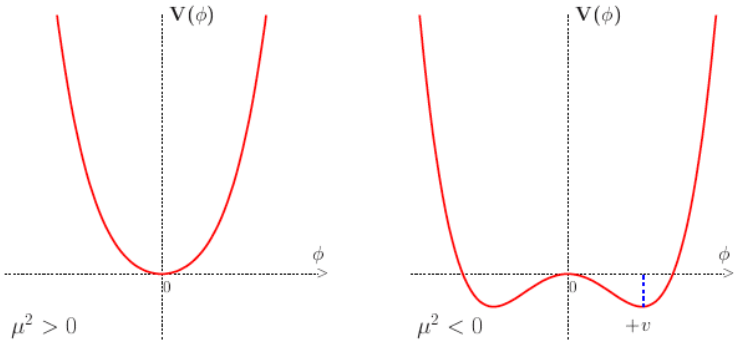

Figure 1.1: The potential V of the scalar field ϕ in the case of $\mu^2 > 0$, on the left. On the right the Higgs potential described from the last two terms of equation (1.37) with $\mu^2 < 0$ and $\lambda > 0$. The potential minimum is not unique, in the latter case, but there is an infinite number of mimimum points located on a continuous ring.

We consider also the oscillations about (1.39):

$$\Phi = \frac{1}{\sqrt{2}} \begin{pmatrix} 0 \\ v + H(x) \end{pmatrix} \ , \tag{1.41}$$

$v/\sqrt{2}$ is the Higgs (three level) vacuum expectation value and H(x) is the fluctuation around the minimum. After breaking symmetry there are three massive gauge bosons (rather than three massless bosons as assumed up to now) and one massless gauge boson.

The covariant derivative (1.7) acts on Φ, so one obtains:

$$\begin{aligned} (D^\mu \Phi)^\dagger D_\mu \Phi = & \frac{1}{2} \partial^\mu H \partial_\mu H + \\ & \frac{1}{8}(v+H)^2 g^2 (W^{1\mu} + iW^{2\mu})(W^1_\mu - iW^2_\mu) + \\ & \frac{1}{8}(v+H)^2 (g' B^\mu - g W^{3\mu})(g' B_\mu - g W^3_\mu) \ . \end{aligned} \tag{1.42}$$

The Lagrangian of the sector consisting of the gauge fields and the Higgs is:

$$\begin{aligned} \mathcal{L}_{G\Phi} &= \mathcal{L}_{\text{gauge}} + \mathcal{L}_{\text{Higgs}} \\ &= -\frac{1}{4} W_i^{\mu\nu} W^i_{\mu\nu} - \frac{1}{4} B^{\mu\nu} B_{\mu\nu} + (D^\mu \Phi)^\dagger D_\mu \Phi - \mu^2 \Phi^\dagger \Phi - \lambda (\Phi^\dagger \Phi)^2 \ . \end{aligned} \tag{1.43}$$

Replacing W_3^μ and B^μ by the physical fields Z^μ and A^μ, from (1.19) and from (1.20), and neglecting the quadratic terms, (1.43) can be rewritten as:

$$\begin{aligned}
\mathcal{L}_{G\Phi} &= \frac{1}{2}\partial^\mu H \partial_\mu H - \mu^2 H^2 && (1.44)\\
&\quad -\frac{1}{4}(\partial_\mu W_{1\nu} - \partial_\nu W_{1\mu})(\partial_\mu W_1^\nu - \partial_\nu W_1^\mu) + \frac{1}{8}g^2 v^2 W_{1\mu} W_1^\mu && (1.45)\\
&\quad -\frac{1}{4}(\partial_\mu W_{2\nu} - \partial_\nu W_{2\mu})(\partial_\mu W_2^\nu - \partial_\nu W_2^\mu) + \frac{1}{8}g^2 v^2 W_{2\mu} W_2^\mu && (1.46)\\
&\quad -\frac{1}{4}(\partial_\mu Z_\nu - \partial_\nu Z_\mu)(\partial_\mu Z^\nu - \partial_\nu Z^\mu) + \frac{1}{8}(g^2 + g'^2) v^2 Z_\mu Z^\mu && (1.47)\\
&\quad -\frac{1}{4}(\partial_\mu A_\nu - \partial_\nu A_\mu)(\partial_\mu A^\nu - \partial_\nu A^\mu) && (1.48)
\end{aligned}$$

where from (1.44) the mass of the Higgs boson is

$$m_{\mathrm{H}} = \sqrt{2}\mu = \sqrt{2\lambda}v \ . \tag{1.49}$$

The second term in (1.45) and (1.46) has exactly the form of a mass term for the W_1 and W_2 fields, since the W mass can be defined as:

$$m_{\mathrm{W}} = \frac{1}{2}gv \ , \tag{1.50}$$

while (1.47) gives the mass of the Z as

$$m_{\mathrm{Z}} = \frac{1}{2}v\sqrt{g^2 + g'^2} = \frac{m_{\mathrm{W}}}{\cos\theta_W} \tag{1.51}$$

From (1.48) it is clear that the photon remains to be massless, the symmetry $U(1)_{em}$ remains unbroken under the gauge subgroup generated by the electric charge.

Equations (1.50) and (1.51) bind the boson masses to θ_W and the parameter v, which is related to the Fermi constant G_F by the relation[6]:

$$v^2 = \frac{1}{\sqrt{2}G_F} \backsimeq (246\ \mathrm{GeV})^2 \ . \tag{1.52}$$

A theoretic prediction was given about Z and W boson masses as function of the three parameters $\alpha = e^2/4\pi$, G_F and $\sin^2\theta_W$. The latter was initially

[6]The relation between v and G_F comes out imposing the equality between transition amplitude according to Fermi theory and the form of Weinberg Salam model. Hence v is determined directly by the Fermi constant.

measured by neutrino-electron scattering and, later, with higher precision at the e^+ e^- collider LEP. Theoretical predictions of boson masses revealed a perfect agreement with experimental data of the SppS collider and LEP collaborations at CERN[2][13], and also with CDF and D0 at Fermilab[14], confirming the predictive power of the GWS model.

The Higgs mass value depends not only on v, the minimum value of Higgs potential, but also on the field selfcoupling constant λ. The latter has to be determined experimentally, and this uncertainty does not permit a prediction of the Higgs mass. It is, nevertheless, possible to extabilish some theoretical and experimental limits on this value as it will be shown later.

1.2.3 Fermionic masses

In order to complete the Electro Weak Lagrangian, another term has to be added: $\mathcal{L}_{\text{Yukawa}}$, that introduces fermionic masses. As explaind before, a mass term such as that in (1.10) breaks the gauge invariance, therefore it has to be removed, and fermion masses, such as boson masses, must be included through the alternative mechanism seen in the previous paragraph.

It is interesting to see how it is possible to produce a gauge invariant mass term by introducing a Yukawa coupling between fermions and the Higgs field, the same doublet (1.41) that gave raise to the Z and W boson mass:

$$\mathcal{L}_{\text{Yukawa}} = -\sum_f g_f(\bar{\psi}_L^f \Phi \psi_R^f + \bar{\psi}_R^f \Phi^\dagger \psi_L^f) \ . \tag{1.53}$$

Consider the electron, for example, and hypothesize such a coupling between the electron-type $SU(2)_L$ doublet in (1.2), the weak electron singlet in (1.5) and the Higgs doublet in Φ (1.41). This leads to the Yukawa term for the electron:

$$\mathcal{L}^e_{\text{Yukawa}} = -g_e(\bar{L}_e \Phi R_e + \bar{R}_e \Phi^\dagger L_e) \tag{1.54}$$

The two $SU(2)_L$ doublets L_e and Φ are dotted together is as to form an $SU(2)_L$ scalar, which multiplies the $SU(2)_L$ scalar right-handed component. In this way, (1.54) is invariant under $SU(2)_L \otimes U(1)_Y$ transformation preserving the gauge invariance of such term. Inserting the vacuum value of the field Φ and considering the oscillations about the v.e.v. (1.41) into (1.54), we obtain a Dirac mass term and the coupling between the Higgs boson and the electron which is proportional to the electron mass:

$$\mathcal{L}^e_{\text{Yukawa}} = -g_e \frac{v}{\sqrt{2}}(\bar{e}_L e_R + \bar{e}_R e_L) - g_e \frac{H}{\sqrt{2}}(\bar{e}_L e_R + \bar{e}_R e_L) \ . \tag{1.55}$$

This term is a Dirac mass term as in (1.10), and it allows to identify the electron mass:

$$m_e = g_e \frac{v}{\sqrt{2}} \ . \tag{1.56}$$

The mass term for the electron, and in general for all fermions, are proportional to the Yukawa coupling. The second term, the Higgs boson coupling to fermions, is proportional to the fermions' mass:

$$g_{\mathrm{H\ ee}} = i \frac{m_e}{v} \ . \tag{1.57}$$

This approach be applied to the *up* component of the $SU(2)_L$, i.e. for the $T_W^3 = +\frac{1}{2}$ component such as neutrinos and quarks u, c, and t. We need to consider also the coupling with the charge conjugate of Φ:

$$\Phi_C = i\tau_2 \Phi^* = \begin{pmatrix} \bar{\Phi}^0 \\ -\Phi^- \end{pmatrix} \ , \tag{1.58}$$

and the corresponding vacuum expectation value:

$$\Phi_C = \frac{1}{\sqrt{2}} \begin{pmatrix} v + H(x) \\ 0 \end{pmatrix} \ . \tag{1.59}$$

Taking this into account, the Lagrangian with quark mass terms can be written as:

$$\begin{aligned} \mathcal{L}_{\mathrm{Yukawa}}^{\mathrm{quarks}} &= \frac{g_q}{\sqrt{2}} - \left[(u_{i,L}, d_{i,L}) \begin{pmatrix} v + H \\ 0 \end{pmatrix} u_{i,R} + u_{i,R} (v + H, 0) \begin{pmatrix} u_{i,L} \\ d_{i,L} \end{pmatrix} \right] \\ &= \frac{g_q}{\sqrt{2}} (v + H)(u_{i,L} u_{i,R} + u_{i,R} u_{i,L}) \end{aligned} \ , \tag{1.60}$$

where $u_i = (u, c, t)$, $d_i = (d, s, b)$. The mass terms have the same form as (1.56), but with a different coupling constant, depending on the quark type, or in general fermion type.

It is clear that the Higgs mechanism solves the problem of the non-invariance of the Lagrangian in the presence of a mass term with the introduction of the Higgs field by means of the spontaneous broken symmetry mechanism. In this way it is possible to give mass to the vector bosons Z and W, but also to all fermions[7]. Nevertheless, the Yukawa coupling doesn't come from a gauge principle and, hence, is not possible to predict the Higgs mass, that

[7] We will not consider, in this thesis work, the terms relative to neutrino masses and their coupling to the Higgs field.

is a free parameter of the theory, since the constant λ is undefined. Also the fermion masses that depend on Higgs-fermion Yukawa couplings g_f are undefined, although they are well determined from experimental data. This means that the Yukawa coupling is a phenomenological model and not a predictive theory. The use of high energy colliders, like Tevatron at Fermilab, and in the near future of LHC at CERN, an experimental evidence confirming or not the existence of Higgs boson is expected.

1.3 The Higgs Sector

The *unbroken* Standard Model is described in a very elegant way by the gauge field theory based on $SU(2)_L \otimes U(1)_Y$ symmetry group, and all interactions are determined by the gauge priciple as a function of just two parameters: g and g'. This model doesn't take into account fermionic and bosonic masses, particles are considered to be massless. The Higgs mechanism brings back to the reality of a world where leptons, quarks and intermediate vector bosons have mass, and does it in a universal way throught the existence of the Higgs scalar field. Three massless Goldstone bosons are generated and absorbed as third polarization component (longitudinal part) of $\mathrm{W}^{\pm}$ and Z giving them mass. The remaining component of the complex doublet is the Higgs boson. This fundamental scalar particle is still undetected, and there is no prediction about its mass, m_{H}, due to the indetermination of the self-coupling constant λ. A Yukawa-like coupling of fermions to the Higgs field provides mass to leptons and quarks, and the interaction strength is proportional to fermion masses themselves. The SM Higgs boson couplings to fermions, gauge bosons and Higgs boson itself are given by[18] (Figure 1.2):

$$g_{\mathrm{H}f\bar{f}} = \frac{m_f}{v}; \tag{1.61}$$

$$g_{\mathrm{H}VV} = \frac{2m_V^2}{v}, \qquad g_{\mathrm{HH}VV} = \frac{2m_V^2}{v^2}; \tag{1.62}$$

$$g_{\mathrm{HHH}} = \frac{3m_{\mathrm{H}}^2}{v}, \qquad g_{\mathrm{HHHH}} = \frac{3m_{\mathrm{H}}^2}{v^2}. \tag{1.63}$$

where $V = \mathrm{W}^{\pm}$, Z.

Also if Higgs boson has eluded direct observation at the present, both theoretical and experimental constraints on m_H value are inferred.

1.3.1 Theoretical constraints on the Higgs boson mass

Theoretical constraints on m_{H} emerge from requests such as unitary, or from evaluations about perturbativity of the Higgs self-coupling, but also from the

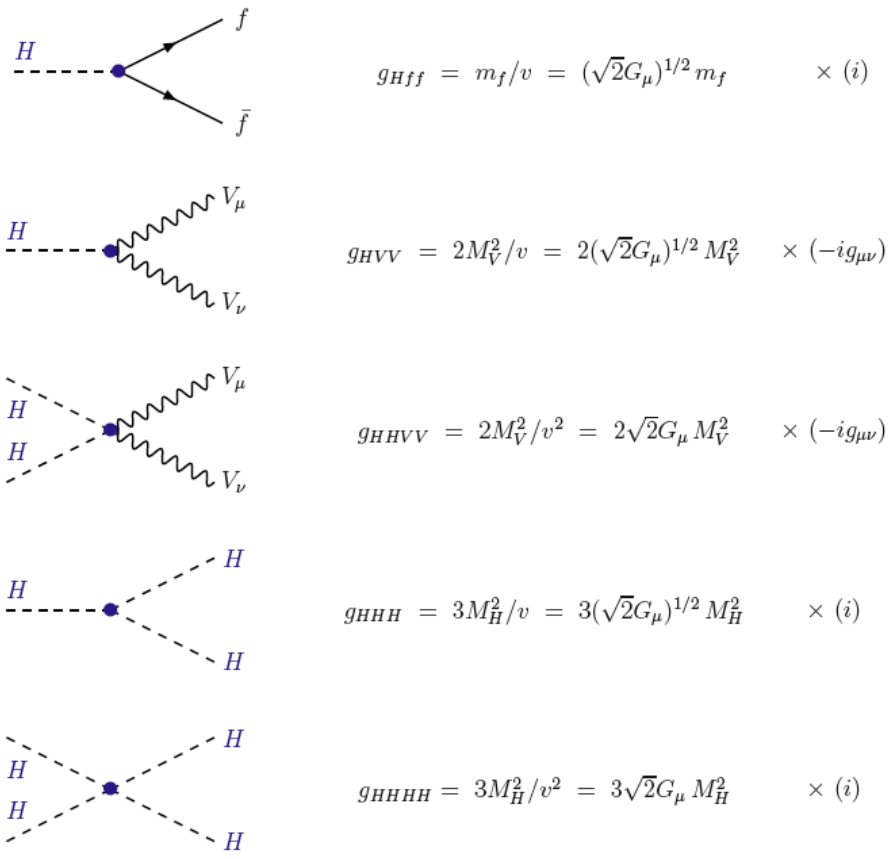

Figure 1.2: The Higgs boson couplings to fermions and gauge bosons and the Higgs self-couplings in the Standard Model.

request of vaccum state stability. These bounds depend on an energy cut-off Λ_C, over which new physics is expected.

Like other coupling constants of renormalizable theory, also λ runs with energy. Looking at the one-loop radiative corrections to the Higgs boson quartic coupling (Figure 1.3) and considering only the Higgs contribution (a top loop should also be taken into account), $\lambda(Q^2)$ shows a dependence on the energy scale Q according to the following expression:

$$\lambda(Q^2) = \frac{\lambda(v^2)}{1 - \frac{3}{4\pi^2}\lambda(v^2)\log\frac{Q^2}{v^2}} \tag{1.64}$$

Hence, there is a logaritmic dependence on the squared energy scale Q^2. At a scale much lower than the weak scale ($Q^2 \ll v^2$), the quartic coupling becomes extremally small, $\lambda(Q^2)$ vanishes leading to a non-interacting theory. If $Q^2 \gg v^2$, i.e. at energy much greater than the scale v, the quartic couplings grows to infinity (like QED running coupling constant). The energy cut-off Λ_C, below which the self-coupling λ remains finite, is:

$$\Lambda_C = v\,\exp\left(\frac{2\pi^2}{3\lambda}\right) = v\,\exp\left(\frac{4\pi^2 v^2}{3M_{\mathrm{H}}^2}\right) \tag{1.65}$$

At $\Lambda_C \backsim 10^{16}$ GeV, m_{H} is expected to be less than 200 GeV/c^2. In turn, at smaller cut-off values, $\Lambda_C \backsim 10^3$ GeV, the upper limit in Higgs mass value is around 1 TeV. This scale corresponds to the non-perturbative regime.

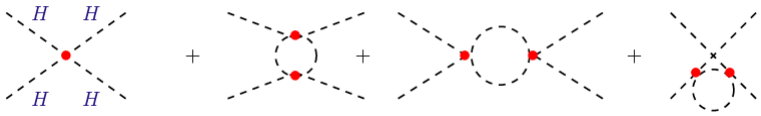

Figure 1.3: Higgs boson quartic coupling and one loop radiative corrections.

Up to now only the Higgs self-coupling has been included. In order to complete the frame it is necessary to take also into account fermion and boson contributions. Since the coupling involving the Higgs particle and fermions or gauge bosons is proportional to the particle masses, at least top quark, $\mathrm{W}^{\pm}$ and Z contributions must be considered. These additional terms change the scale at which new physics appears. There is in particular a strict dependence on top quark mass[19].

For small values of λ, the top quark contribution could determine a negative value of $\lambda(Q^2)$. In order to have vacuum state stability, it is necessary to

keep a positive value of $\lambda(Q^2)$; therefore, we impose the constraints on m_{H} to be larger than a certain value which is proportional to squared top mass and depends on the cut-off scale value Λ_C.

The upper and lower bounds on the Higgs mass described above are known, as *triviality* and *vacuum stability* respectively. Figure 1.4 illustrates these limits as a function of the cut-off energy scale Λ_C at which new physics is expected. In particular, if the new physics scale is about 1 TeV, the Higgs boson mass is expected to lie within the interval:

$$50 \text{ GeV}/c^2 \lesssim m_{\mathrm{H}} \lesssim 800 \text{ GeV}/c^2 \tag{1.66}$$

while, requiring the SM to be valid up to the Grand Unification scale, i.e. the energy scale at which a unification of strong, electromagnetic and weak interactions is expected, $\Lambda_{\mathrm{GUT}} \backsim 10^{16} GeV$, the Higgs mass should belong to the range:

$$130 \text{ GeV}/c^2 \lesssim m_{\mathrm{H}} \lesssim 180 \text{ GeV}/c^2 \tag{1.67}$$

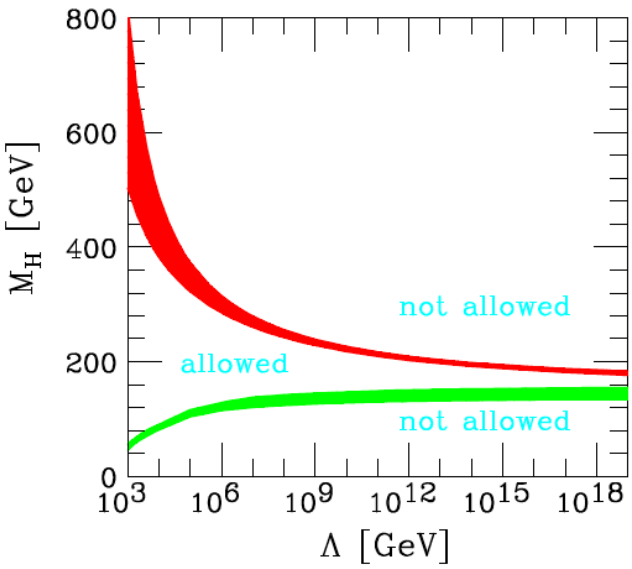

Figure 1.4: The triviality bound (upper limit) and the vacuum stability bound (lower limit) to the Higgs boson mass as a function of the cut-off scale Λ_C. Above, the cut-off scale Λ is the scale at which the SM is no longer able to describes the known physics, and new physics is therefore expected.

Although the theory cannot predict the exact value of Higgs boson mass, it can impose some constraints and, hence, determine limits of the range in which it lies. As it was explained before, this limits depend on the energy scale Λ_C above which Standard Model has to be replaced by an other theory describing a new phenomenology.

1.3.2 Experimental constraints on Higgs boson mass

Bounds on the Higgs mass are also provided by direct searches of Higgs bosons and, indirectly, by precision measures led at hadron coliders.

Precision electroweak measurements are sensitive to radiative corrections which depend logarithmically on m_{H}. This allows to estimate a confidence interval about the value through a combined fit of the electroweak parameters. The SM is assumed to be the correct theory, the Higgs boson mass is left as a free parameter.

For instance, the radiatively-corrected value for the mass of $\mathrm{W}^{\pm}$ can be expressed as:

$$m_{\mathrm{W}}^2 = \frac{\pi\alpha/\sqrt{2}G_F}{\sin^2\theta_W(1-\Delta r)} \tag{1.68}$$

where Δr includes the radiative corrections related to α, G_F, m_{Z} and m_{W}. Δr depends on the running coupling constant $\alpha(m_{\mathrm{Z}})$, quadratically on top quark mass (due to the loop $t-b$ correction) and logarithmically in $\mathrm{M_H}$. Experiments at Tevatron measured the top mass[19]. Hence, radiative corrections to the $\mathrm{W}^{\pm}$ mass, and also to the other parameter contemplated by the SM, depends only on m_{H}, as is the only unknown parameter.

Figure 1.6 shows $\Delta\chi^2 = \chi^2 - \chi^2_{min}$ as a function of m_{H}. Measurements from the four LEP collaborations, ALEPH, DELPHI, L3 and OPAL and from the SLD experiment at the Stanford Linear Collider, are collected (Figure 1.5) and a global fit is performed on them, reported on the plot in Figure 1.6.

Taking into account all the precision electroweak data (Figure 1.5) one obtains, by minimizing $\Delta\chi^2$, the value of the most likely SM Higgs boson mass to be:

$$m_{\mathrm{H}} = 114^{+69}_{-45}\ \mathrm{GeV}/c^2 \tag{1.69}$$

with an upper limit (at the 95 % Confidence Level) in the SM of:

$$m_{\mathrm{H}} < 260\ \mathrm{GeV}/c^2 \tag{1.70}$$

At LEP2 the direct search for the Higgs bosons has been extended at centre of mass (CM) energies up to 209 GeV looking for the Higgs-stralhung production process, where the electron-positron pair annihilates into a virtual

Quantity	Value	Standard Model	Pull	Dev.
m_t [GeV]	$170.9 \pm 1.8 \pm 0.6$	171.1 ± 1.9	-0.1	-0.8
M_W [GeV]	80.428 ± 0.039	80.375 ± 0.015	1.4	1.7
	80.376 ± 0.033		0.0	0.5
M_Z [GeV]	91.1876 ± 0.0021	91.1874 ± 0.0021	0.1	-0.1
Γ_Z [GeV]	2.4952 ± 0.0023	2.4968 ± 0.0010	-0.7	-0.5
Γ(had) [GeV]	1.7444 ± 0.0020	1.7434 ± 0.0010	–	–
Γ(inv) [MeV]	499.0 ± 1.5	501.59 ± 0.08	–	–
$\Gamma(\ell^+\ell^-)$ [MeV]	83.984 ± 0.086	83.988 ± 0.016	–	–
$\sigma_{\rm had}$ [nb]	41.541 ± 0.037	41.466 ± 0.009	2.0	2.0
R_e	20.804 ± 0.050	20.758 ± 0.011	0.9	1.0
R_μ	20.785 ± 0.033	20.758 ± 0.011	0.8	0.9
R_τ	20.764 ± 0.045	20.803 ± 0.011	-0.9	-0.8
R_b	0.21629 ± 0.00066	0.21584 ± 0.00006	0.7	0.7
R_c	0.1721 ± 0.0030	0.17228 ± 0.00004	-0.1	-0.1
$A_{FB}^{(0,e)}$	0.0145 ± 0.0025	0.01627 ± 0.00023	-0.7	-0.6
$A_{FB}^{(0,\mu)}$	0.0169 ± 0.0013		0.5	0.7
$A_{FB}^{(0,\tau)}$	0.0188 ± 0.0017		1.5	1.6
$A_{FB}^{(0,b)}$	0.0992 ± 0.0016	0.1033 ± 0.0007	-2.5	-2.0
$A_{FB}^{(0,c)}$	0.0707 ± 0.0035	0.0738 ± 0.0006	-0.9	-0.7
$A_{FB}^{(0,s)}$	0.0976 ± 0.0114	0.1034 ± 0.0007	-0.5	-0.4
$s_\ell^2(A_{FB}^{(0,q)})$	0.2324 ± 0.0012	0.23149 ± 0.00013	0.8	0.6
	0.2238 ± 0.0050		-1.5	-1.6
A_e	0.15138 ± 0.00216	0.1473 ± 0.0011	1.9	2.4
	0.1544 ± 0.0060		1.2	1.4
	0.1498 ± 0.0049		0.5	0.7
A_μ	0.142 ± 0.015		-0.4	-0.3
A_τ	0.136 ± 0.015		-0.8	-0.7
	0.1439 ± 0.0043		-0.8	-0.5
A_b	0.923 ± 0.020	0.9348 ± 0.0001	-0.6	-0.6
A_c	0.670 ± 0.027	0.6679 ± 0.0005	0.1	0.1
A_s	0.895 ± 0.091	0.9357 ± 0.0001	-0.4	-0.4
g_L^2	0.3010 ± 0.0015	0.30386 ± 0.00018	-1.9	-1.8
g_R^2	0.0308 ± 0.0011	0.03001 ± 0.00003	0.7	0.7
$g_V^{\nu e}$	-0.040 ± 0.015	-0.0397 ± 0.0003	0.0	0.0
$g_A^{\nu e}$	-0.507 ± 0.014	-0.5064 ± 0.0001	0.0	0.0
A_{PV}	$(-1.31 \pm 0.17) \cdot 10^{-7}$	$(-1.54 \pm 0.02) \cdot 10^{-7}$	1.3	1.2
Q_W(Cs)	-72.62 ± 0.46	-73.16 ± 0.03	1.2	1.2
Q_W(Tl)	-116.4 ± 3.6	-116.76 ± 0.04	0.1	0.1
$\frac{\Gamma(b\to s\gamma)}{\Gamma(b\to X c l \nu)}$	$\left(3.55^{+0.53}_{-0.46}\right) \cdot 10^{-3}$	$(3.19 \pm 0.08) \cdot 10^{-3}$	0.8	0.7
$\frac{1}{2}(g_\mu - 2 - \frac{\alpha}{\pi})$	$4511.07(74) \cdot 10^{-9}$	$4509.08(10) \cdot 10^{-9}$	2.7	2.7
τ_τ [fs]	290.93 ± 0.48	291.80 ± 1.76	-0.4	-0.4

Figure 1.5: SM parameters[9], with relative pull, in the EWK fit to the Higgs mass.

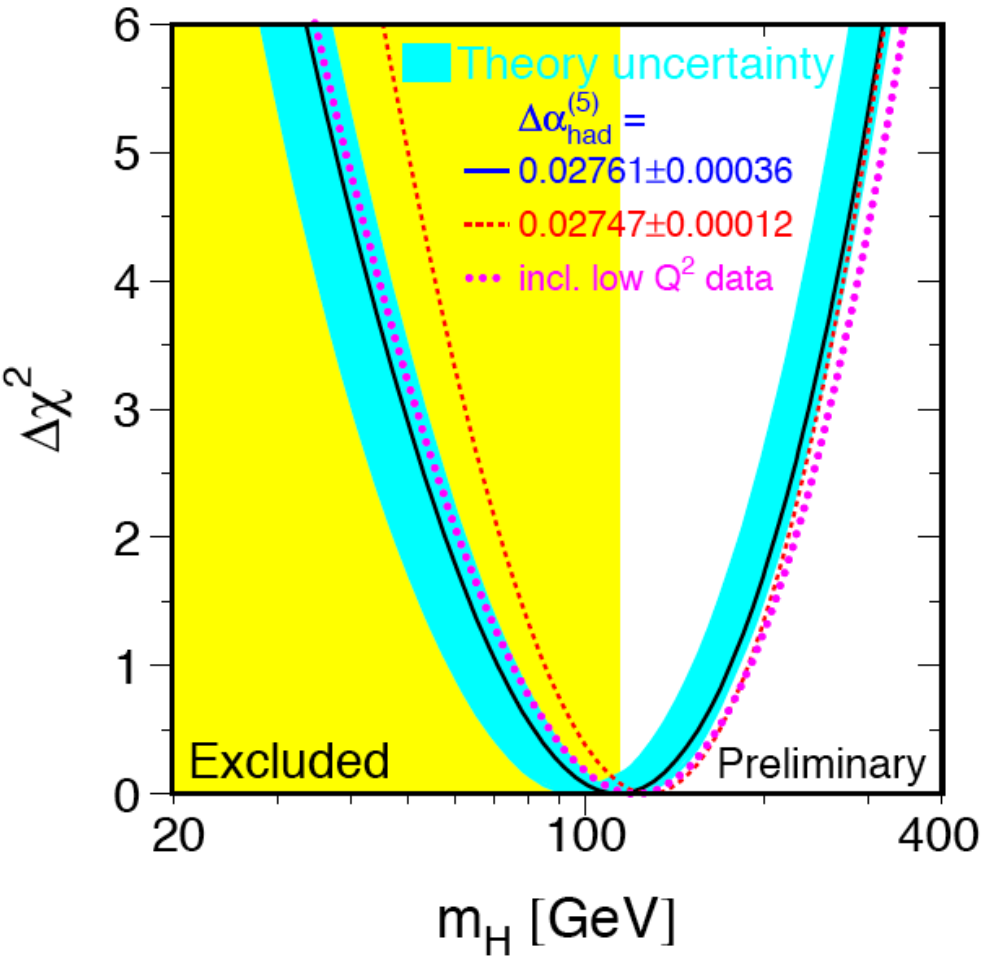

Figure 1.6: The χ^2 of the fit to the electro-weak precision data as function of m_{H}. The continuos line results from high energy precision measurement. The blue band takes into account theoretical uncertainties, caused by neglecting higher order corrections. The yellow region is excluded by direct searches at LEP.

Z which then splits into a Higgs particle and a real Z. This process has the highest cross section. At LEP energies, the Higgs boson and the Z were expected to be observed through their decay products. The decay channel that have been studied at LEP are:

$$\mathrm{HZ} \to \mathrm{b\bar{b}}q\bar{q} \quad , \mathrm{HZ} \to \mathrm{b\bar{b}}\nu\bar{\nu} \quad , \mathrm{HZ} \to \mathrm{b\bar{b}}\ell\bar{\ell} \quad , \mathrm{HZ} \to \tau^-\tau^+\mathrm{b\bar{b}} \quad .$$

The combination of results from all four collaborations at LEP of the direct search for the Higgs boson production led to a lower limit at 95% of confidence level to the Higgs mass:

$$m_{\mathrm{H}} > 114 \text{ GeV}/c^2 \tag{1.71}$$

Preliminary results on direct searches for a SM Higgs Boson in p $\overline{\mathrm{p}}$ collisions at the Fermilab Tevatron accelerator at $\sqrt{s} = 1.96$ TeV have been presented recently (March 2009). CDF and DØ experiments performed a search for the Higgs boson in the following channels:

$$\mathrm{HW} \to \mathrm{b\bar{b}}\tau^-\nu \ , \ \mathrm{HV} \to \mathrm{b\bar{b}}\tau^-\tau^+/\tau^-\tau^+jj \ , \ \mathrm{HV} \to \mathrm{b\bar{b}}jj \ , \ \tau^-\tau^+\mathrm{H} \to \tau^-\tau^+\mathrm{b\bar{b}} \ ,$$

where V=$\mathrm{W}^{\pm}$,Z. These direct searches have further extended the mass region excluded at 95 % C.L. for a SM Higgs, adding the exclusion of the range 160 GeV/$c^2 < m_{\mathrm{H}} <$ 170 GeV/c^2[20] (Figure 1.7).

1.4 Quantum Chromodynamics

Quantum Chromodynamics[21][22], QCD, is a non-abelian gauge field theory describing strong interactions among quarks and gluons.

The first theoretical evidence of the presence of a new degree of freedom, later called *color*, emerged by looking at Δ^{++} spectroscopy to preserve the anti-symmetry of its (and in general of all baryons, since they must obey to the Pauli exclusion principle) wavefunction with the introduction of another term to baryon wavefunction: the antisymmetric *color wavefunction*. This feature of strong interactions was soon confirmed by some experimental evidences such as the measure of the ratio R[23][24][25][26]:

$$R = \frac{\sigma(\mathrm{e^-e^+} \to hadrons)}{\sigma(\mathrm{e^-e^+} \to \mu^-\mu^+} \ . \tag{1.72}$$

According to the quark parton model should be equal to the sum of all quark couplings to the photon:

$$R = \sum_a e_a^2 \ . \tag{1.73}$$

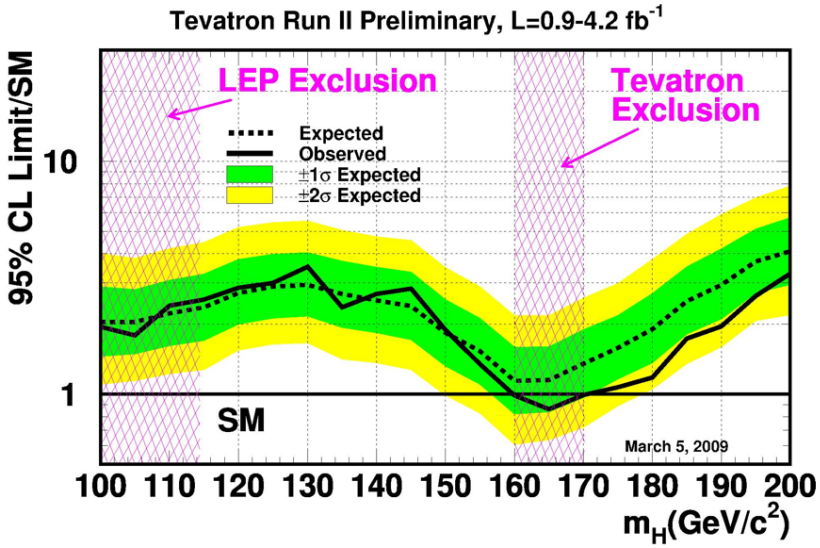

Figure 1.7: Observed and expected 95 % C.L. upper limits on the ratios of the Higgs production cross section and the SM cross section, as a function of the Higgs boson mass for the combined CDF and DØ analyses. Both experiments performed dedicated searches in different channels.

This would give $R = \frac{11}{9}$ and not $R = \frac{11}{3}$, that is the due value in the presence of color. The factor 3 confirms the existence of this further degree of freedom. This is only one of the confirmations of the presence of color.

An interesting feature of strong interaction is the apparently changing in its effective strength with the kinematic regime, which becomes quite weak at short distance or at high energy. This property is known as *asymptotic freedom*. In such regime, lowest-order perturbation theory amplitudes provide a good qualitative description of the phenomenology. The running coupling constant[8)] $\alpha_s(Q^2)$, as consequence, becomes larger at lower energies and strong enough to lead to the *confinement* of quarks and gluons into hadrons. At low energies, perturbation theory breaks down.

The simplest gauge theory describing strong interaction features, such as the non observation of color multiplet of hadronic state, or the apparent non existence of $q\ q$, $\overline{q}\ q\ q$ or $q\ q\ q\ q\ q$ states, is based on the $SU(3)$ group.

QCD is formulated in an analogous way as QED and the theory of weak interactions by a gauge principle. Strong iteractions involve quarks, which are present in three color eigenstates. The free strong Lagrangian is:

$$\mathcal{L}_{\rm QCD}^{\rm free} = \bar{\psi}_{q,a}(i\partial\!\!\!/ - m)\psi_{q,a} \ , \tag{1.75}$$

where $\alpha = 1, 2, 3$ is the color index (red, blue, green) and f is the quark flavour index. For simplicity, we will refer to just one quark flavour in the following. The QCD Lagrangian is required to be invariant under an $SU(3)_C$ transformation

$$\psi \rightarrow \psi' = e^{-ig_s \boldsymbol{\alpha}(x)\frac{\boldsymbol{\lambda}}{2}}\psi \ , \tag{1.76}$$

where $\boldsymbol{\lambda} = (\lambda_1, \lambda_2, .., \lambda_8)$ is a vector of the SU(3) generators, i.e. the Gell Mann matrices, $g_s = \sqrt{4\pi\alpha_s}$. The following commutation rules hold for Gell-Mann matrices:

$$\left[\frac{\lambda_a}{2}, \frac{\lambda_b}{2}\right] = i f_{abc}\frac{\lambda_c}{2} \ , \tag{1.77}$$

where f_{abc} are real constants, called structure constants of the group. The non commutation of all the generators is due to the group being non-abelian.

In order to preserve the invariance under local tranformation, the ordinary derivative has to be replaced by the covariant one, containing eight gluon

[8]The strong running coupling constant is defined by:

$$\alpha_s(Q^2) = \frac{\alpha_s(\mu^2)}{[1 + \frac{\alpha_s}{12\pi}(33 - 2f)ln(\frac{Q^2}{\mu^2})]} \ , \tag{1.74}$$

where f is the flavor number and μ is a reference mass scale. The positive sign in the denominator is responsable of the decreasing of $\alpha_s(Q^2)$ with energy.

fields, G^a_μ :

$$D_\mu = \partial_\mu + i\frac{g_s}{2}\lambda_a G^a_\mu \ . \tag{1.78}$$

Replacing $\partial_\mu \to D_\mu$ in (1.75), we obtain the QCD Lagrangian, complete of a free term and of an interaction term:

$$\mathcal{L}_{\text{QCD}} = \bar{\psi}(i\partial\!\!\!/ - m)\psi - g_s\bar{\psi}\gamma^\mu\frac{\lambda_a}{2}\psi G^a_\mu \tag{1.79}$$

Although this form is the analogue of QED Lagrangian, it does not show a gauge invariance under $SU(3)$ transformation, since it is a non-abelian one. Each field G^a_μ has to transform as:

$$G^a_\mu \to G'^a_\mu = G^a_\mu - \partial_\mu\alpha^a - g_s f^{abc}\alpha_b G_{c\mu} \tag{1.80}$$

The last term is quadratic in gluon fields and produces a self-interaction term. This term arises also in weak interaction theory (Equation 1.15), but not in QED, because it is a characteristic of non-Abelian symmetries, such as $SU(3)$ or $SU(2)$. A gauge invariant kinetic energy term for each gluon field has to be added. The complete QCD Lagrangian takes the form:

$$\mathcal{L}_{\text{QCD}} = \bar{\psi}(i\partial\!\!\!/ - m)\psi - g_s\bar{\psi}\gamma^\mu\frac{\lambda_a}{2}\psi G^a_\mu - \frac{1}{4}G^a_{\mu\nu}G^{\mu\nu}_a \tag{1.81}$$

with the $G^a_{\mu\nu}$, the gluon field tensor defined as:

$$G^a_{\mu\nu} = \partial_\mu G^a_\nu - \partial_\nu G^a_\mu - g_s f^{abc}G_{\mu b}G_{\nu c} \tag{1.82}$$

1.5 The quark parton model

The internal hadron structure can be investigated through deep inelastic scattering of electron or neutrinos on a nucleon. This kind of experiment has firstly evidenced the non-pointlike nature of hadrons and the existence of fundamendal constituents.

Feynman introduced the parton model in 1969[28] explaining the deep inelastic scattering in terms of elastic scattering in free point-like constituents, the *partons*. At high transferred momentum the virtual photon is probing very short distances and time scales. In this scenario, the partons can be treated as free inside the hadron, and the photon interacts only with one parton (*asymptotic freedom*) which carries a fraction x of the total hadron's 4-momentum (Figure 1.8). The probability distribution of this variable is called Parton Distribution Function (PDF), and it is not predicted by the model. The PDFs are measured by to inelastic scattering experiments and

describe the distribution of quarks inside the nucleon. Two types of quarks have to be considered inside the nucleon: "valence" quarks (elementary constituents of the quark model) and " sea" quarks (virtually created $q\,\overline{q}$ pairs). Quark distributions have to be parametrized for valence and sea quarks. Nucleons, gluons and anti-quarks only have the "sea" contribution.

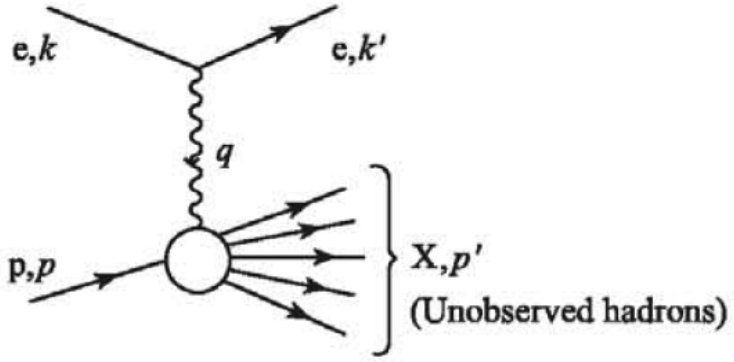

Figure 1.8: Inelastic electron-proton scattering, within one-photon exchange approssimation, in terms of interaction of the photon with a parton.

PDFs depends on the transferred momentum Q^2. Of course the assumed perturbative approssimation is valid for large four-momentum transfer, hence for low Q^2 the PDFs extracted experimentally are affected by larger uncertainties.

According to the quark parton model, the collision between two protons, like the ones that will be produced at the Large Hadron Collider, can be schematically presented as the interaction between two partons of momenta x_1p_1 and x_2p_2 respectively, p_1 and p_2 being the colliding protons momenta, and it takes place at centre-of-mass energy $\sqrt{s} = \sqrt{x_1x_2s}$, where s is centre-of-mass energy of the two protons system (Figure 1.9).

1.5.1 The Drell-Yan process

According to the parton model, we can interpret p-p collisions in terms of subprocesses between elementary constituents of the nucleons. The most important process is the Drell Yan process p p $\rightarrow \mu^-\ \mu^+$ X in which a muons pair is produced in association to an hadronic final state (Figure 1.9). At the tree-level approximation a valence quark and a sea antiquark annihilate into

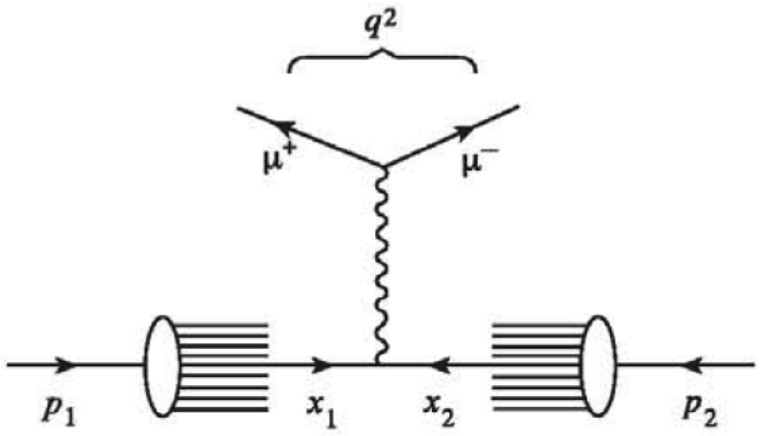

Figure 1.9: Parton model ampltude for Drell Yan process.

a virtual photon decaying in a muon pairs. The subprocess to consider is:

$$q\overline{q} \rightarrow \mu^-\mu^+ \ . \tag{1.83}$$

The cross section for this process can be computed in analogy to that of electron positron annihilation in muon-antimuon:

$$\sigma(\mathrm{e}^-\mathrm{e}^+ \rightarrow \mu^-\mu^+) = 4\pi\alpha^2/3q^2 \ . \tag{1.84}$$

Above the electron and muon masses are neglected. The cross section for the collision of a $q\ \overline{q}$ pair of quark type a with charge e_a (in units of the electric charge), assuming a given color charge, is then:

$$\sigma(q\overline{q} \rightarrow \mu^-\mu^+) = (4\pi\alpha^2/3q^2)e_a^2 \ . \tag{1.85}$$

The elementary process cross section has to be multiplied by the probabilities of finding a quark of type a with a x_1 fraction momentum, and an antiquark of the same type with a x_2 fraction momentum in the colliding protons:

$$dP_a(x_1, x_2) = q_a(x_1)dx_1\overline{q}_a(x_2)dx_2 \ . \tag{1.86}$$

We have to consider also the contribution due to an antiquark with x_1 fraction momentum and to a quark with x_2:

$$dP'_a(x_1, x_2) = q_a(x_2)dx_2\overline{q}_a(x_1)dx_1 \ . \tag{1.87}$$

The double differential cross section for Drell Yan process is then:

$$d^2\sigma(\mathrm{pp} \to \mu^-\mu^+ X) = \frac{4\pi\alpha^2}{9q^2} \sum_a e_a^2 [q_a(x_1)\overline{q}_a(x_2) + q_a(x_2)\overline{q}_a(x_1)] dx_1 dx_2 \ . \tag{1.88}$$

The factor $\frac{1}{3}$ takes into account the color of the quarks and the fact that particles are color-singlets implies that quark and antiquark have opposite color charge. The experimental observation of this process was one of the first experimental evidences for the presence of this new degree of freedom.

This cross section considers only the electrodynamic process with one photon exchange, but other diagrams must also be added, such as that with one Z boson exchange (Figure 1.10). This contribution cannot be neglected at high energies.

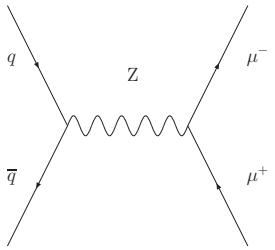

Figure 1.10: Annihilation $q\ \overline{q}$ in $\mu^-\ \mu^+$ pair through Z boson exchange.

Chapter 2

The Large Hadron Collider and the CMS experiment

The Standard Model of particle physics provides an accurate as well as elegant treatment of the penomenology and it has been so far tested to high precision at energy scale well below the TeV. However, it doesn't explaine some features such as the origin of the mass, that is up to now an unsolved problem. This has led to project a new accelerator able to investigate SM at an energy range above that probed so far in laboratories, in order to find answers about the electroweak breaking symmetry and to explore possible new physics beyond the Standard Model.

The Large Hadron Collider, build at CERN (Conseil Europen pour la Recherche Nuclaire)[32], has been thought to provide a test of SM also at energy up to the TeV as well as to search an experimental evidence of Higgs boson, which would confirm the Higgs hyphotesis of spontaneous breaking symmetry mechanism as origin of the mass. It has also the role to look for evidences of other phenomenology supporting theories such as supersymmetry or technicolor.

2.1 The LHC collider

The Large Hadron Collider (LHC)[29][30][31] is an accelerator and collider built at CERN and located in the already existing LEP tunnel on the the Swiss-French border, at about 100 m depth underground. It has a 27 km circumference.

The proton collisions will take place up to 7 TeV per beam with a total centre mass energy of 14 TeV. Proton beams will have a bunch-crossing frequence of 40 MHz, that corresponds to a time interval between two bunches

of 25 ns. The choice to project a pp collider rather than an e^-e^+ one allows to reach high energy without great loss due to synchroton radiation (proportional to the fourth inverse power of mass of accelerated particles). Moreover accelerating proton instead of antiproton is technically easier, and at LHC energy there are high propability density also for sea quark and antiquark.

Proton bunches cirtulate in two rings guided by high field superconducting magnets (up to 8.4 T) that are cooled by a huge cryogenics system.

To reach 7 TeV, the proton beams have to be pre-accelerate by existing machines. The protons are provided by an hydrogen source removing electrons and accelerated at 50 MeV by Linac, linear accelerator, hence put in a booster to reach 1.4 GeV. The bunches are formed and accelerated to 26 GeV in the Proton Synchroton (PS) with the correct 25 ns spacing ad then are injected into the Super Proton Synchroton (SPS) that accelerates them at 450 GeV and transferred into the two rings of LHC. Figure 2.1 shows an overview of CERN Accelerator Complex.

Proton beams will collide in four interaction points (IP), at which four detectors are installed: **CMS** (Compact Muon Solenoid)[34], **ATLAS** (A Toroidal LHC ApparatuS)[35], **LHCb** (Large Hadron Collider Beauty experiment)[36], and **ALICE** (A Large Ion Collider Experiment)[37]. CMS and ATLAS are the two largest experiments based on general purpose detectors, designed to explore the largest possible range of physics. ALICE is designed to study heavy ion physics and is an ion-ion collision experiment, it works with the collisions of two beams of Pb ions accelerated up to total energy of 2.76 TeV/nucleon. LHCb is designed to investigate the B-physics and precision measurment of CP violation, in order to do this, it doesn't work in the pp centre of mass system. One of the most important parameter of an accelerator is the istantaneous *luminosity* related to the total cross section σ of the two beam collisions and to the event rate R by the relation:

$$R = \mathcal{L}\sigma$$

$\mathcal{L}$ depends on machine parameters according to

$$\mathcal{L} = \frac{\gamma f k_B N_p^2}{4\pi\epsilon_n\beta} F$$

where γ is the Lorentz factor of the accelerated protons, f is the beam revolution frequency, k_B is the number of bunches per beam, N_p is the number of protons per bunch, ϵ_n is the normalized transverse emittance[1], β is the betatron function at the IP, and F a the reduction factor due to the crossing angle. The design luminosity for LHC is $\mathcal{L} = 10^{34} cm^{-2} s^{-1}$, leading to

[1]The design value of the emittance is 3.75 μ m

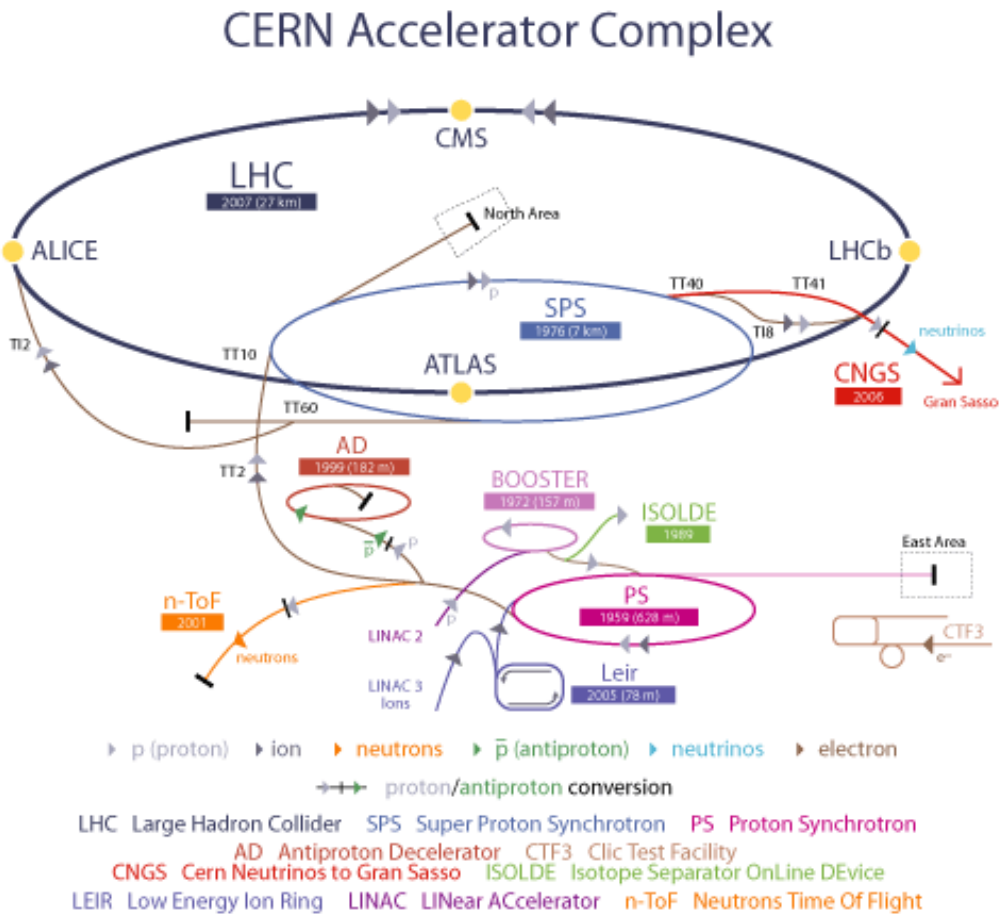

Figure 2.1: Overview of the CERN Accelerator System.

around 1 bilion proton-proton interaction per second. In Table 2.1 the main parameters for LHC are listed. The integrated luminosity $L = \int \mathcal{L} dt$ is a

Parameter		**p p**	**Heavy Ions**	
Energy per nucleon	E	7	2.76	TeV
Dipole field at 7 TeV	B	8.33	8.33	T
Design Luminosity	$\mathcal{L}$	10^{34}	10^{27}	$cm^{-}2s^{-}1$
Bunch separation		25	100	ns
Number of bunches	k_B	2808	592	
Number of particles per bunch	N_p	1.15 x 10^{11}	7.0 x 10^7	
β value at IP	β	0.55	0.5	m
RMS beam radius at IP	σ	16.7	15.9	μm
Luminosity lifetime	τ_L	15	6	hr
Number of collisions/crossing	n_c	~ 20	-	

Table 2.1: The machine parameters relevant for LHC detectors.

measurementof the number of events produced in a period of data tacking per cross section unit. Larger data acquisition time corresponds to a larger number of events acquired, and it is possible in these conditions to explore low cross section events.

The LHC startup is expected at the end of September 2009, with collisions following in late October and with the first physics data in the late 2009 with, an integrated luminosity of more than 200 pb^{-1} and at 5 TeV energy per beam for the first period of run.

2.2 The CMS detector

CMS (Compact Muon Solenoid)[34] is one of the two general purpose experiments which will take data at the LHC. Its aim is to investigate a wide range of physics: from the search for the Higgs boson to searches for new physics beyond the Standard Model, to the precision measurments of already known particles and phenomena. CMS has the same scientific purposes as ATLAS experiment, but it is designed using different technical solutions as well as a different magnet system. To achieve these goals, CMS detector has to fulfil to some requirements:

- Muons have to be reconstructed in the range $|\eta| < 2.5$ with good momentum resolution and also good mass resolution ($\sim 1\%$ at 100 GeV/c^2),

and the detector has to be able to determine unambiguosly the charge of muons up to p$\sim$ 1 TeV/c.

- The inner track system must be able to guarantee an high track reconstruction efficiency and a good momentum resolution of charged particles. Pixel detectors close to the impact region, are needed to provide an efficient triggering and offline τ and b tagging.

- Electromagnetic calorimeter has to provide a good energy resolution as well as a good photon pairs and electron pairs invariant mass resolution ($\sim$ 1% at 100 GeV/c^2) in a wide region ($|\eta| < 2.5$). It must to provide also a correct measurement of the direction of photons and the identification of primary vertex.

- Jets must be reconstructed with high E_T^{miss} resolution in a large region ($|\eta| < 5$) and with a fine lateral segmentation ($\Delta\eta \times \Delta\phi < 0.1 \times 0.1$).

The technical solutions adopted for CMS detector to supply these requirements are explained in more details in the following section. The most important components of CMS are its high field solenoid, a full silicon-based inner tracking system and a fully active scintillating crystals-based electromagnetic calorimeter. Figure 2.2. illustrates an overview of CMS detector with its subdetectors. The CMS detector consists of a longitudinal structure, the *barrel* and of two disks orthogonal to the beam pipe, the *endcaps*. In the centre of the barrel a 4T superconducting solenoid, which allows to achieve good momentum resolution [2], is positioned . A return field of about 2T with opposite direction than that provided by the solenoid, coveres the region where four muon stations are located. Each station consists of several layers of alluminium drift tubes (DT) in the barrel region and of cathode strip chambes (CSC) in the two endcaps. In both regions, DTs are complemented by resistive plate chambers (RPC). Inside the magnet, the tracker and the two calorimeters are inserted. The tracker is made of 10 layers of silicon microstrips providing the required granularity and precision, and of 3 layers of silicon pixel detectors, placed closer to the impact region in order to improve the measurement of the impact parameter of charged particles as well as the the position of the secondary vertices. CMS electromagnetic calorimeter (ECAL) is homogeneous and is charachterized by a very good

[2]The resoluion in p_T improves with increasing in magnetic field intensity according to this relation:

$$\left.\frac{\sigma_{p_T}}{p_T}\right|_{geom} = \frac{\sigma_s}{s} = \frac{8}{0.3BL^2} p_T \sigma_s \ .$$

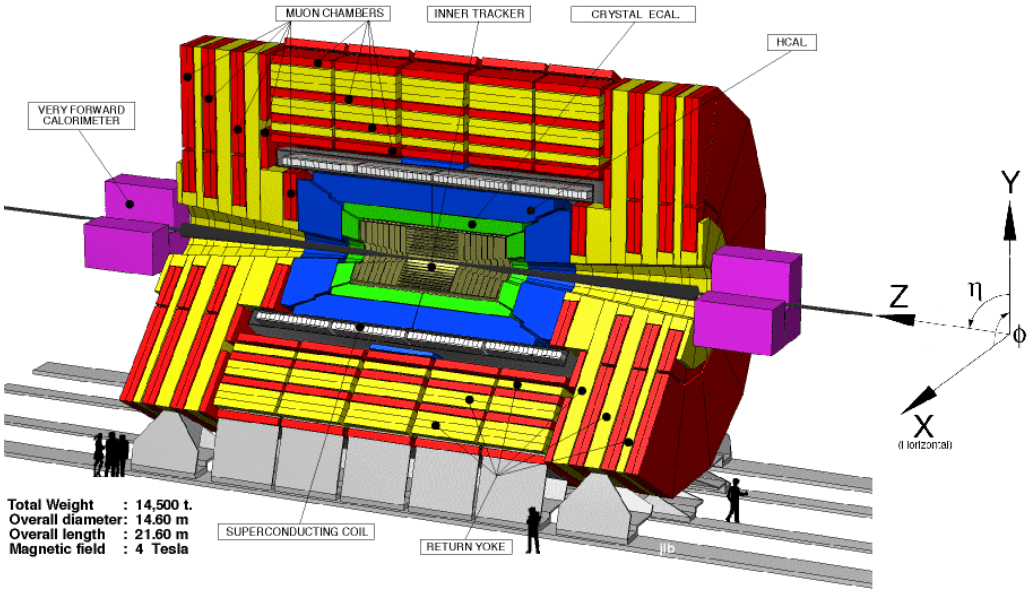

Figure 2.2: An overview of the CMS detector.

energy resolution. It is uses lead tungstate crystals ($PbWO_4$) and covers a pseudorapidity region up to $|\eta| < 3.0$. The scintillation light is collected by silicon avalanche photodiodes (APDs) in the barrel region and vacuum phototriodes in the endcaps. In front of the ECAL a preshower detector is installed in order to reject π^0 s. Between ECAL and the magnet, a sampling hadron calorimeter is installed covering the same η region as the ECAL. The scintillating light, due to the passage of particles through the crystals, is converted by wavelenth shifter fibres embedded in the scintillator, then collected and detected by hybrid photodiodes, HPDs, which provide high gain and at the same time very low sensitivity to the high magnetic field. A coverage up to $|\eta| < 5$ is provided by an iron-quartz fibre calorimeter. Figure 2.3 shows different kinds of particles traversing all subdetectors.

In terms of radiation length, the thickness of the detector is greater than 25 X_0 for ECAL and in terms of interaction length is about 7-11 λ_I for HCAL (depending on η). We will return on the details of each detector in the following sections.

The total pp cross section at $\sqrt{s} = 14$ TeV is about 100 mb, hence, at the design luminosity CMS will observe an event rate 10^9 inelastic events/s. So, the trigger and the online selection process must be able to reduce the

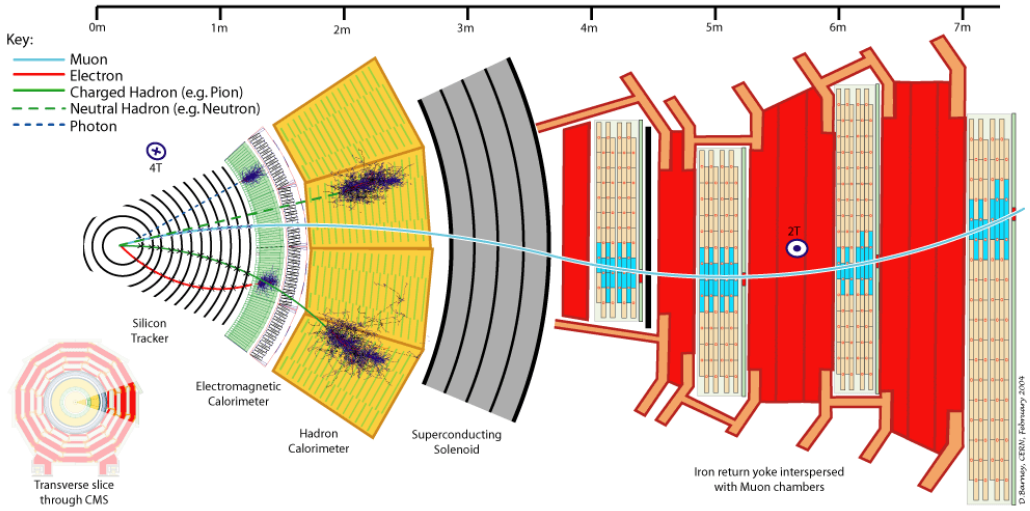

Figure 2.3: Overview of different kind of particles traversing all CMS subdetectors.

number of events, to store and analyze, to about 100 events/s. The short time between two bunch-crossing (25 ns) requires very fast readout and trigger systems.

Products of different collisions within the same bunch or even different bunches can *pile up* on the same detector, thus making information on the event uncorrect. In order to avoid the superimposition of events coming from two following bunches, the readout electronics must be very fast. The effect of pile up can be reduced also by using high granularity detectors with good time resolution. This implies a great complexity because an high number of electronic channels is needed and therefore a good synchronization among them.

Moreover the detector is subject to radiation damage due to the large flux of particles coming from the interaction region and it must be high resistant to it. Another source of radiation damage is the *beam-halo* which provides a not negligible rate of particles hiting the subdetectors.

The coordinate system

The coordinate system adopted by CMS has the origin centred at the nominal interaction point inside the experiment. The z-axis points along beam direction. The x-axis and the y-axis belong to the plane orthogonal to the

beam direction, the former points at the centre of the LHC, while the latter points vertically upward. CMS detector has a cylindrical symmetry around the z-axis, and for this reason a more convenient coordinate system is given by the radius r, i.e. the distance from z-axis, the azimuthal angle ϕ defined from the x-axis in the $x-y$ plane and the polar angle from z-axis in the $y-z$ plane. For hadron colliders the polar angle θ is more conveniently replaced by the pseudorapidity η defined as $\eta = -\ln(\tan(\theta/2))$. Figure 2.2 shows the CMS coordinate frame close to the detector.

2.2.1 The tracking system

The inner tracking system of CMS[40] is designed to provide a precise and efficient measurement of the trajectories of charged particles coming from the LHC collisions, as well as a precise reconstruction of secondary vertices. It is placed in the inner part of the apparatus, completely immerse in the 4T magnetic field generated by the solenoid. It extends for a length of 5.8 m and for a diameter of 2.5 m and it is centred around the interaction point. The high number of particles traversing the tracker for each bunch-crossing (every 25 ns) requires high granularity in order to identify and reconstruct the trajectories and a fast response to assign them to the correct bunch-crossing. Indeed the high density of the readout electronics needs an efficient cooling. The large particle flux in the impact region is also an intense source of radiation, hence the detector has to be resistent to radiation damage. The expected tracking system lifetime is $\sim$10 years. All these features areprovided by the silicon technologies. For this reason the tracker has been designed entirly as a silicon detecor. As already mentioned, at designed LHC luminosity of $10^{34}\text{cm}^{-2}\text{s}^{-1}$, about 1000 particles per bunch-crossing hit the tracker. This means that at a radius of 4 cm, the hit rate density is 1 MHz/mm^2, 60 kHz/mm^2 at a radius of 22 cm and 3 kHz/mm^2 at a radius of 115 cm. The tracking system is therefore divided into three regions:

- *Pixel* detectors are placed closest to interaction vertex where the particle flux is higher: three cylindrical barrel layers at radii of 4.4, 7.3 and 10.2 cm and two disks on each endcap. This system allows to keep the occupancy net larger than 1%. The size of each pixel is of 100 x 150 μm^2. The pixel detector counts 66 milion pixels.

- The radial region between 20 cm and 55 cm, where the particle flux is lower than the region closest to the interaction vertex, is covered by the *silicon microstrip* tracker with a minimum cell size of 10 cm x 80 μm. It is organized in three barrel layers and three disks at each endcap.

- In the outermost region, that extends from 55 cm to 116 cm a system of *larger-pitch silicon strips* is adopted since the particle flux is sufficiently low to allow their use.

Figure 2.4 shows a schematic drawing of the CMS tracker.

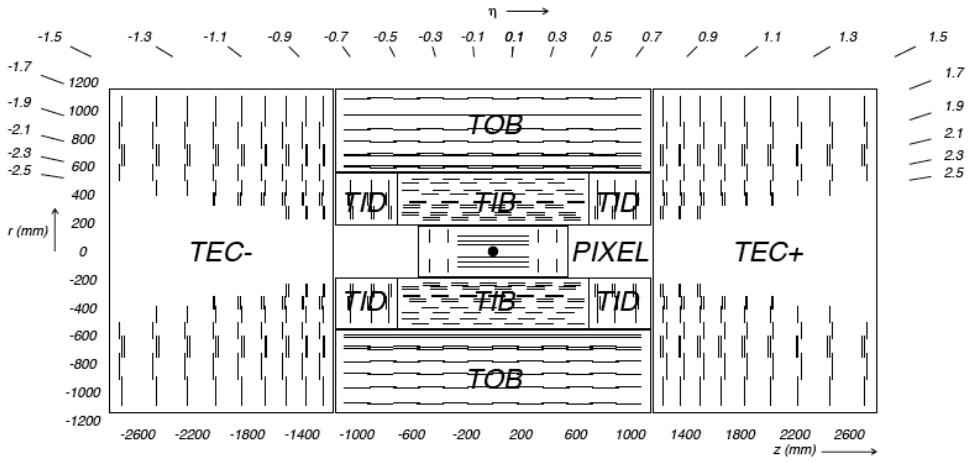

Figure 2.4: Transverse section of the CMS tracking system. It is made of a Pixel detector and a Strip detector divided into 4 subdetectors: Tracker Inner Barrel (TIB), Tracker Inner Disks (TID), Tracker Outer Barrel (TOB) and Tracker EndCaps (TEC+ and TEC-). Each line represents a detector module, while double lines indicate back-to-back modules which deliver stereo hits.

The Pixel detector

The Pixel system (Figure 2.5) provides precise measurements of trajectory points in $r-\phi$ and z with a spatial resolution about 10μm for the $r-\phi$ measurement and about 20μm for the z measurement. It is very important to reconstruct secondary vertices from b and tau decay, and also to provide a seed track for outer track reconstruction. The Pixel detector cover the pseudorapidity region $|\eta| < 2.5$.

The presence of a 4T magnetic field implies a Lorentz drift that leads to a charge spreading of the collected signal charge over more thant one pixel. The Lorentz angle is 23°. This effect improves the spatial resolution. The endcap

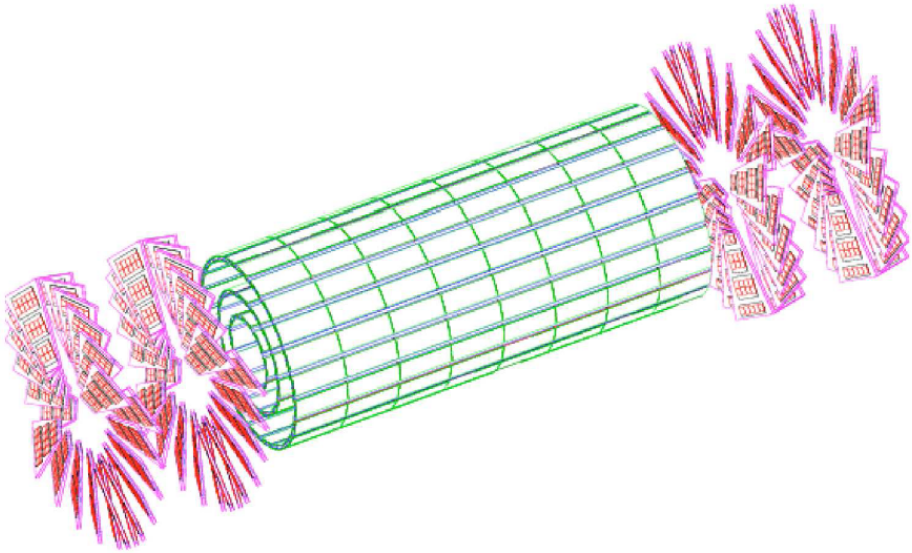

Figure 2.5: The three layers of barrel section of the Pixel detector (green) and the four disks of the endcap (red).

pixel disks in order to benefit from the Lorentz effect, has been constructed with a turbine-like geometry, with blades rotated by 20°.

The Pixel barrel detector is made of three layers at radii of 4.4, 7.3 and 10.2 cm. The pixel modules are mounted inside CMS on their support structure, divided in two half-cylinders, together with the supply tubes which house also the electronics for read-out and controls. The entire barrel length is 570 mm, ranging from -285 mm to +285 mm and consists of about 800 modules.

The forward Pixel detector is composed of two disks for each endcap, extending from 6 to 15 cm in radius and placed at $|z| = 34.5$ cm and 46.5 cm. Each disk is divided into 24 blades supporting 7 modules.

Each module is composite of two silicon basestrips, which support the module, and of the front end electronics consisting of read-out chips bump-bounded to the detector modules by red indium connections.

The Strip detector

The intermediate and outermost regions of tracking system (figura 2.6) are occupied by the silicon strip tracker divided into four subsystems. At radius 55 cm the Tracker Inner Barrel (TIB) extends with its 4 layers, coupled to the

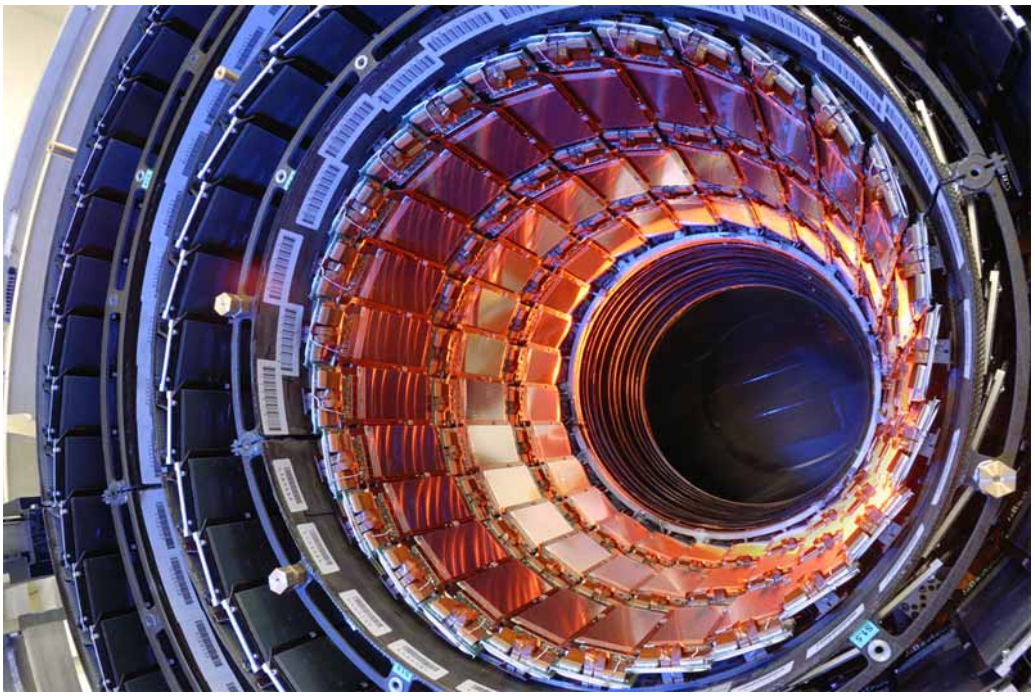

Figure 2.6: Overview of the Strip detector.

Tracker Inner Disks (TID) composite of 3 disks at each end. The barrel and endcap layers are made of 320 μm thick silicon micro-strip sensors oriented parallel to the beam direction in the barrel and radially on the disks. They provide up to 4 $r-\phi$ measurements. The strip pitch becomes larger in the outermost layers, it is 80 μm on layers 1 and 2, and 120 μm on layers 3 and 4 in the TIB, leading to a spatial resolution of 23 μm and 35 μm respectively. In the TID the strip pitch varies between 100 μm and 141 μm. The Tracker Outer Barrel surronds the TIB and the TID up to a radius of 116 cm and counts 6 layers of micro-strips larger than the ones used in the inner tracker: the strip thickness is 500 μm and their pitches are 183 μm on the first four layers (the inner ones) and 122 μm on layers 5 and 6. The TOB provides six additional $r-\phi$ measurements with a spatial resolution of 53 μm and 35 μm. The TOB coveres the region extending to $\pm$ 118 cm along the beam pipe (z-axis). The Tracker EndCaps (TEC+ and TEC-, where the sign indicates the covered z region) extends along the beam axis in the interval 124 cm $< |z| <$ 282 cm and along the radius from 22.5 cm $< |r| <$ 113.5 cm. Each TEC consists of 9 disks, carrying 7 rings of micro-strip detectors with thickness variable between 320 μm and 500 μm, and with a strip pitch which varies in the interval 97-184 μm. The layers of the TEC provide another 9 ϕ measurements for trajectory. The two inner layers of TIB, TID and TOB as well as the first, the second and also the fifth layer of TEC, are charachterized by the presence of a second strip layer mounted back-to-back with a stereo angle of 100 mrad providing a stereo view, i.e. a measurment of the second coordinate, which is z for barrel layers and r for endcap layers. This measurement allow to achieve an average single-point resolution of 230 μm in the TIB and 530 μm in the TOB, in TID and TEC (varies with strip pitch). Refer to Figure 2.7 to see the TIB layers (two double-sided and two single-sided) and the TOB ones (two double-sided and four single-sided).

The modules which host the silicon sensors are supported by a carbon-fibre structures inside an outer support tube that provides a temperature control system that keeps the operating temperature around -10°C.

This design for the strip tracker system allows to have at least 9 hits, about which 4 are two-dimentional measurements, for tracks in the range $|\eta| \leq 2.4$. The strips detector counts about 9.3 milion of strips and covers an area of about 198 m^2.

Performance of the tracker

Figure 2.8 shows the resolution of transverse momentum, transverse impact parameter and longitudinal impact parameter as a function of pseudorapidity, for single muons of transverse momenta up to 1, 10 and 100 GeV. The

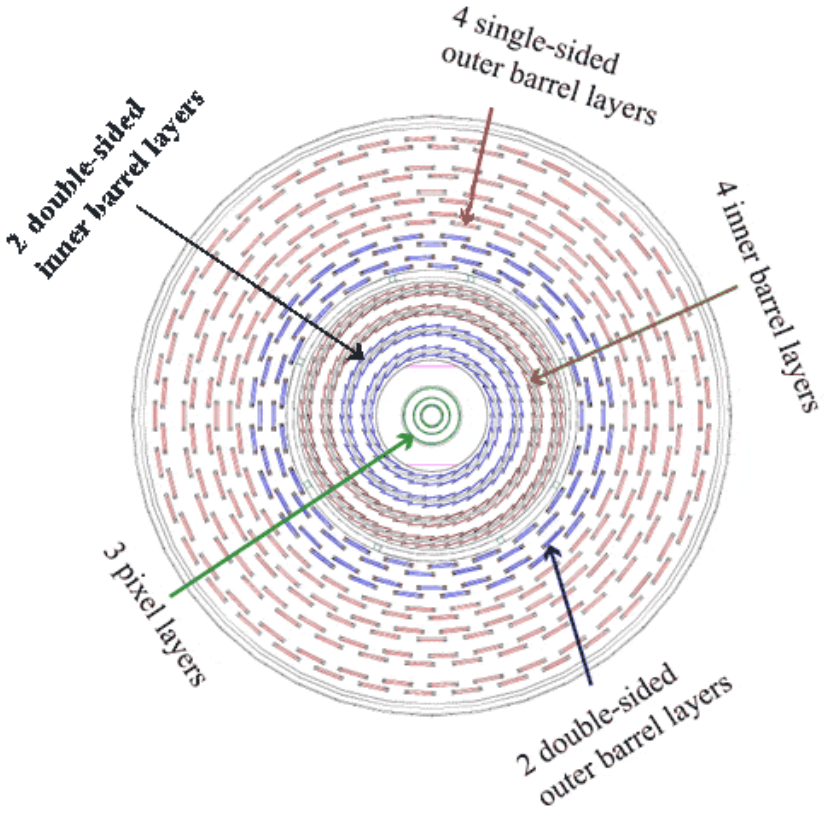

Figure 2.7: Transverse section of the tracking system. In green the three pixel detector layers. TIB and TOB layers are shown indicating in blue the double-sided layers which provide a stereo view, and in brown the single-sided layer.

transverse momentum resolution is dominated by multiple scattering for low p_T muons. In the region $|\eta|$ ≈1.6, for 100 GeV particles the resolution is about $1 \div 2\%$ The track reconstruction efficiency is plotted in Figure 2.9 for

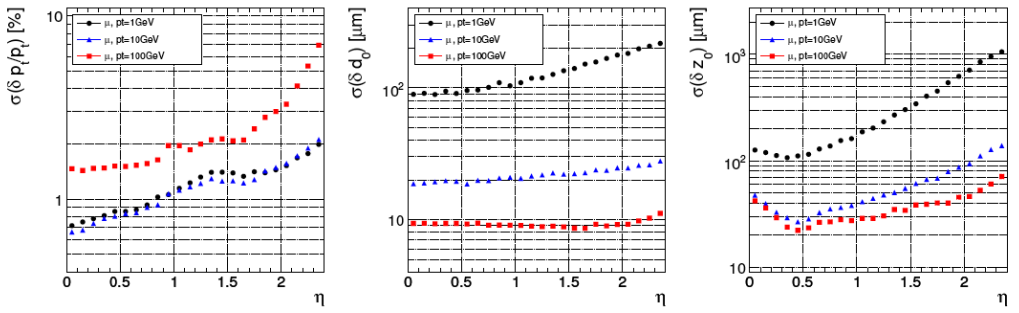

Figure 2.8: From the left: resolution of transverse momentum (left) , transverse impact parameter (centre) and longitudinal impact parameter (right) respect to the pseudorapidity, for single muon transverse momentum of 1, 10 and 100 GeV.

both muons and pions at different transverse momentum values. For muons efficiency it reaches 99%, indipendently of p_T. The decrease of the efficiency at $|\eta| \approx 0$ is due to the presence of gaps between the ladders of the pixel detectors at $z \approx 0$, while at high values of η the decrease in efficiency is caused by the reduced coverage of the pixel forward disks. Pions and hadrons in general interact with the material of the tracker and, hence, their reconstruction efficiency is lower than muons' one.

2.2.2 The Electromagnetic calorimeter

The Electromagnetic calorimeter of CMS (ECAL) is an hermetic homogeneous calorimeter made of 61200 lead tungstate ($PbWO_4$) crystals mounted in a central barrel and of 7324 crystals in each of two endcaps. This system is completed with a preshower (designed to reject π^0) inserted in front of endcaps.

The ECAL has to identify the decay in two photons of the Higgs boson. This requirement demands a very good energy resolution, provided by the homogeneous calorimeter design. The lead tungstate crystals have high density (8.28 g/cm^3), short radiation length (0.89 cm) and short Moliére radius

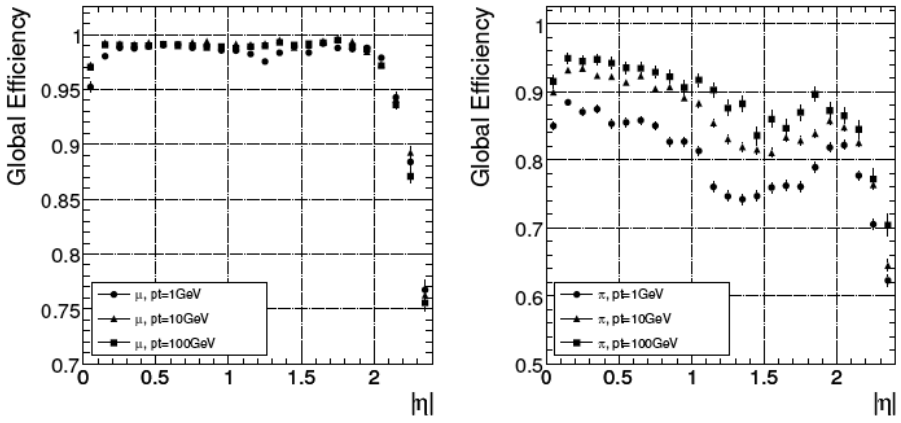

Figure 2.9: Global track reconstruction efficiency for muons (left) and pions (right) as function of η.

(2.2 cm) resulting in a fine granularity and in a compact structure. An interesting feature of these crystals is their scintillation decay time, which is of the same order of magnitude as the bunch-crossing time, about 80% of the light is emitted in 25 ns. However their light yield is very low (30 photons/MeV) and strongly dependent on the temperature. This requires the system has to be maintained to a constant temperature to high precision. It requires, hence, a cooling system to keep the temperature of crystals an photodetectors stable within ± 0.05°C in order to preserve energy resolution. The nominal operating temperature of the CMS ECAL is 18°C, and the cooling system employs water flow to stabilize the detector.

The barrel section of the ECAL (BE) covers the region at $|\eta| < 1.479$ with 61200 crystals of dimentions: 22×22 mm^2 at the front face, 26×26 mm^2 at the rare face, and a length of 230 mm, corresponding to 25.8 X_0. The total barrel crystal volume is 8.14 m^3 and its weight is 67.4 t. The crystals (at the centre of their front face) are 1.29 m distant from the z-axis. All the crystals are supported by an alveolar structure made of an aluminium layer and two layers of glass fibre-epoxy resin.

The endcap part of the ECAL (EE) covers the pseudorapidity range $1.479 < |\eta| < 3.0$ ad is distant 315.4 cm from the interaction point. The crystals have a rear face cross section 30×20 mm^2 and a front face cross section 28.62×28.62 mm^2 and a length of 220 mm, corresponding to 24.7 X_0. Crystals in

EE are grouped in 5×5 modules and arranged into carbon-fibre alveolar structure. The total EE volume is 2.90 m^3 with a weight of 24.0 t.

The light signal coming from scintillators must be converted into an electric signal by photodetectors, which need to be fast, highly radiation resistent, able to operate in the 4 T magnetic field and must compensate the low yield production of the scintillators with a high gain and high quantum efficiency. Avalanche photodiodes have been chosen to detect the light coming from the EB scintillators, while in the EE vacuum photodiodes have been installed. The latter ones have lower quantum efficiency and internal gain, but a larger detection surface.

A preshower device covers the region $1.653 < |\eta| < 2.6$. It is made of two planes of silicon strips which lie behind disks of lead absorber at depths of 2 X_0 and 3 X_0 and the aim of the preshower detector is to identify neutral pions in endcap region, but also to help with the position determination of electrons and photons.

Performance of the electromagnetic calorimeter.

The energy resolution of CMS ECAL can be parametrized as function of the energy (Figure 2.10) as:

$$\left(\frac{\sigma}{E}\right)^2 = \left(\frac{S}{\sqrt{E}}\right)^2 + \left(\frac{N}{E}\right)^2 + C^2 \tag{2.1}$$

where S is a stochastic term, N a noise term and C a constant term. Different contributions have a role in each term. The fluctuation in the number of produced and collected electrons is included in stochastic term, while the noise is due overall to electronic noise and to pile-up events. The constant term takes into account contributions such as:

- the stability of working conditions, such as temperature and high voltage;
- the presence of dead material between the crystals and the rear and lateral leakage of the electromagnetic shower;
- the non-uniformity of the longitudinal light collection, due to the truncated pyramidal shape of the crystals and to the high refractive index;
- the inter-calibrations error;
- the radiation damage of the crystals, the exposition of the crystals to high radiation dose, resulting in a change of detector response to the deposited energy.

The constant term dominates at high energy.

In test beam the energy resolution has been found to be:

$$\left(\frac{\sigma}{E}\right)^2 = \left(\frac{2.8\%}{\sqrt{E}}\right)^2 + \left(\frac{0.12}{E}\right)^2 + (0.30\%)^2 \tag{2.2}$$

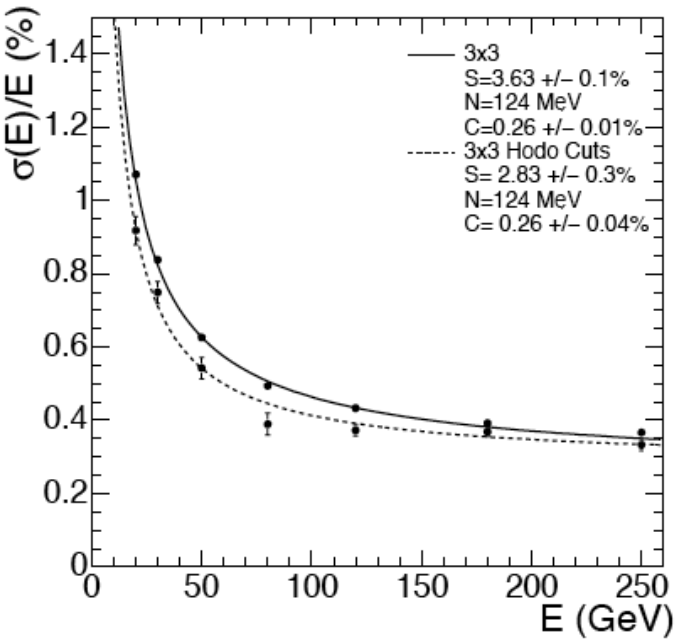

Figure 2.10: ECAL energy resolution, σ_E/E, as a function of the electron energy as measured from a beam test. The energy was measured in an array of 3×3 crystals with electrons.

2.2.3 The Hadron Calorimeter

The CMS Hadron Calorimeter (HCAL) has been designed to cover a wide range of physics processes with different signatures in final states, particularly those involving hadron jets and neutrinos, but also exotic particles resulting in missing transverse energy (E_T^{miss}). In order to have a good E_T^{miss} measurement, the HCAL has to minimize the non-Gaussian tails in the energy resolution and to provide a good conteinment and hermeticity. A strong condition for the HCAL is its location: inside the magnet coil and surrounding the ECAL (Figure 2.11). Therefore, the HCAL extends from radius 1.77

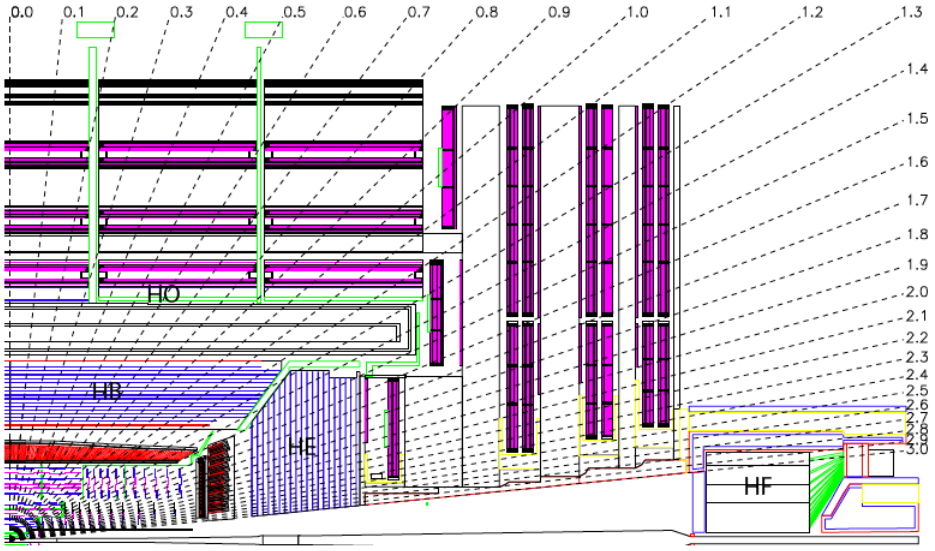

Figure 2.11: Longitudinal view if the CMS detector showing the locations of the hadron barrel (HB), endcap (HE), outer (HO) and forward (HF) calorimeters. HB ad HE are placed surronding the ECAL and inside the solenoid. HO and HF are installed outside the magnet coil.

m to the inner surface of the magnet at radius 2.95 m, and has to maximize the amount of material inside this region in terms of interaction length, in order to absorb the hadronic shower, and at the same time the absorber has to be non-magnetic. Brass has been chosen as absorber material because it is a non-magnetic material and has short interaction length (Table 2.2.3 reports brass physical properties).

Chemical composition	70% Cu, 30% Zn
Density	8.53 g/cm^3
Radiation length	1.49 cm
Interaction length	16.42 cm

Table 2.2: Physical properties of the bass absorber

An outer calorimeter is placed outside the solenoid complementing the barrel calorimeter, and acts as a *tail catcher.* A forward hadron calorimeter extends the pseudorapidity coverage up to $|\eta| = 5.2$ using Cherenkov technology.

The barrel hadron calorimeter (HB) is a sampling calorimeter placed inside the magnet coil surrounding the ECAL barrel. It covers the pseudorapidity range $|\eta| < 1.3$. The plastic scintillator is divided into 32 η sectors resulting in a segmentation of $\Delta\eta \times \Delta\phi = 0.087 \times 0.087$. The absorber consist of two steel plates, a 40 mm thick front one and a 75 mm thick back one, and of eight brass plates 50.5 mm thick and other six plates 56.5 mm thick. The total absorber thickness at 90°is 5.82 interaction lengths. Of course, the effective HB thickness increases with the polar angle according to $1/\sin\theta$.
The HB baseline active material is Kuraray SCSN81[45] plastic scintillator and has a thickness of 3.7 mm. The main reasons which have led to choose it are its long-term stability and moderate radiation hardness. The first layer, layer 0, is made of 9 mm thick Bicron BC408[46]. The light is collected in plastic scintillator tiles, readout through embedded wavelength shifting fibres and converted into an electric signal by multichannel hybrid photodiodes (HPDs).

The endcap part (HE) extends in a pseudorapidity interval $1.3 < |\eta| < 3$, a region which collects about 34% of the particles produced in the final states. It consists of 14 η towers with a segmentation in ϕ of 5° for the 5 towers at lower η, and of 10° for the 8 innermost towers. The total number of HE towers is 2304. The design of the two HE is driven by the need to avoid

"dead" zones rather than high resolution. Indeed, the jet energy resolution in the HE is limited by the pile-up, the magnetic field effects and also by the parton fragmentation. The entire design provides a self-supporting hermetic construction. As for the HB, the absorber material is the brass: plates of 79 mm thickness are spaced by 9 mm gap to accomodate the scintillators. Including the adopted electromagnetic crystals, the total amount of material of the two calorimeters is about $10\lambda_I$.

The trapezoidal scntillators adopted are 3.7 mm thick SCSN81 for the 1-17 layers, and 9 mm thick Bicron BC408 for layer 0. The scintillation light is collected also in this case by wavelength shifting fibres and readout by the multipixel hybrid photodiodes (HPDs), due to their very low sensitivity to magnetic field and also to their large dynamical range.

The outer calorimeter (HO) is placed in the pseudorapidity central region, as in Figure 2.11 in order to provide sufficient containment for hadron showers together with EB and HB, and it extends outside the magnet coil. The solenoid is used as the additional absorber with a thickness equal to $1.4/\sin\theta\ \lambda_I$ and allows to identify late starting showers and to measure the shower energy deposited after HB. The pseudorapidity region covered by the HO is $|\eta| < 1.3$. The HO consists of 10 mm scintillators. The tiles are grouped in 30°-sectors, the same ϕ segmentation used in the muon system DT chambers. Acting as "tail catcher" the HO improves the E_T^{miss} resolution of the calorimeter.

Being placed inside the muon system, outside the solenoid, the HO is constrained to be integrated into the muon system geometry. It is divided into 5 rings along η with iron as absorber material. Each ring has a length of 2.5 m along the z-axis. The HO scintillators follow the same tower geometry in η and ϕ as the rest of HCAL. Figure 2.12 shows longitudinal and transverse view of the outer calorimeter.

The forward hadron calorimeter (HF) provides a coverage of the pseudorapidity range $3.0 < \eta < 5.0$ by steel/quartz fibre. The front face is located 11.2 m away from the interaction pont, outside the solenoid.

The signal is generated when charged shower particles, above the Cherenkov threshold ($E \geq 190$ keV for electrons) generate Cherenkov light, hence the calorimeter is most sensitive to electromagnetic component. The signal originated in this way reaches the photomultipliers throught the quartz fibres. The steel absorber extends for 1.65 m depth and is composed of 5 mm thick grooved plates where fibres are inserted. The detector is funtionally subdivided into two longitudinal half parts: half of the fibres extends along the entire length of the absorber, while the other half starts at a depth of 22 cm from the front of the detector. This design allows to distinguish showers gen-

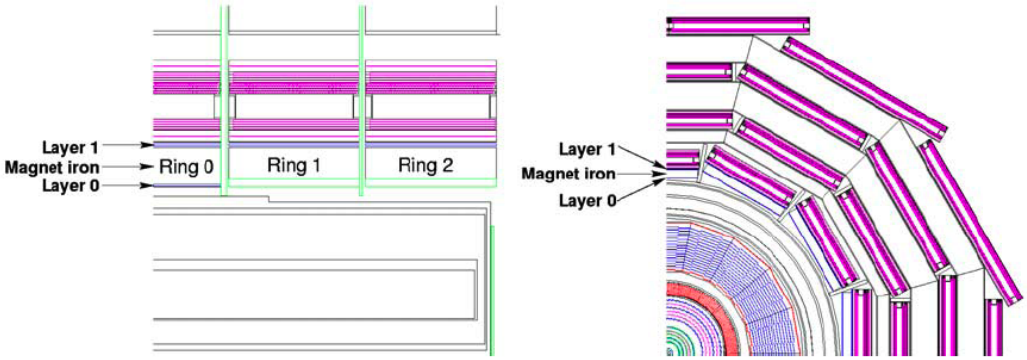

Figure 2.12: Longitudinal and transverse views of the outer calorimeter, HO, of the CMS detector, showing positions of HO layer.

erated by electrons and photons, which deposits a large part of their energy in the first 22 cm, from those generated by hadrons which produce roughly equal signals along the entire length of the calorimeter. Long and short fibres are integrated in the grooves of the absorber, and are placed alternatively. These fibres run parallel to the beam line.

The forward calorimeter is cylindrical and inserted around the beam pipe. It is distant 12.5 cm from the beam line and its outer radius is 130.0 cm. Its structure is organized in 13 η towers, all with a size given by $\Delta\eta \approx 0.175$, with the exeption of highest-η tower with $\Delta\eta \approx 0.3$ and the lowest one with $\Delta\eta \approx 0.1$. The detector is azimuthally subdivided into 20° modular wedges. In total, the structure counts 900 towers and 1800 channels in the two HF modules.

Performance of the hadron calorimeter

In order to evaluate the performance of the three parts of HCAL (HB, HE and HF) it is usual to look at the jet energy resolution and at the missing transverse energy resolution. The granularity of these three parts has been chosen to make the jet energy resolution quite uniform , as a function of E_T. Figure 2.13 shows the transverse energy resolution as function of E_T. The missing transverse energy resolution is given by $\sigma_{E_T^{miss}} \approx 1.25\sqrt{\sum E_T}$, where $\sum E_T$ is the jet transverse energy, without considering clustering corrections.

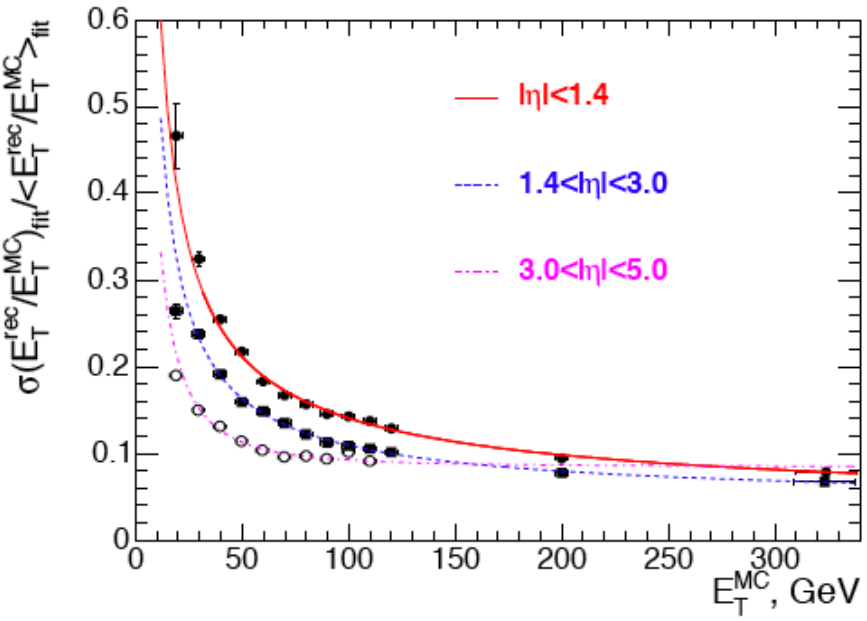

Figure 2.13: The jet transverse energy resolution as a function of the simulated jet transverse energy for barrel, endcap and forward region.

2.2.4 The magnet

The CMS magnet is a large superconducting solenoid designed to reach a 4 T field. An high bending power is required to reach a good p_T resolution and to distinguish unambiguously the sign for muons with momentum up $\approx$ 1 TeV. The bending power of the high field also allows to measure aslo high transverse momenta with good resolution. The magnet parameters are given in Table 2.2.4.

The magnetic coils surrounds the two calorimeters (ECAL and HCAL) and the tracking system. The goal is to achieve a muon resolution about 10% p_T for 1 TeV muons. The p_T resolution scales with 1/B, where B is the strength of the magnetic field.

Field	4 T
Inner Bore	5.9 m
Length	12.9 m
Number of turns	2168
Current	19.5 kA
Stored energy	2.7 Gj
Hoop stress	64 atm

Table 2.3: CMS superconducting solenoid parameters

2.2.5 The muon system

Muon final states are clear signatures of the interesting physics processed expected at LHC, such as the Higgs decay into ZZ and ZZ*, which in turn decay into four leptons, and in particular the muon channel is called the "gold plated" channel. Furthermore the best four-particle mass resolution can be achieved if the 4 leptons are muons, because they are less affected by radiative losses than electrons. This is only one of the physics processes and of interest in LHC physics program involving muons. A system for muon detection with a wide angular coverage for the detection is necessary. The muon system provides a precise muon momentum measurement, but also a time measurement of the bunch-crossing, and also works as trigger for events involving muons.

Momentum measurement, in the muon system, is determined by the muon bending angle at the exit of the 4T coil, considering the interaction point as the origin of the muon. For low-momentum muons, the best resolution is given by the silicon tracker. In fact up to p_T values of 200 GeV/c the resolution of the muon system is dominated by multiple scattering rather than by the chamber spatial resolution.

The CMS muon system is designed using three kinds of gaseous particle detectors for muon identification: drift tubes chambers (DT), chatode strip chambers (CSC) and resistive plate chambers (RPC). As the tracker and the calorimeters, it is made of a cylindrical barrel and two endcaps. The first two provide an exellent spatial resolution, while the RPCs have a very good timing. Figure 2.14 shows the longitudinal view of the subdetector.

The barrel extends up to $|\eta| < 1.2$ and is based on DT chambers. The drift cells (Figure 2.15) consist of a stainless steel anode wire placed between two parallel alluminium layers. Two chatodes shape the electric field. The gas mixture choosen to fill the cell is: 85% Ar and 15% CO_2. This leads to a

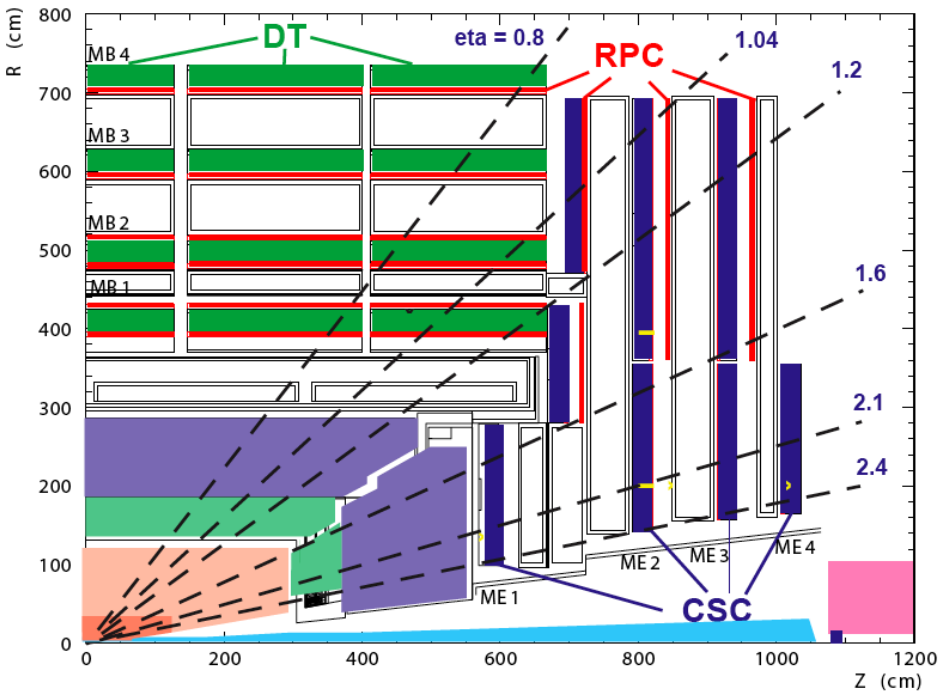

Figure 2.14: Longitudinal section of the quarter of the CMS muon system, with DT chambers in the barrel, CSCs in the endcap and RPCs coupled to both DT chambers and CSC.

maximum time of electron drift of 380 ns for a maximum path of 21 mm. The efficiency of single chamber lies around 99.8% with a spatial resolution of $\approx 180\ \mu m$. The device is organized into 4 stations (MB1, MB2, MB3 and MB4) interspersed with layers of the flux return plates as shown in Figure 2.16. The first 3 stations, named MB1, MB2 and MB3 contain 8 chambers for the measurement of the muon coordinate in the $r-\phi$ plane, and 4 chambers which provide a z-measurement. The last station MB4 does not contain a z-measuring plane. Along the longitudinal direction the muon system barrel is divided into 5 wheels, as well as the HO, which are subdivided into 12 sectors each covering a 30° azimuthal angle. The design chosen for the barrel provides a single point resolution of $\approx 200\mu m$ and a ϕ precision better than $\approx 100\mu m$ in position and ≈ 1 mrad in direction.

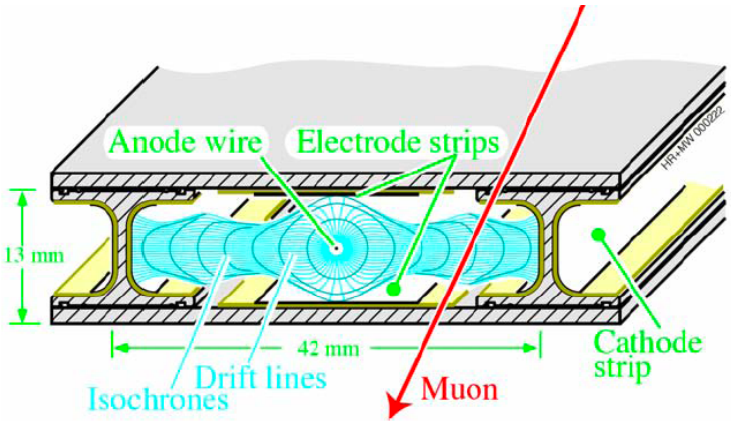

Figure 2.15: Schematic view of a drift cell. The electrons, coming from the gas ionization due to the passage of a muon, drift towards the wire anode. The voltages applied to the electrodes are +3600V for wires, +1800V for strips, and −1200V for cathodes.

DT chambers in stations MB1 and MB2 are installed between two RPCs and in the stations MB2, MB3 they are coupled to one RPC. High p_T muons traversing the muon system cross up to 6 RPCs and 4 DT chambers providing in the DT system up to 44 measured point from which the muon track candidate can be built.

The two endcap regions of CMS are characterized by a non-uniform magnetic field and large background levels. The muon system is constructed, in these regions, with CSCs, which are multi-wire proportional chambers, with

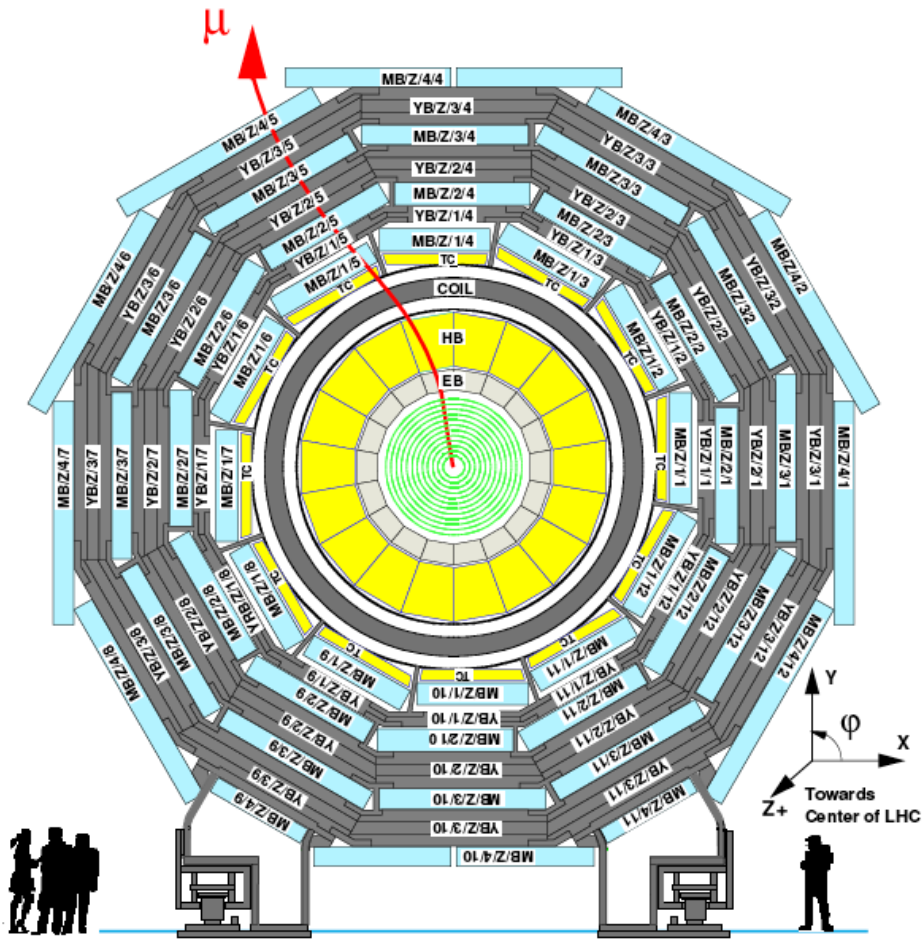

Figure 2.16: Layout of the CMS barrel muon DT chambers in one of the 5 wheels. Each wheel is divided into 12 sectors, each covering a 30° azimuthal angle, and composed of 4 stations.

fast response time, fine segmentation and radiation resistance. The covered pseudorapidity range is $0.9 < |\eta| < 2.4$. Each endacap is divided into 4 stations of CSCs of trapezoidal shape and is installed perpendicularly to the beam line. Each CSC (Figure 2.17) consists of 6 gas gaps filled with a mixture of 30% Ar, 50% CO_2 and 20% CF_4. Each gap has a plane of radial chatode strips, providing an $r - \phi$ measurement, and a plane of anode wires placed orthogonally to the catode plane and read out in order to give an η measurement, as well as a beam-crossing time of a muon: a charged particle traversing the CSCs causes gas ionization and, hence, an electron avalanche with the consequent production of a charge introduction on the anode wire and an image charge on the chatode strips. The very fast signal on the anode wires is used in the Level-1 Trigger. While, determining the centre of gravity of the charge distribution on the cathode strips makes it possible to achieve a better spatial resolution, that is tipically $\approx 200\mu m$, and an angular resolution in ϕ of 10 mrad. In order to improve the time resolution and the p_T resolution and can be used to resolve ambiguites due to multiple hits in a chamber, RPCs are installed also in the endcap. An RPC is coupled to each of the first three stations.

RPCs provide spatial informations with a time resolution comparable to scintillators: the tagging time of an ionizing event is shorter than 25 ns, the time interval between two LHC bunch-crossings. It allows to know what bunch-crossing the event belongs to. For this reason a dedicated muon trigger is based on RPCs.
The RPCs consist of 2 gaps formed by four bakelite electrodes, which are covered by graphite in order to distribute uniformly the high voltage over the surface. The 2 mm gaps are filled with a gas mixture of freon ($C_2H_2F_4$, 95%) and isobutane (i-C_4H_1O). Since the RPCs work in avalanche mode the gas gain is low, and the signal has to be amplified by the readout electronics. Figure 2.18 shows a schematic view of an RPC.

2.2.6 The trigger

At LHC design luminosity, for a bunch-crossing rate of 40 MHz, a very high rate of interactions is expected ($\approx 10^9$ interactions/s). Each event has a size about 1MB. It is impossible to store and process such a large amount of data. A selection has to be made on the events in order to reduce the selected event rate to about 100 Hz, according to what is allowed by the limits on the storage capacity. This goal is achieved by the trigger system (Figure 2.19) in two steps: the Level-1 (L1) Trigger and the High-Level Trigger (HLT).
Data readout from the front-end electronics must reach the service cavern

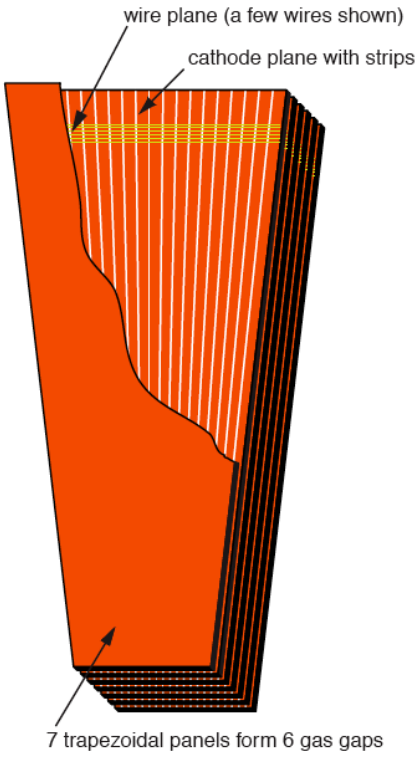

Figure 2.17: View of the CSC made of 7 parallel trapezoidal panels forming 6 gaps.

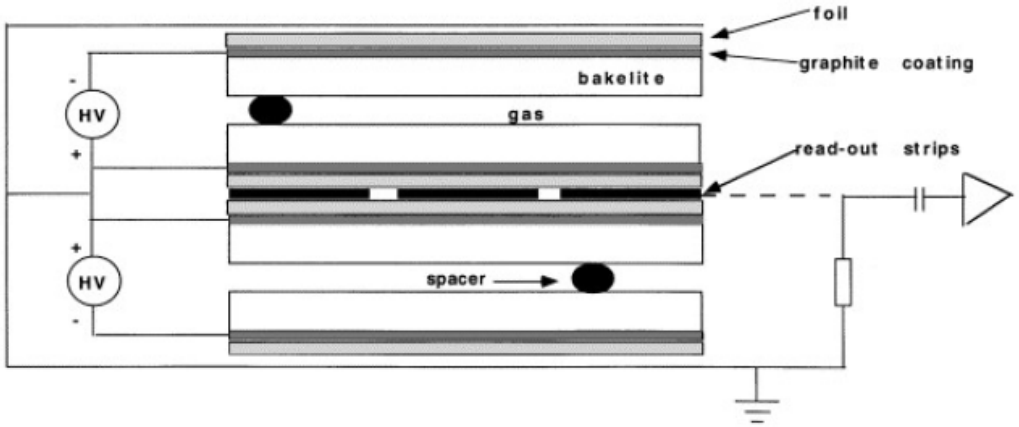

Figure 2.18: Layout of the RPC double-gap structure.

that houses the L1 Trigger system and return back to the front-end electronics and provides a decision about taking or discarding the data from a particular bunch-crossing. It takes about 3.2 μs to perform a decision.

The L1 Trigger must reduce the events rate to 100 KHz, manteining at the same time an high efficiency on interesting events. The time in which the Trigger has to take a decision is too short to consider information from all raw data; then, it works involving only the calorimeters (Calorimeter Trigger) and the muon system (Muon Trigger), as well as correlelations among informations of both two systems (Global Trigger). Figure 2.20 illustrate the L1 Trigger organization. The presence of "trigger objects" such as electrons, photons, muons and jets, above a set of E_T and p_T thresholds, is the base for L1 Trigger decisions. The triggered objects pass to the subsequent Data Aquisition system (DAQ) and HLT for further reconstruction and selection steps.

The next level of trigger is the HLT, which aim at further reduce the events rate to about 100 Hz, using more detailed informations than the L1 trigger, and more sophisticated reconstruction alghoritms. The data coming from the readout buffers are transferred to processors, each running the HLT software code to produce a smaller output rate for mass storage. The idea on which the HLT is based, is to reconstruct only objects in the region of interest and discard other objects. Many virtual trigger levels are used. A "local reconstruction" is made initially using the full information of the muon system and the calorimeters. In a second step also the information of the tracker

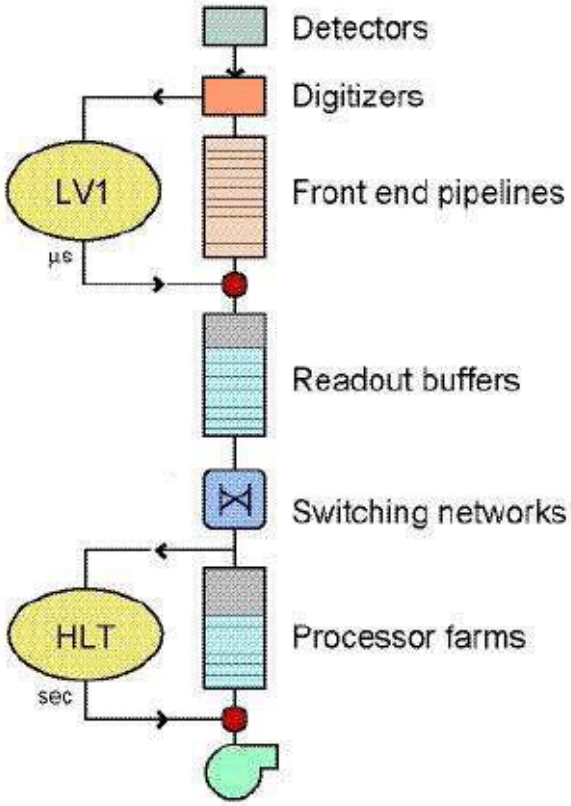

Figure 2.19: Data Flow in the Trigger/DAQ system.

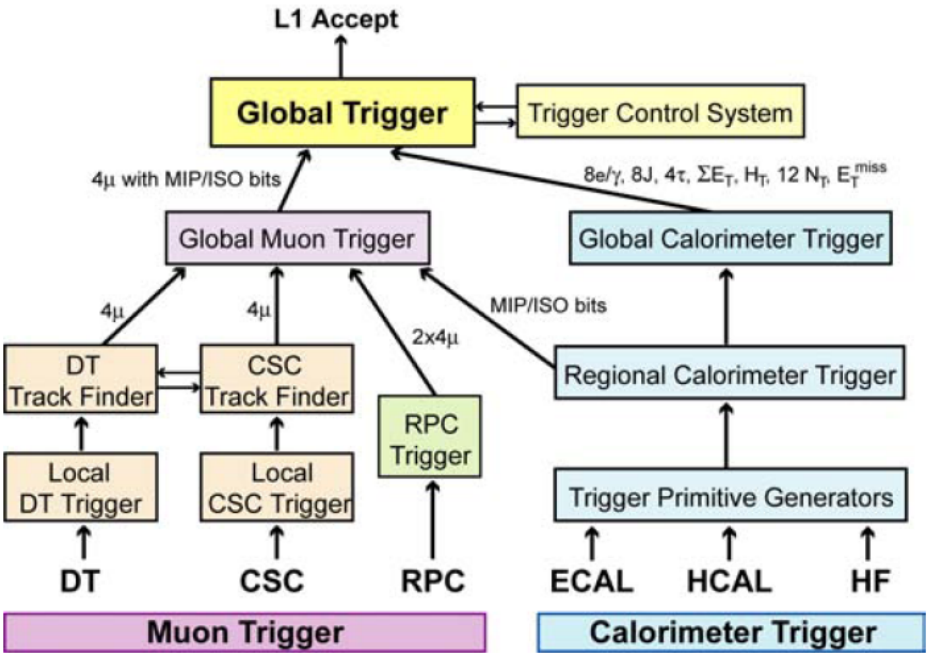

Figure 2.20: Architecture of the Level1-Trigger.

hits is taken into account and added. The last step is the use of the full event informations (calorimeters, muon system and tracker).

Chapter 3

The physics program at CMS experiment

The choice of LHC design parameters is determined by the physics goals which have brought to the construction of this machine. According to this idea the LHC collider is a pp collider, and differently from e^-e^+ colliders, it is a discovery machine. The partons are the fundamental constituents entering the pp scattering, and they carry an unknown fraction of the proton four-momentum each, x_1 and x_2 . Therefore, the centre of mass energy (CM) of the hard scattering process, given by $\sqrt{\hat{s}} = \sqrt{sx_1x_2}$, can span a range of different orders of magnitude. The centre of mass energy of the proton-proton collisions will be $\sqrt{s} = 14$ TeV, and if x_1 and x_2 are of the order of $0.15 - 0.20\%$ (it depends on the origin of the quarks, if they are "valence" or "sea" type) of the incoming proton momentum, the partonic CM energy, $\sqrt{\hat{s}}$, will be about $1 - 2$ TeV, that is the energy range we want to explore.

The total proton-proton cross section at 14 TeV is ≈ 110 mb, where the contribution from inelastic processes cross section is about 60 mb, and 40 mb is the contribution to the cross section from elastic scattering. Figure 3.1 shows the proton-proton cross section in a pp collider of $\sqrt{s}$ centre of mass energy.

The main goals of the CMS experiment are:

- study the symmetry breaking mechanism giving rise to particle masses, and, hence, search for the Higgs boson in the mass range 100 GeV/c^2 < $m_{\mathrm{H}} < 1$ TeV/c^2. If it wil be found we have to understand if it is compatible with the SM Higgs, and if it is not found we have to look for alternative models;

- search for new physics beyond the Standard Model such as supersymmetry, technicolor, new strong interactions, extra-dimentions, etc.

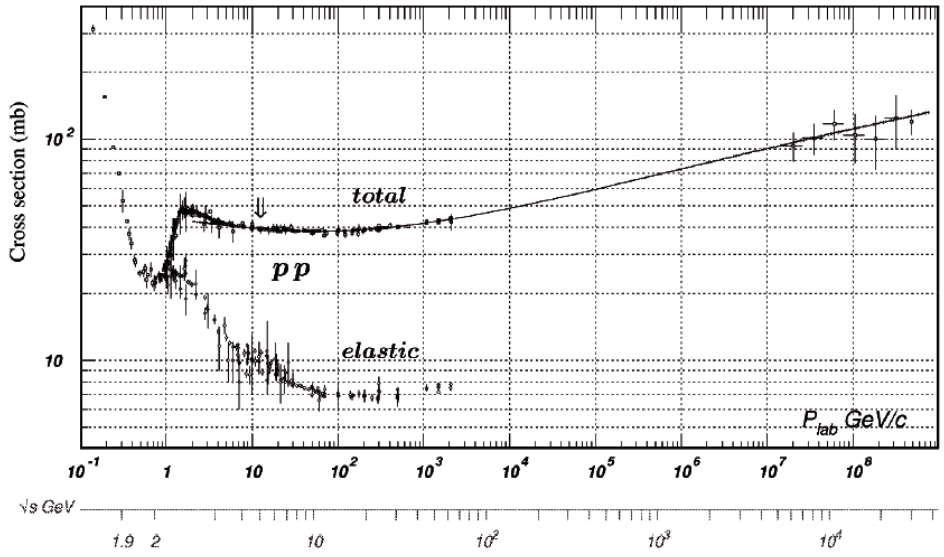

Figure 3.1: Total pp cross section in a pp collider as function of laboratory beam momentum and total centre of mass energy as reported in Particle Data Group[51]. LHC will work at a CM energy of 14 TeV.

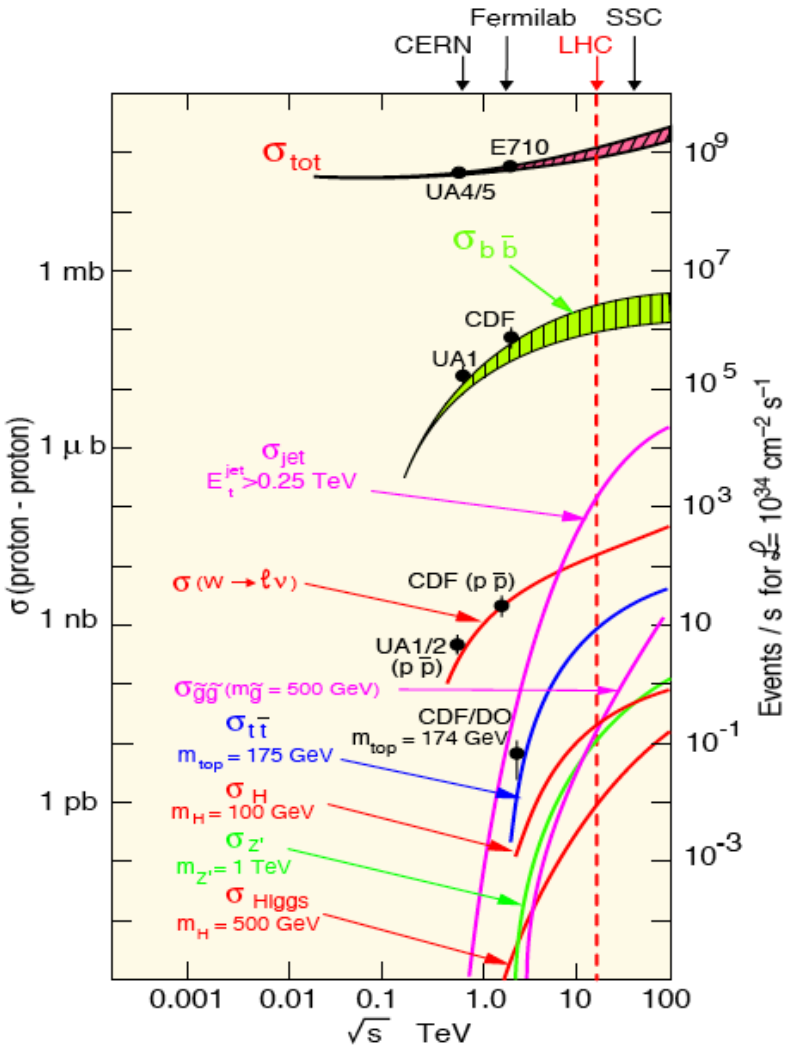

Figure 3.2: Cross sections for different processes in a proton-proton and proton-antiproton collisions as a function of the centre of mass energy with a luminosity $\mathcal{L} = 10^{34} cm^{-2} s^{-1}$

- perform precision measurements in the electroweak sector, QCD, CP violation and B physics sector.

3.1 Standard Model measurements

The Standard Model predictions have been well confirmed first by the discovery of neutral currents in 1973[1] and then by the W and Z bosons discovery in 1983[2], as reported in Chapter 1. In the following years, experiments at LEP and SLC measured, with very high precision, the properties of the W and Z. The observation of the *top*-quark at Tevatron[19] completed these measurements. There is a piece of the Standard Model still missing: the Higgs boson. At CMS searches for the Higgs boson will be performed in the Higgs mass range from 100 GeV/c^2 to 1 TeV/c^2 (see section 3.2). Already from the initial phase of data-taking, interesting measurements can be done studying the production and leptonic decays of Z and W bosons as explained in section 3.1.1. These measurements will be very useful in the understanding of alignements and detector calibrations, as well as in searches for new physics. Furthermore, as already said in the section 1.3.2, m_{H} can be extracted from a global fit of the electroweak measurements, knowing the logarithmic dependence of the electroweak corrections on m_{H}. Of course, EWs observables have to be known with high precision and one of the main goals of the CMS experiment is to perform precision measurements in the electroweak sector (m_{W}, m_{t}, triple gauge couplings, $\sin^2\theta_W$). In order to have an useful help in the determination of m_{H}, m_{W} and m_{t} should be measured with a precision $\Delta m_{\mathrm{Z}} \leq 15\ MeV$ and $\Delta m_{\mathrm{t}} \leq 2\ GeV$. Of course, since LHC is not an $\mathrm{e^-e^+}$ machine, will be a great challenge to achieve so high precision on these measurements. CMS SM measurements will be performed also in B-physics sector as in QCD.

3.1.1 Electroweak physics at CMS

The production cross sections of Z and W bosons at 14 TeV in hadronic collisions are large, their leptonic decays have very clear signatures and they are theoretically well understood. The cross sections for leptonic channels, $\mathrm{pp} \rightarrow \mathrm{Z} + X \rightarrow \ell\overline{\ell}$ and $\mathrm{pp} \rightarrow \mathrm{W} + X \rightarrow \ell\overline{\nu}$, at LHC and in the fiducial region of the CMS detector, are expected to be above 1 nb and 10 nb, respectively. Decays in electrons and muons will be detected in the very early phase of the experiment. In fact, due to their very high production rate, Z and W physics will start already with the first few inverse picobarns of collision data collected by the CMS experiment. Decays into tau leptons require higher

luminosity, because triggering is based on more sophisticated criteria, hence, these channel will be studied later.

Vector boson productions are useful for many purposes such as a precise luminosity measuremente and monitoring, high-statistics detector calibration and control of the performance of the CMS experiment. Furthermore, ZW, WW and ZZ events will provide informations on important backgrounds to searches.

The main selection, made on Z and W decays into muons, is realized by requiring muons in defined geometrical acceptance region and whitin the trigger acceptance. Useful selection criteria, together with triggering, are isolation criteria: a region around the lepton (a cone, called *isolation cone*) is defined and it is required a low total p_T in the tracker or total E_T in calorimeters within the isolation cone. Muons coming from b and c decays, or from K and π decays are produced in jets, therefore they are characterized by the presence of nearby particles, i.e. of tracks and amount of energy around them. Muons from Z and W decays are isolated. The isolation selection is very useful in background rejection, although it is a source of inefficiency. In this thesis work a careful study on isolation has been conducted (we will explain it in the following chapter).

Using these channels it will possible to study the trigger efficiency already at the startup and during the wide lifetime of the LHC experiments.

In hadron colliders such as the LHC, the electron and muon Z decay channels are experimentally the easiest to identify, since the Z decay into quark pairs have much more backgrounds than other Z decays, and W decays have not a so clear signature due to the high E_T^{miss} caused by the presence of neutrinos in the final decay states.

The production of lepton pairs in hadron-hadron virtual collisions, the Drell-Yan process[52], is described by an s-channel exchange of a photon or a Z boson: $q\overline{q} \rightarrow \gamma/\mathrm{Z} \rightarrow \ell\overline{\ell}$. At low energies the γ exchange dominates, but around the Z peak the dominating exchange is that of Z boson. At higher energies both photon and Z exchange contribute resulting in a large value of the *forward-backward asymmetry*[1], A_{FB}, due to the interference between the neutral currents.

The measurement of parton cross section and forward-backward asymmetry will provide a lot of interesting informations, such as ones about the PDFs.

[1]The forward-backward asymmetry A_{FB} is defined as:

$$A_{FB} \equiv \frac{N_F - N_B}{N_F + N_B} \tag{3.1}$$

where N_F is the number scattered into the forwards hemisphere $0 \leq \cos\theta \geq 1$ and N_B that into the backward hemisphere $-1 \leq \cos\theta \geq 0$.

The production of lepton pairs above the Z pole is a rich search field for new phenomena, because the differential cross section of the process and the interference term are sensitive to the manifestation of new physics.

The cross section and the forward-backward asymmetry depend on observables which are experimentally well measured: the invariant mass and the *rapidity*[2] of the final state lepton pair. The knowledge of these dependences together with the measurement of the cross section and the A_{FB}, will allow to reconstruct the centre of mass energy of the initial partons, although their flavours are unknown. For each pair of interacting partons there are four possible combinations of *up* and *down* quarks: $u\bar{u}$,$\bar{u}u$,$d\bar{d}$ and $\bar{d}d$. In pp collisions the anti-quarks are sea quark, while quarks may be both valence and sea quarks.

The measurements relative to di-lepton invariant mass, especially those with high-mass, will be useful from the initial phase of data-tacking to test the tracking alignment of the muon system and to calibrate the electromagnetic calorimeter with the electron channel, in order to reduce the width of possible peaks, and as already said, they will be useful as search fields for new physics (as the presence of the heavy neutral boson Z′ from its decay in muon pairs).

This thesis work will deal with $pp \rightarrow Z + X \rightarrow \mu^-\mu^+$ channel and with the measurement of its cross section.

3.2 SM Higgs boson search

The Higgs Boson mass is not predicted by the theory because it depends on two parameters, v[3] and λ. While the former is known by the relation which bounds it to the constant G_F of Fermi's theory, the latter can determine only by the direct measurement of the Higgs mass, as seen in chapter 1. On the other hand, the Higgs boson couplings to the fermions and bosons are predicted to be proportional to the corresponding fermion masses or squared boson masses. For this reason the Higgs boson production and decay processes are dominated by those channels involving heavy bosons such as $W^{\pm}$ and Z and the third generation of fermions. While the coupling to gluons and photons takes place at higher orders than tree level.

We will see in the following sections the Higgs boson production processes

[2]The rapidity is defined as:

$$y = \frac{1}{2}\log\frac{E + p_L}{E - p_L}\ , \tag{3.2}$$

where p_L is the longitudinal momentum along the direction of the incident particle and E is the energy, both defined for a given particle.

[3]

and the decay modes and what is, in each Higgs mass range, the golden channel to discover it.

3.2.1 Higgs boson production

The main channels contributing to the SM Higgs boson production at a hadron collider, such as LHC, are:

- gluon-gluon fusion
- VV fusion
- W and Z associated production, *Higgsstrahlung*
- $t\bar{t}$ associated production

The cross sections corresponding to these channels are reported in Figure 3.4 for a centre of mass energy $\sqrt{s} = 14$ TeV, the design value at the LHC.

The *gg fusion* is the dominating Higgs production mechanism, at the LHC, over the entire Higgs mass spectrum. The diagram is shown in Figure 3.4a. The main contribution is given by the top loop because of the strong coupling of Higgs boson to the top quark. The value of the cross section increases of a factor ~ 2 considering nex-to-leading orders (NLO) with respect to that leading order (LO) cross section. The $gg \rightarrow H$ cross section is affected by large uncertainty due to the gluon structure function. This Higgs production process is very interesting not only because of its relativly larger cross section in the entire mass range, but also because it is very sensitive to an hypotetical fourth generation of quark, since, as already said, the Higgs coupling is proportional to the fermion mass. The second contribution to the Higgs boson productions is the *VV fusion*. Its cross section is one order of magnitude lower than the gg fusion in a wide range of m_H values. *VV* fusion and gg fusion become comparable for high Higgs boson mass values. This process (Figure 3.4b) has a very clear signature: two spectator jets with high invariant mass are present in the forward region. This feature provides a good signal to background ratio. The uncerainties on this process are small and both LO and NLO are well known. The last two channels contributing in this scenario to the Higgs boson production are the *Higgsstralhung* and the associated production with a $t\bar{t}$ pair. Figures 3.4c and 3.4d show both of them. In the first channel, the Higgs boson is produced in association with a $W^{\pm}$ or Z boson. The cross section of this process is several orders of magnitude lower than the previous two. The last process has a $t\bar{t}$ pair as a tag of the Higgs boson production. Also for this channel the cross section is

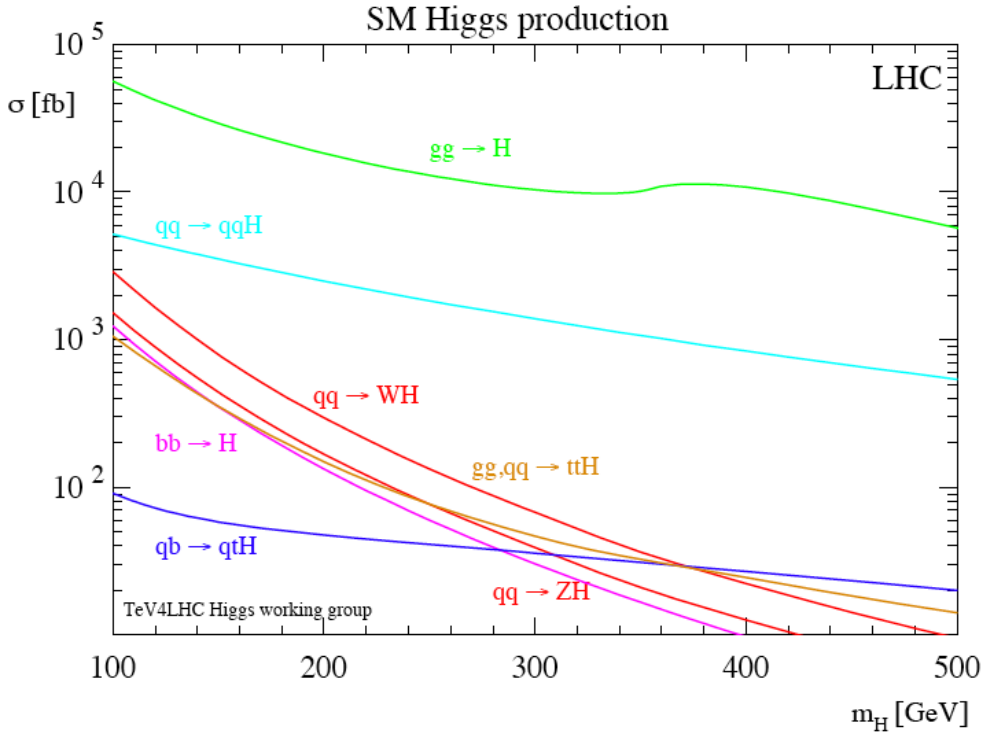

Figure 3.3: Higgs boson production cross section at $\sqrt{s} = 14$ TeV as a function of the Higgs boson mass.

quite low, but on the other hand its signature is very good and provides a clear tag of the Higgs production.

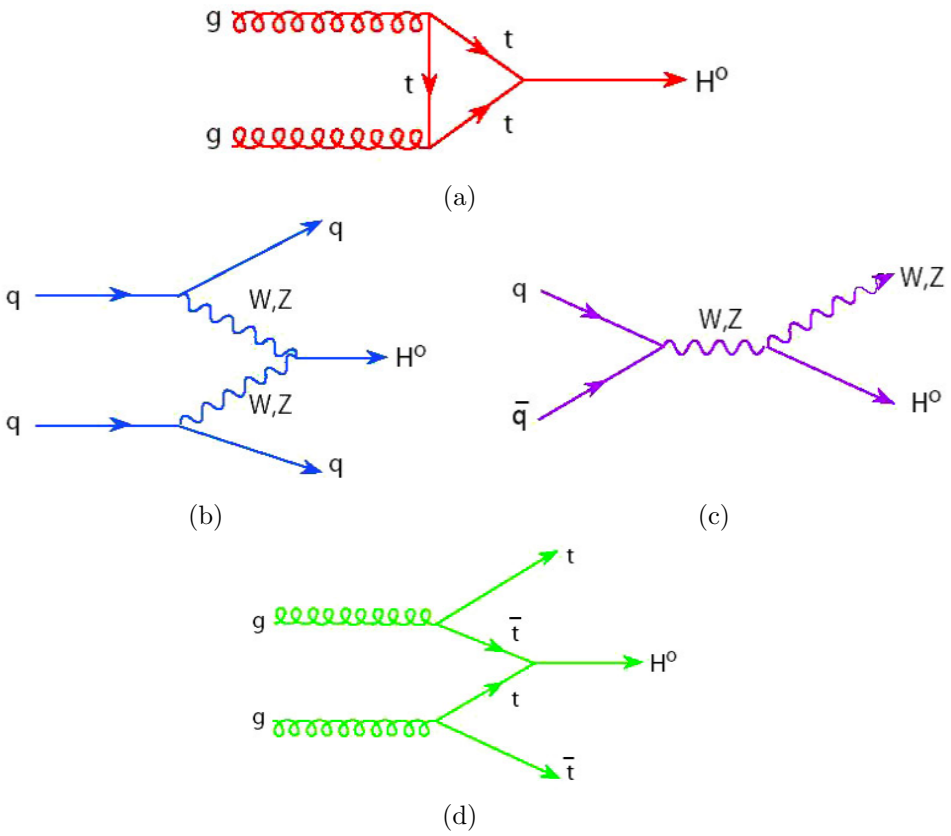

Figure 3.4: Higgs boson production mechanism at tree level in proton-proton collisions: (a) gluon-gluon fusion; (b) VV fusion; (c) W and Z associated production (*Higgsstralhung*); (d) $t\bar{t}$ associated production.

3.2.2 Higgs boson decay and search

According to the mass range, the branching ratios (BRs) of all kind of decays varies in a significant way. Hence, the discovery of the Higgs boson strongly depends on what is the mass range in which it lies and on the BRs of the decay channels in this range. Moreover, experimentally, the capability to detect the signal and reject the background is very important. The decay channels involving leptons are preferable.

Figure 3.5 illustrates the branching ratio for all possible decay modes.

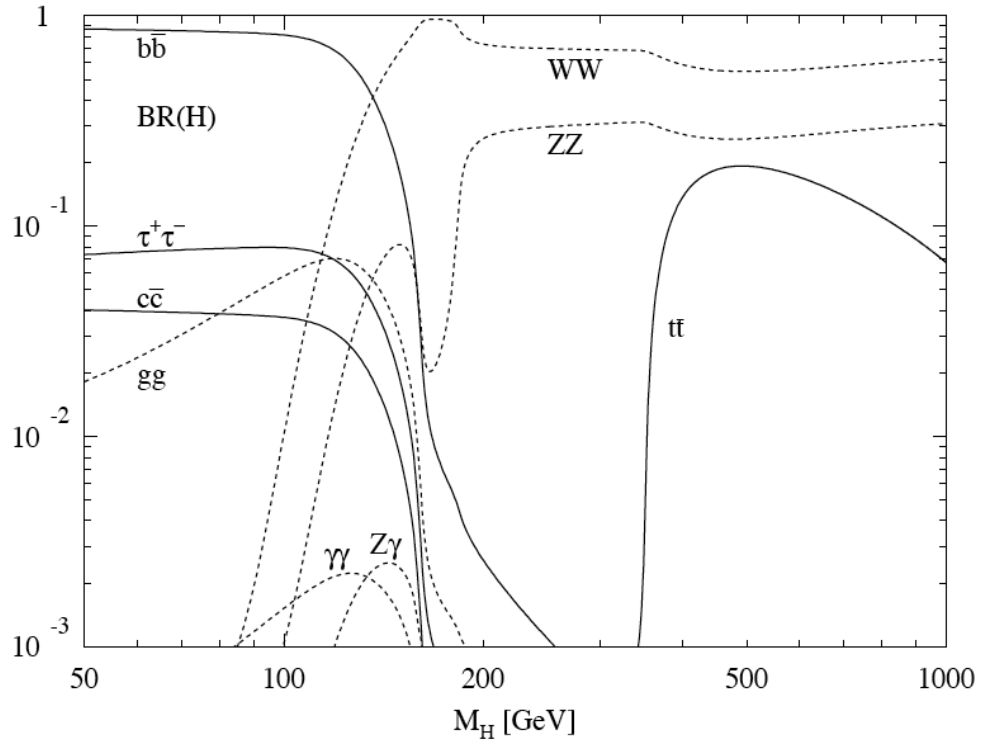

Figure 3.5: Branching ratios of different Higgs boson decay channels as a function of the Higgs boson mass. They are calculated with the program HDECAY[53] which includes the dominant higher order corrections to the decay width.

Low mass region

We can see that for low values of m_{H} fermionic decay modes dominate (up to ~ 150 GeV/c^2). Due to its large mass value, the channel which has the highest BR in this region is $\mathrm{H} \to \mathrm{b\bar{b}}$. The background for this channel makes quite difficult the search for the Higgs boson: background is constituted by di-jets and it is few orders of magnitude greater than the signal.

In spite of its low cross section, this channel, relative to a Higgs boson produced in association with a $\mathrm{t\bar{t}}$ or via Higgsstralhung, can give interesting results because of its clearer signature. Three possible final states are considerated: a leptonic channel, $\mathrm{H} \to \mathrm{b\bar{b}}$, $\mathrm{t} \to \ell\nu\mathrm{b}$, $\bar{\mathrm{t}} \to \ell\nu\mathrm{\bar{b}}$, a semi-leptonic channel, $\mathrm{H} \to \mathrm{b\bar{b}}$, $\mathrm{t} \to q\bar{q}\mathrm{b}$, $\bar{\mathrm{t}} \to \ell\nu\mathrm{\bar{b}}$ and an hadronic channel, $\mathrm{H} \to \mathrm{b\bar{b}}$, $\mathrm{t} \to q\bar{q}\mathrm{b}$, $\bar{\mathrm{t}} \to q\bar{q}\mathrm{\bar{b}}$. The signal, in these channels, is characterized by the presence of high p_T leptons and missing energy, as well as the presence of 4 b-tagged jets, two of which are coming from Higgs boson. The background is mainly due to QCD events. Most recent studies also consider Higgs production via Vector Boson Fusion. Infact, in this case, the final state is characterized by two forward/backward jets, two b-jets (from the Higgs decays) and a central high p_T photon.

The golden channel in this mass region will be the decay of Higgs boson into a pair of photons, $\mathrm{H} \to \gamma\gamma$, infact, the two high energy photons provide a very clear signature, although its cross section is quite low. We expect a narrow peak in the two photons invariant mass distribution (Figure 3.6). Background sources for this channel are photons coming from $q\bar{q} \to \gamma\gamma$, $\mathrm{Z} \to \mathrm{e^-e^+}$ and from jets. This channel has a strong dependence on the detector performance. The resolution of the electromagnetic calorimeters is crucial.

Intermediate mass region

In the intermediate mass region (130 GeV/$c^2 \leq m_{\mathrm{H}} \leq 2m_{\mathrm{Z}}$) the decays of Higgs boson into $\mathrm{WW}^{(*)}$ and into ZZ^* open up. There is a peak of the $\mathrm{H} \to \mathrm{W^+W^-}$ cross section, when the production of a pair of W on shell bosons is kinematically allowed. The best channels for the discovery in this region are: $\mathrm{H} \to \mathrm{WW}^{(*)} \to 2\ell 2\nu$ and $\mathrm{H} \to \mathrm{ZZ}^* \to 4\ell$. The first decay mode has a higher cross section, and it is very important in this range of mass where an Higgs boson can decay into two real W bosons, but into only one real Z boson and one virtual. Nevertheless, due to the presence of neutrinos, the recostruction of the Higgs boson in this case is quite difficult.

The signal events signature of the channel $\mathrm{H} \to \mathrm{WW}^{(*)} \to 2\ell 2\nu$ is two isolated high p_T leptons (that may be either electrons or muons) with a small

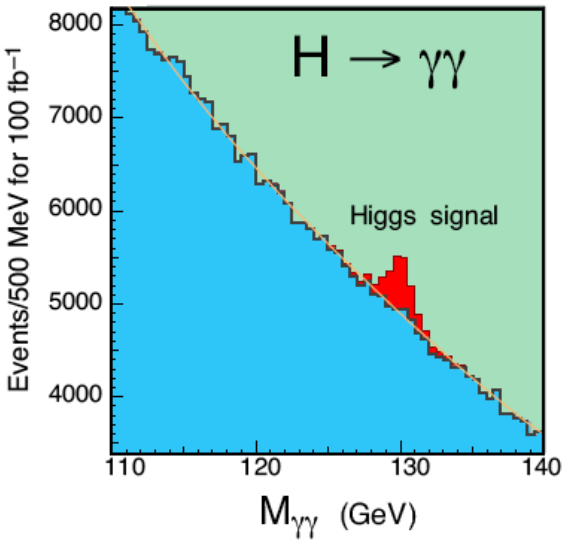

Figure 3.6: Di-photon invariant mass spectrum in H $\rightarrow \gamma\gamma$ channel.

opening angle in the transverse plane, significant E_T^{miss} and without jets in the central region of the CMS detector[54]. The topologies of the signal are three: e^+e^-, $\mu^-\mu^+$ and $e^{\pm}\mu^{\mp}$. For this channel the dominant backgrounds are the continuum W^+W^- and $t\bar{t}$ productions. The missing energy is, of course, due to the neutrinos and it prevents the presence of a signal peak as in Figure 3.7.

The decay mode H $\rightarrow ZZ^* \rightarrow 4\ell$, with $\ell = e^{\pm}, \mu^{\pm}$, has a more clear experimental signature and high signal to background ratio, but it has a very low BR. Differently from the decay into two W bosons, this decay channel allows a precise reconstruction of the Higgs boson thanks to the presence of isolated charged leptons with high transverse momentum. This channel seems to be a golden channel in this range of mass. The main sources of backgrounds are $t\bar{t}, Zb\bar{b}$ and ZZ^*/γ^*, while $Zc\bar{c}$ is neglegible. Figure 3.8 shows the invariant mass distribution for events of different Higgs mass hypothesis for the three signal topologies[55].

High mass region

In the third region, with mass values above 2 m_Z, the decay of the Higgs into two real Z is possible, and the leptonic channel is certainly the golden

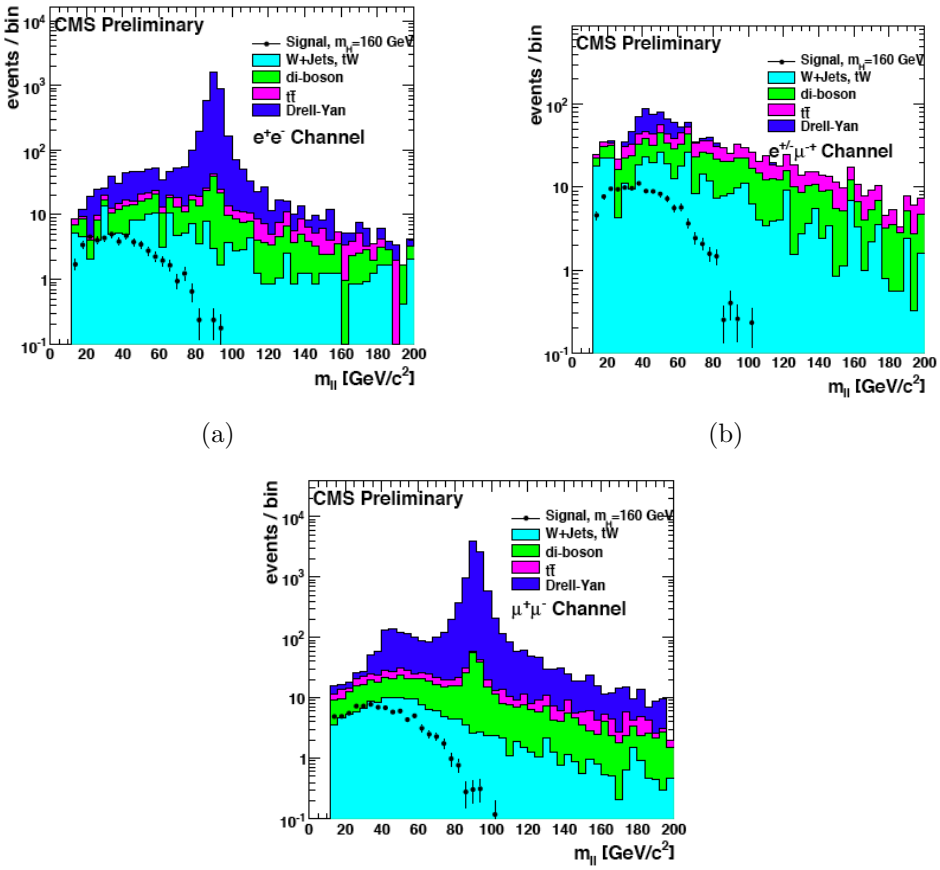

(a) (b)

(c)

Figure 3.7: Invariant mass of the di-lepton system, after the High Level Trigger, lepton identification, pre-selection cuts and the central jet veto for a SM Higgs with $m_{\mathrm{H}} = 160$ GeV/c^2[54], for (a) the $\mathrm{e}^-\mathrm{e}^+$ channel, (b) the $\mathrm{e}^{\mp}\mu^{\pm}$ channel and (c) the $\mu^-\mu^+$ channel.

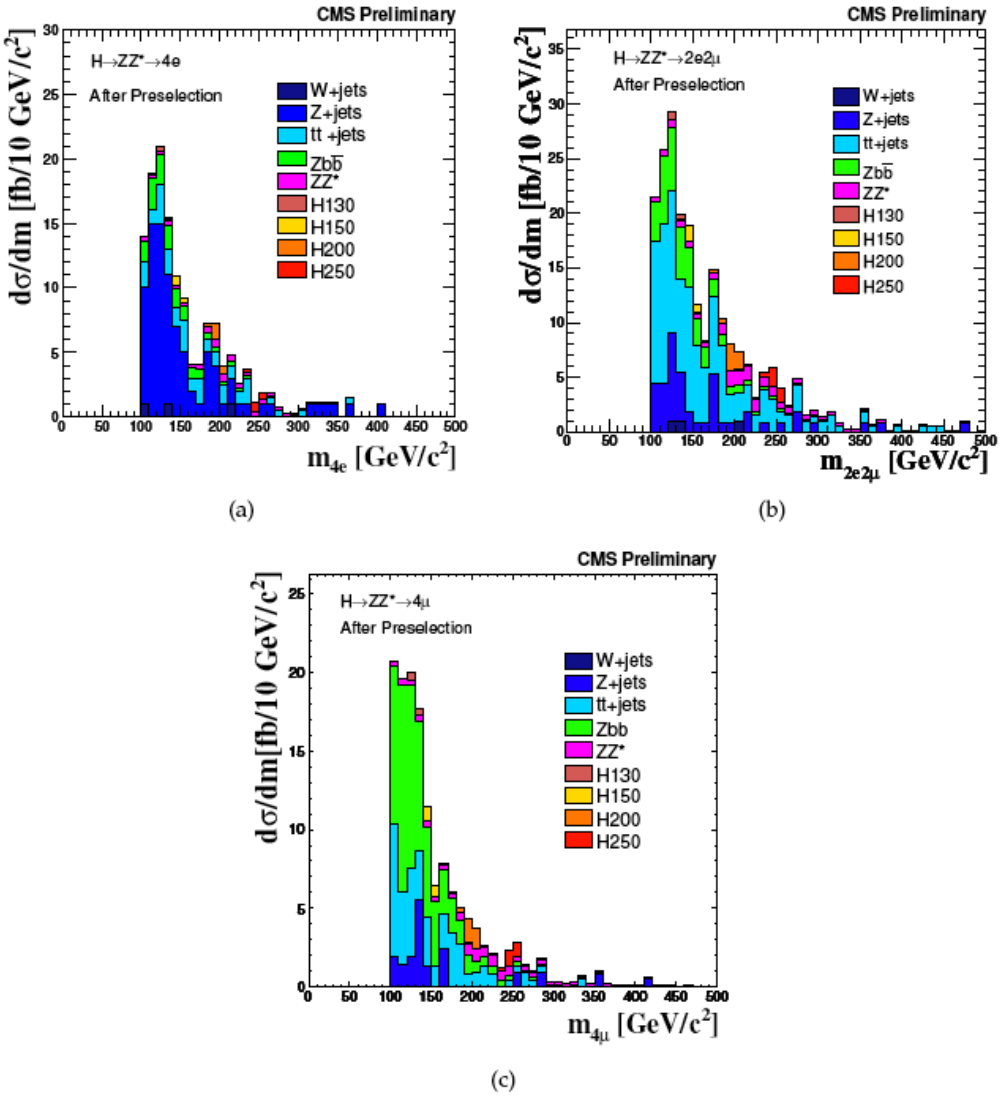

Figure 3.8: Four-lepton invariant mass after pre-selection[55] with cumulative backgrounds and H $\rightarrow$ ZZ* $\rightarrow$ 4ℓ signal events together for different m_{H} hypothesis in the (a) 4e$^-$, (b) 2e$^-$ 2μ^- and (c) 4μ^- channel.

channel, although the BR of this channel is still lower than that of the decay into two W. At mass values of about ~ 350 GeV/c^2, also $t\bar{t}$ can be produced.

Of course, a reduced production rate implies a large width of the signal, and, hence, a difficulty to observe the mass peak. For this reason decays into jets and neutrinos have also to be considered. The rate of the channel $H \rightarrow WW \rightarrow \ell\nu jj$ is higher than the four lepton channel from $H \rightarrow ZZ$ decays.

The total width of the Higgs boson resonance is a function of m_H. Below the $2m_W$ threshold the width is dominated by experimental resolution and helds of the order of the MeV, but over that threshold it becomes larger (Figure 3.9).

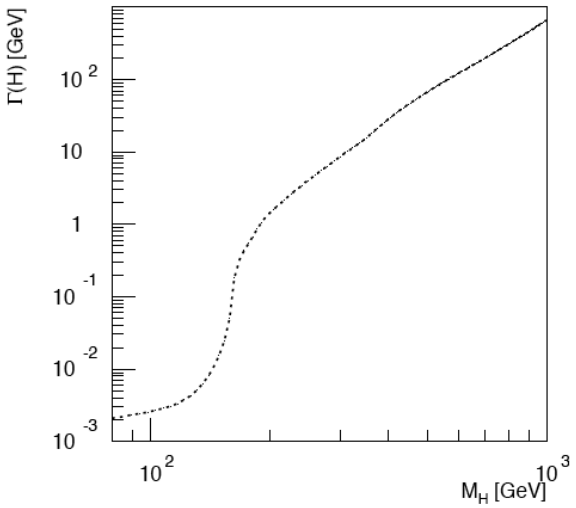

Figure 3.9: Higgs boson total decay width as a function of the Higgs boson mass.

At high values of Higgs boson mass, separating the Higgs peak from the VV continuum becomes very difficult since the width $\Gamma(H \rightarrow VV)$ is proportional to m_H:

$$\Gamma(H \rightarrow VV) = \frac{3}{32\pi}\frac{m_H^3}{v^2} \ . \tag{3.3}$$

As m_H increases, it becomes experimentally very problematic to observe the Higgs separating the signal peak from the background.

3.3 B-Physics

The CMS experiment is well suited for B physics, thanks the large b production cross section. The decay $B_s^0 \rightarrow J/\psi\phi \rightarrow \mu^-\mu^+K\overline{K}^0$ is the CMS benchmark channel to study many properties of the B_s^0 system and in particular the difference between the widths and the masses of the two weak eigenstates B_s^{0H} and B_s^{0L}. In fact this difference, such as that between the decay rates of K_S^0 and K_L^0 mesons, should be due to a different behaviour of weak interaction between matter and anti-matter particles or to the existence of an undiscovered force in nature not symmetric in matter-antimatter, and not predicted by the SM. An asymmetry in the two rates (B^0 and $\overline{B}^0$) would be a signal of CP violation since it dependes on the phases of CKM matrix.

3.4 Beyond the Standard Model

The SM has been experimentally tested with high precision, but it cannot answer to some fundamental questions like:

- the origin of Dark Matter;
- the origin of particle masses (if the SM Higgs boson will not discovered);
- the origin of the three generations of fundamental fermions;
- how to introduce Gravity in a quantum scenario;
- how to unify fundamental forces.

The LHC will probe the TeV energy scale where new physics is expected. An important part of the CMS program will be to search for this new physics beyond the Standard Model. The CMS design has been chosen to make it suitable to investigate new scenarios of High Energy Particle Physics. The production of a new gauge boson, the Z', with a mass in the TeV range is one of the possible early discover at the LHC and in particular at the CMS detector. It has a clean final state for its decays into two high p_T leptons leading to a very clear signal in CMS. In CMS, in order to detect this boson by its decay channel $Z' \rightarrow \mu^-\mu^+$, dedicated reconstruction techniques have been developed to study muons with p_T in the TeV/c range.

The strong presence of jets in LHC collisions has brought the CMS collaboration to study in detail the analysis of dijets events and the dijet invariant mass. Moreover an accurate work has been made in order to evaluate in

details experimental and theoretical systematics on the dijet mass distribution. The results of these study have been interpreted as a sensitivity to new physics scenarios.

The determination of the missing transverse momentum in collisions at an hadron collider is in general a difficult measurement since it is very suscetible to detector inefficiencies, but also to physics and instrumental backgrounds. But it may be an important signature for new phiysics events such as those concerning low mass SUSY. For this reason, techniques to calibrate E_T^{miss} with well knows Standard Model processes have been also developed in CMS. The good knowledge of the detector and a good control of backgrounds will make possible the study of low mass SUSY already with 0.1 fb^{-1} of data.

A signal of the presence of new physics could also be an excess of τ production. The selection and analysis of τ will be used to search for the A/H heavy Higgs bosons which are predicted, for example, by the Minimal Supersymmetric Standard Model (MSSM). It is, hence, very important the study conducted in detail on the τ-tagging and τ-trigger.

3.4.1 Supersymmetry

A strong motivation to search for evidences of Supersimmetry (SUSY)[56] concernes the fact that the Higgs Boson mass is affected by quantum corrections from every particle that couple to the Higgs field. Figure 3.10a shows this correction at one-loop level. This Feynman diagram yields a correction:

$$\Delta M_{\mathrm{H}}^2 = -\frac{|\lambda_f|^2}{8\pi^2}\Lambda_{UV}^2 + \dots \,. \tag{3.4}$$

Here Λ_{UV} is an ultraviolet momentum cutoff used to regulate the loop integral. It should be interpreted as at least the energy scale at which new physics enters to alter the high-energy behaviour of the theory; λ_f is the Yukawa coupling of the Higgs field to the fermion fields. Since all particles acquire their mass via the Higgs mechanism, they are all influenced by this correction to the Higgs boson mass.

Considering the graph in Figure 3.10b, a different correction is involved with a different sign:

$$\Delta M_{\mathrm{H}}^2 = -\frac{|\lambda_s|^2}{16\pi^2}\Lambda_{UV}^2 - 2m_s^2 \ln(\Lambda_{UV}/m_s) + \dots \,. \tag{3.5}$$

Thanks to this term, the corrections partially cancel out (λ_s is the Yukawa coupling of the boson s and m_s its mass). In the SM the number of fermions and bosons is very different and the large corrections remain. If there was

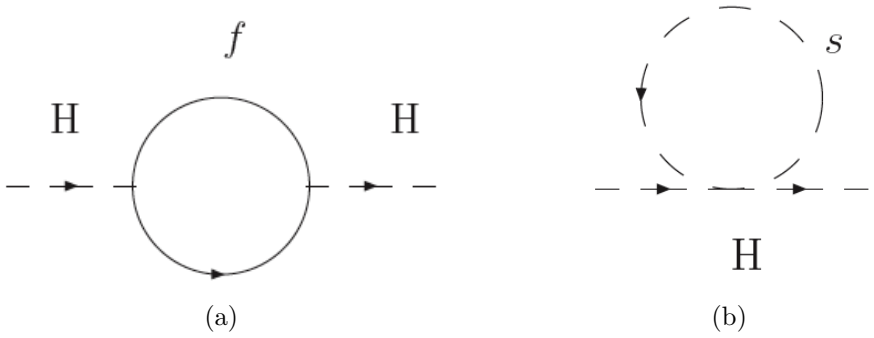

Figure 3.10: Fermion (a) and boson (b) corrections to the Higgs propagator at one loop level.

a bosonic particle for each SM fermion and vice versa, and the coupling $\lambda_s = |\lambda_f|^2$ were equal, then, all corrections would cancel out as well in case of a broken symmetry, where the masses of the corresponding particles are different. The cancellation of all such contributions to scalar masses is possible a symmetry relating fermions and bosons is assumed. This symmetry is called *supersymmetry*.

A supersymmetric transformation Q turns a bosonic state into a fermionic state ($Q \mid \text{boson}\rangle = \mid \text{fermion}\rangle$) and vice versa. According to this transformation, each SM particle is turned into its superpartner, which differs in spin by 1/2, i.e. a boson with spin 0 or 1 is associated at each fermion with spin 1/2, and a fermion with spin 1/2 is associated at each boson with spin 0 or 1. Supersymmetric particles are commonly called *sparticles*, the superpartners of the fermions get a prefix $s-$ (*squark* and *sleptons* are the sparticles associated to quarks and leptons), while the superpartners of the bosons get a suffix $-ino$ (the photon is accompaigned by the photino, and the $\widetilde{\mathrm{W}}$, W*ino*, and the $\widetilde{\mathrm{Z}}$, Z*ino* are coupled at the vector bosons W and Z, they are called *gauginos*). None of these superpartners has been observed until now. The particles included in the MSSM are listed in Figure 3.11.

The MSSM provides the existence of two Higgs doublets, H_u and H_d with $Y = \pm 1/2$, which the respective weak isospin components $\mathrm{H}^+_{u,d}$ and $\mathrm{H}^0_{u,d}$. The supersymmetric doublets $\widetilde{\mathrm{H}}_u$ and $\widetilde{\mathrm{H}}_d$ are associated to the Higgs doublets considered by the theory. The standard Higgs is a combination of H^0_u and H^0_d. The mixing of charged and neutral *gauginos* and *higgsinos* are physical states called *charginos* and *neutralinos*, respectively. Neutralinos, $\widetilde{\chi}^0{}_i$ ($i = 1, 2, 3, 4$), and charginos, $\widetilde{\chi}^{\pm}{}_1$ and $\widetilde{\chi}^{\pm}{}_2$ are ordered by their mass, indicated

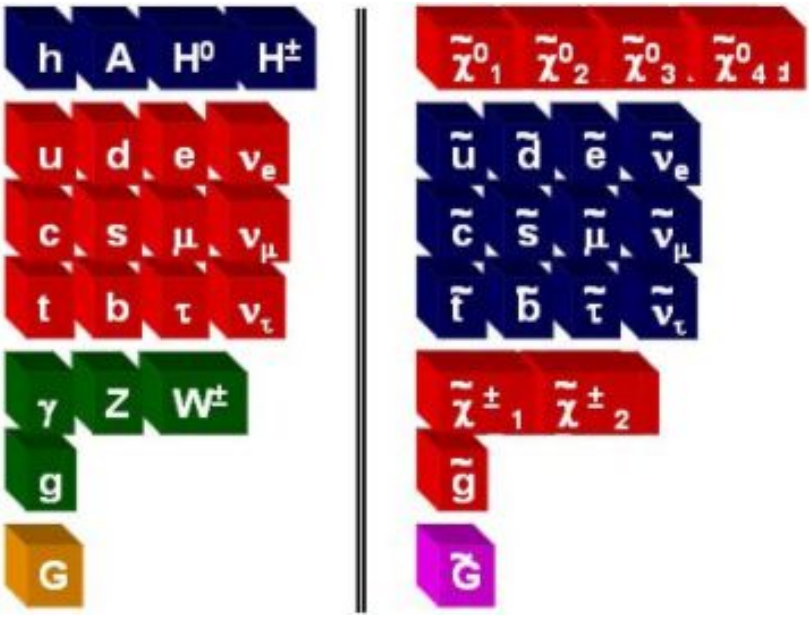

Figure 3.11: Supersymmetric partners of Standard Model particles.

by the index of the particle, where the mass increases with the index.

In supersymmetric models a new multiplicative quantum number is introduced, which allows to distinguish SM and supersymmetric particles. It is called R-parity (or matter parity) and is defined as follow:

$$P_R = (-1)^{3(B-L)+2s} \ , \tag{3.6}$$

where B is the baryon number, and L the leptonic number, while s is the spin of the particle. P_R is $+1$ for SM particles ad -1 for supersymmetric particles.

If the R-parity is conserved in decays of supersymmetric particles, the resulting decay cascade (Figure 3.12) contains the lightest SUSY particle (LSP), i.e. the lightest neutralino, which is expected to interact very weakly with matter, leading to a significant E_T^{miss} in the final state and to an abundance of leptons and jets (this decays presents a spectacular kinematical spectra in $\ell\overline{\ell}$ invariant mass distribution, as in Figure 3.13 (the plot is relative to the process in Figure 3.12)).

A very interesting feature of SUSY, and also an important motivation to search for it, is the unification of gauge couplings at high energy. This feature is not allowed by the SM theory, but it could be achieved with a Minimal Supersymmetric Standard Model (MSSM) (Figure 3.14).

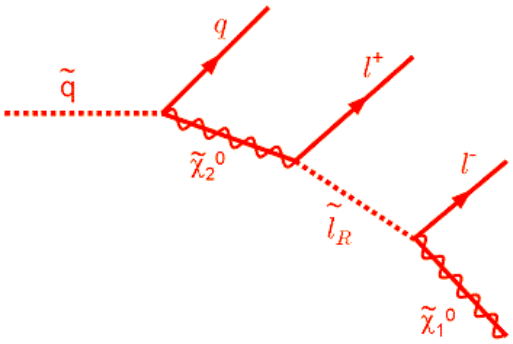

Figure 3.12: The decay cascade of an squark.

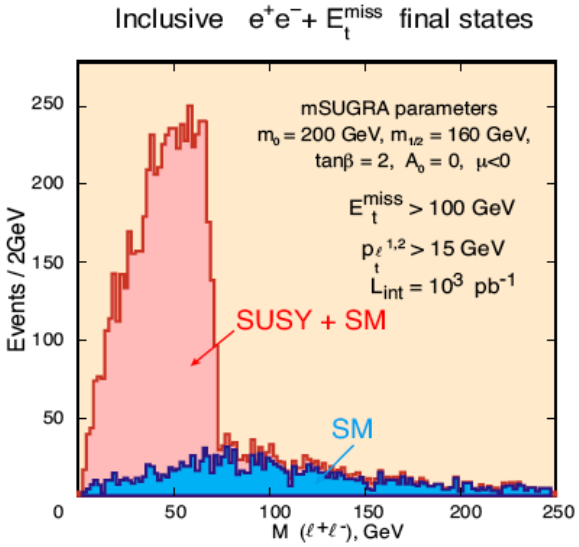

Figure 3.13: The edge in the $\ell\bar{\ell}$ invariant mass spectrum reflects the $\widetilde{\chi}^0{}_2 \rightarrow \ell\bar{\ell}\widetilde{\chi}^0{}_1$ production and decay.

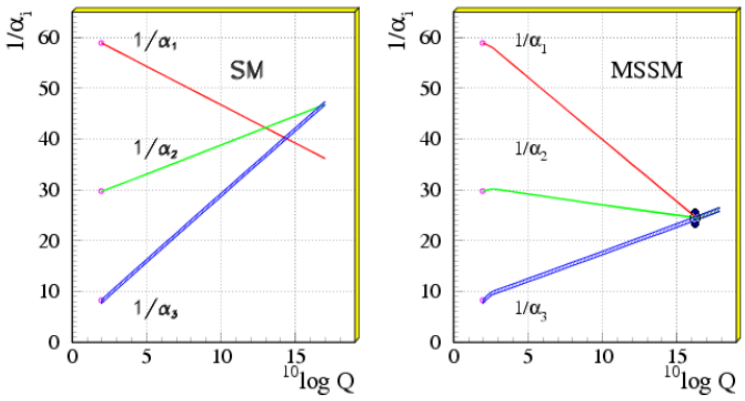

Figure 3.14: In the left: Gauge coupling unification in non-SUSY GUTs. On the right: Gauge coupling unification SUSY GUTs.

3.4.2 Extra dimensions and new vector boson high mass states

The theoretical and phenomenological landscape of searches for physics beyond the Standard Model extends to a multitude of exotic tendencies today in collider physics. Several theories require for extra space-time dimensions scenarios and supersymmetric ones, as previous discussed. The experimental problem is that the final states and signatures of the models are very similar, and, hence, an additional challenge is to distinguish the phenomena belonging to each of them.

Models with heavy vector bosons

Many superstring-inspired[57][58] and unified theories (GUTs)[59], as well as dynamical symmetry breaking[60] and "little Higgs"[63] models predict the existence of additional heavy neutral gauge bosons (Z′). There aren't, at the moment, theoretical predictions on Z′ mass scale but only lower limits of the order of $600 - 900$ GeV/c^2. LHC will investigate Z′ in mass range up to $1 - 5$ TeV/c^2 for $Z' \rightarrow \mu^-\mu^+$ and $Z' \rightarrow e^-e^+$ decay channels.

Randall-Sundrum models

Randall-Sundrum (RS) models predict to warped extra dimensions, hypothesized by Lisa Randall and Raman Sundrum[61][62]. One additional spatial

dimension is considered by the models, where the fifth dimensions is warped by the branes. The branes extend to infinit in the usual three spatial dimensions, but they are so thin in the warped direction to be approximated by delta functions in high energy range. The collider physics phenomenology assuming warped extra dimensions is based upon a specific model called RSI. This model considers the extradimension as compactified to a circle of circumference $2L$, closed by identifying points by $y \rightarrow -y$. This means that the fifth dimension consists into two mirror copies of a curved 5D space extending from $y = 0$ to $y = L$.

At TeV scale, the SM, in RSI, is replaced by a new effective theory in which gravity is still very weak, but there are exotic heavy spin-two particles, that are excited states of Kaluza-Kline (KK) graviton. The KK gravitons, at LHC, would be seen as di-fermion or di-boson resonances, whose width is proportional to $c = k/M$ ratio (Figure 3.15).

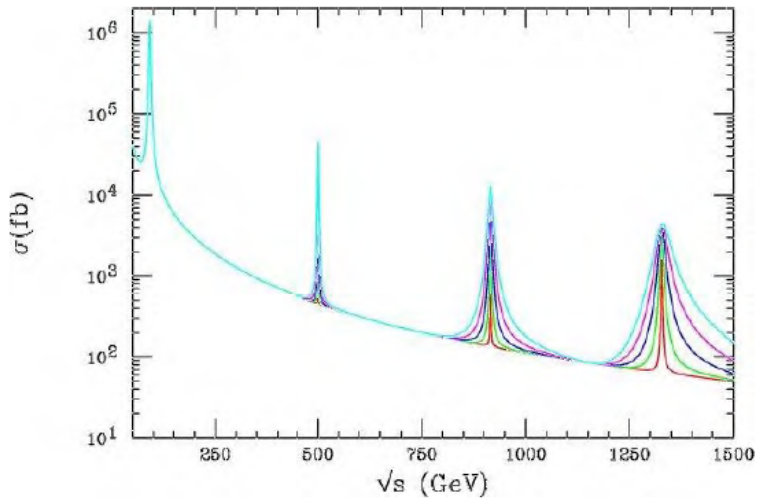

Figure 3.15: The cross section for $e^-e^+ \rightarrow \mu^-\mu^+$ including the exchange of KK gravitons in the RSI model. The narrowest resonances correspond to $k/M = 0.05$, the widest to $k/M = 0.14$.

3.4.3 Technicolor theories

An alternative to the Higgs mechanism of the Standard Model is advanced by Technicolour (TC). This theory introduce in the particle physics scenario

a new strong force, QCD-like, acting on technifermions, and providing a dynamical nature to Electroweak Symmetry Breaking. It acts at an energy scale $\Lambda_{TC} \sim \nu_{weak} = 246GeV$. N_D technifermion doublets condensate yield the pseudo-Goldstone bosons π_{TC}, together with a wide spectroscopy of excited technimesons, such as ρ_{TC} and ω_{TC} of spin 1.

CMS attenction, in this scenario, will be focused on the study of $\rho_{TC} \rightarrow$ W + Z decay channel in order to search the ρ_{TC} meson.

Chapter 4

Study of the inclusive process $\mathbf{pp \to Z + X \to \mu^- \mu^+ + X}$ and cross section measurement

The inclusive process $pp \to Z + X$ will be one of the first processes to be studied at the LHC from the very early phase of data-taking, thanks to its relatively large cross section and clear signature. In particular, its lepton decay channels, $Z + X \to \ell\bar{\ell} + X$, will be very useful because of the following reasons:

- these physics channels are well known from previuos studies and, hence, they will provide a check of the Standard Model predictions at TeV energy scale. They will be an interesting benchmark to unveil the potential presence of new physics at such energy range. For example, an anomaly in the rate of ZZ and $Z\gamma$ production may points out the existence of triple neutral bosons coupling like $ZZ\gamma$ and $Z\gamma\gamma$;

- some theoretical models beyond the SM predict the existence of heavy neutral bosons (Z') or resonances at the TeV scale. The discovery of such phenomena, if they exist, could be established through the detection of events with two leptons in the final state with invariant mass peaking at a given mass resonance;

- the Higgs boson decay into ZZ^* will be the benchmark process in intermediate and high mass regions. The $H \to ZZ^* \to \ell\bar{\ell}\ell\bar{\ell}$ decay would be the golden channel for Higgs observation.

- these channels will provide a precise measurement of the pp luminosity from the startup of the machine;

- they will be used to calibrate the detector and estimate its efficiencies, since their experimental signature is very clear.

In this thesis work a method for the analysis of the Z $\rightarrow \mu^-\mu^+$ physics channel is presented together with a measurement of the inclusive pp $\rightarrow$ Z+$X \rightarrow \mu^-\mu^+ + X$ process cross section. The analysis is performed according to a method based on a simultaneous fit of the yield of $Z \rightarrow \mu^-\mu^+$ events and of the average reconstruction muon efficiencies in the tracker and in the muon system, as well as the efficiency of the isolation cut appied to select events and HLT efficiency. This kind of analysis has been thought to be applicable directly on collision data, also of low statistics, and therefore it will allow to achieve reliable measurement already from the very first data taken at the LHC.

In the following sections we will present a short introduction to the production process of Z boson and its decay into a muon pair and then we will describe all the analysis steps performed in order to measure the process cross section and the involved efficiencies.

4.1 Study of the signal Z $\rightarrow \mu^-\mu^+$

The Z creation in a pp collision takes place from the annihilation of a $q\overline{q}$ pair, where $\overline{q}$ is sea-quark and the q may be either valence or sea quark (Figure 4.1). Since a valence quark has on avarage a momentum greater than sea quark/anti-quark, and the $\overline{q}$ is certainly a sea-quarkthe Z momentum results to have a non-zero longitudinal component. For this reason, most of the Z bosons are produced in forward region. The distribution of kinematic quantities m, p_T , y and ϕ for the Monte Carlo Z are plotted in Figures 4.2a, 4.2b, 4.2c and 4.2d, respectively.

Plots in Figure 4.3 show the p_T, η and ϕ distributions for the MC muons which are the final state of Z decays. MC muons are produced mainly in the plane orthogonal to the beam direction: η distribution is more populated in $\eta = 0$ region as in Figure 4.3b.

4.2 Analysis method description

The purpose of this analysis is to determine the yield of the produced Z $\rightarrow \mu^-\mu^+$ events, corrected by the muon detector efficiency and the track reconstruction efficiency as well as the efficiencies of the isolation cut and HLT. All these estimates come directly from the data without any estimate from Monte Carlo (MC).

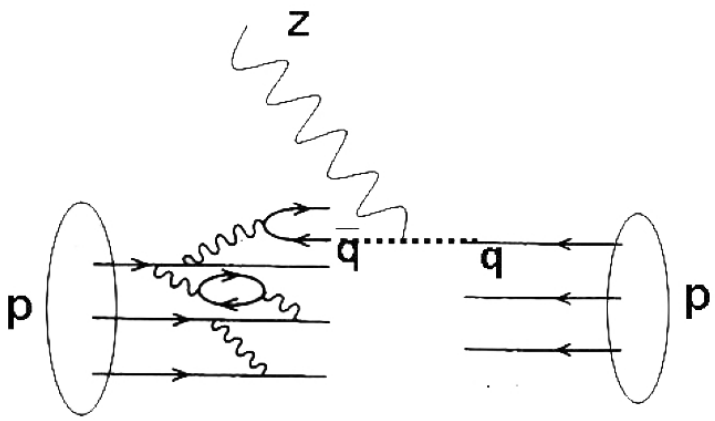

Figure 4.1: Annihilation of a "valence" quark and a "sea" quark into a Z boson. The valence quark momentum is, on average, greater than sea quark one, resulting in a forward directed Z boson.

4.2.1 The signal

The $Z \rightarrow \mu^{-}\mu^{+}$ events reconstructed from pair of muons (*di-muons*) of opposite charge. Muon candidates are classified according to the type of tracks they are associated to. They can be reconstructed in the central tracker (*tracker tracks*), or in the muon detector (*standalone muons*). If an internal and an external tracks are matched, they are combined into a *global muon*. Figures 4.4 show a schematic image of the three kinds of reconstructed muons.

For our analysis, the reconstructed Z events are classified into four statistically indipendent categories with a reconstructed $Z \rightarrow \mu^{-}\mu^{+}$:

- $Z_{\mu\mu}$, built from a pair of muons both global and isolated. This category is split into two samples which are statistically independent:
  - $Z_{\mu\mu}^{2HLT}$, both of muons are global, isolated and matched to HLT trigger primitive;
  - $Z_{\mu\mu}^{1HLT}$, both of muons are global and isolated, but only one of them is HLT matched;
- $Z_{\mu s}$ built from one isolated, HLT matched, global muon and one isolated standalone muon;

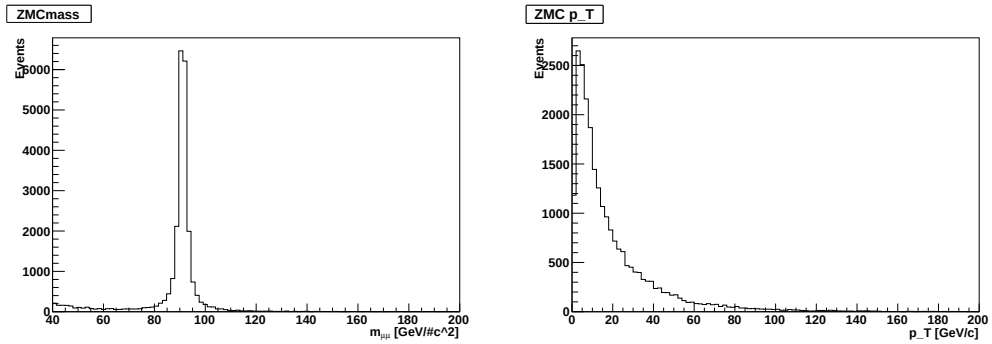

(a) mass (b) p_T

(c) y (d) ϕ

Figure 4.2: Distribution of kinematic quantities of Z Monte Carlo events: (a) mass m, (b) transvers momentum, p_T, (c) rapidity y and (d) azimuthal angle ϕ.

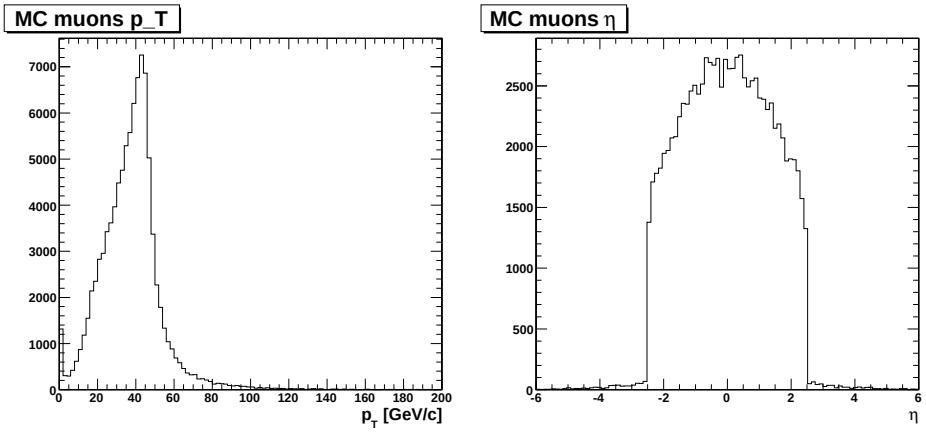

(a) p_T (b) η

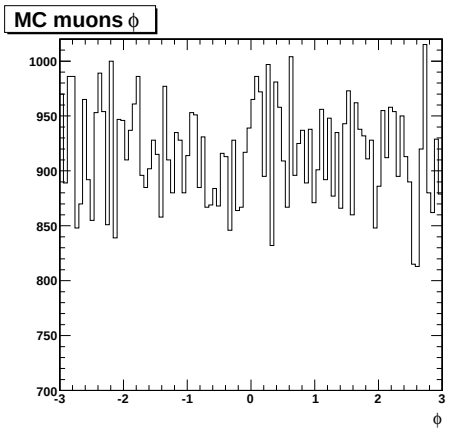

(c) ϕ

Figure 4.3: Distribution of kinematic quantities of Monte Carlo muons coming from Z decay: (a) transvers momentum, p_T, (b) pseudorapidityrapidity η and (c) azimuthal angle ϕ.

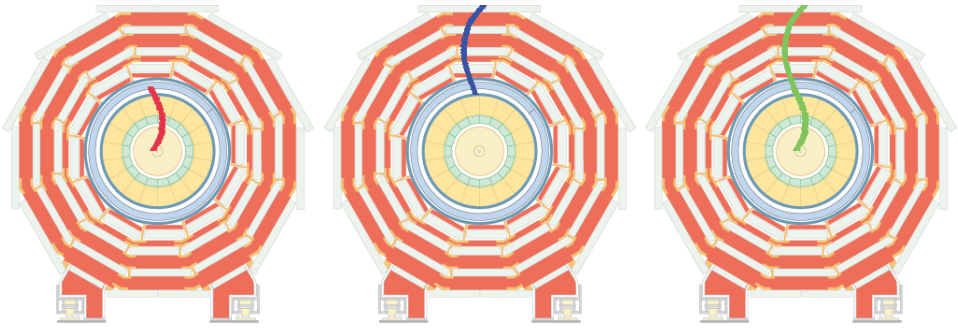

(a) Tracker track (b) Standalone track (c) Global muon

Figure 4.4: Muon candidates reconstruction classification: (a) tracker track, p_T, (b) standalone track and (c) global muon.

- $Z_{\mu t}$ built from one isolated, HLT matched, global muon and one isolated tracker track;

- $Z_{\mu\mu}^{non\ iso}$ built from a pair of global muons, where at least one is *non* isolated and at least one is HLT matched.

The selection of Z candidates and their classification in the categories described above is made in the following way: if a Z candidate matches all the criteria of the first category, it belongs to it and it is excuded from the others; if it does not fall in the first category but in the second, it is excluded from the third and from the fourth, and so on. This procedure allows to construct four mutually exclusive event samples, which are not-overlapping and, hence, statistically indipendent. If more than one pair of muons reconstruct a Z candidate in a unique event, they are all included in the mass spectrum resulting in a combinatorial background.

For each sample, we produce a binned muon invariant mass spectrum and perform a binned χ^2 fit simultaneously on all the categories in order to extract the Z yield and the average efficiencies.

For each category we introduce the differential event yields for signal plus background with the following Probability Density Functions (PDF):

$$\frac{\mathrm{d}N_{\mu\mu}}{\mathrm{d}m} = f_{\mu\mu}(m) = N_{\mu\mu} f_{peak}(m) \quad (4.1)$$

$$\frac{\mathrm{d}N^{2HLT}_{\mu\mu}}{\mathrm{d}m} = f^{2HLT}_{\mu\mu}(m) = N^{2HLT}_{\mu\mu} f_{peak}(m) \quad (4.2)$$

$$\frac{\mathrm{d}N^{1HLT}_{\mu\mu}}{\mathrm{d}m} = f^{1HLT}_{\mu\mu}(m) = N^{1HLT}_{\mu\mu} f_{peak}(m) \quad (4.3)$$

$$\frac{\mathrm{d}N_{\mu s}}{\mathrm{d}m} = f_{\mu s}(m) = N_{\mu s} f^{s}_{peak}(m) + b_{\mu s}(m) \quad (4.4)$$

$$\frac{\mathrm{d}N_{\mu t}}{\mathrm{d}m} = f_{\mu t}(m) = N_{\mu t} f_{peak}(m) + b_{\mu t}(m) \quad (4.5)$$

$$\frac{\mathrm{d}N^{non\ iso}_{\mu\mu}}{\mathrm{d}m} = f^{non\ iso}_{\mu\mu}(m) = N^{non\ iso}_{\mu\mu} f_{peak}(m) + b^{non\ iso}_{\mu\mu}(m) \quad (4.6)$$

The terms $N_{\mu\mu} = N^{2HLT}_{\mu\mu} + N^{1HLT}_{\mu\mu}$, $N_{\mu s}$, $N_{\mu t}$ and $N^{non\ iso}_{\mu\mu}$ are the events yields for each category, and they can be expressed in terms of Z production yield, $N_{\mathrm{Z}\to\mu^-\mu^+}$ and average efficiencies for muon reconstruction in the tracker (ϵ_{trk}) and in the muon system as stand-alone track (ϵ_{sa}) as well as the average efficiencies of the isolation cut (ϵ_{iso}) and HLT (ϵ_{HLT}):

$$N^{2HLT}_{\mu\mu} = N_{\mathrm{Z}\to\mu^-\mu^+}\epsilon^2_{HLT}\epsilon^2_{iso}\epsilon^2_{trk}\epsilon^2_{sa} \quad (4.7)$$

$$N^{1HLT}_{\mu\mu} = 2N_{\mathrm{Z}\to\mu^-\mu^+}\epsilon_{HLT}(1-\epsilon_{HLT})\epsilon^2_{iso}\epsilon^2_{trk}\epsilon^2_{sa} \quad (4.8)$$

$$N_{\mu s} = 2N_{\mathrm{Z}\to\mu^-\mu^+}\epsilon_{HLT}\epsilon^2_{iso}\epsilon_{trk}(1-\epsilon_{trk})\epsilon^2_{sa} \quad (4.9)$$

$$N_{\mu t} = 2N_{\mathrm{Z}\to\mu^-\mu^+}\epsilon_{HLT}\epsilon^2_{iso}\epsilon^2_{trk}\epsilon_{sa}(1-\epsilon_{sa}) \quad (4.10)$$

$$N^{non\ iso}_{\mu\mu} = N_{\mathrm{Z}\to\mu^-\mu^+}(1-(1-\epsilon_{HLT})^2)(1-\epsilon^2_{iso})\epsilon^2_{trk}\epsilon^2_{sa} \quad (4.11)$$

The factor 2, which is involved in $N^{1HLT}_{\mu\mu}$, $N_{\mu s}$ and $N_{\mu t}$ is due to the fact that the specific criterium can be satisfied by the first or the second muon of the pair. The two cases are indipendent and have to be summed.

We have factorized the efficiency terms in equations (4.7) to (4.11) since we have assumed the effects of correlation between the two muon to be neglected. This assumption is justified by an extimation of the correlation perferomed in the CMS internal note[67]: it is about 0.11%.

We assume that the peak shape in $Z^{2HLT}_{\mu\mu}$, $Z^{1HLT}_{\mu\mu}$, $Z_{\mu t}$ and $Z^{non\ iso}_{\mu\mu}$ categories is the same, and it can be extracted directly from the data rather then parametrize it. Hence, we take as distribution for $f_{peak}(m)$ the normalized histogram of the di-muon invariant mass spectrum in the $Z_{\mu\mu}$ sample, where the background is neglegible.

The model of the Z mass peak shape for Z reconstructed from a global muon and a standalone muon ($f^{s}_{peak}(m)$) has been parametrized initially as

a Gaussian, since resolution effects hide the Z peak shape and the statistcs is low. The implementation of a different way to model the Z peak shape in the $Z_{\mu s}$ category is integral part of this thesis work: we have determined the PDF of the distribution of signal events in this sample considering the $Z_{\mu\mu}$ candidates and taking, for one of the two muons, the momentum measured from the muon detector track fit only in order to simulate a pair o muons of which one is standalone and one is global. Each event of the $Z_{\mu\mu}$ sample is counted only once by chosing alternatively the first (second) muon for even (odd) events respectively. The goal of considering such description for the signal shape is that it is entirely data-driven and, furthermore, it allows to reduce the number of parameters to fit. Figure 4.5 compares the signal shape of the selected $Z_{\mu s}$ candidates and the shape obtained from $Z_{\mu\mu}$ sample. The results of the two kinds of fit are compared and reported in Table 4.4 in Section 4.2.5.

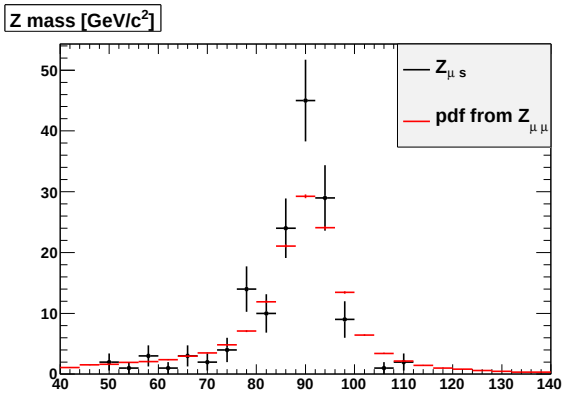

Figure 4.5: Invariant mass distribution for selected $Z_{\mu s}$ candidates in signal events (black points) superimposed to the pdf (red points) determined from $Z_{\mu\mu}$ candidates by using , for one of the muons in thepair, the momentum of the associated standalone muon. The pdf is normalized to the invariant mass distribution of $Z_{\mu s}$ candidates.

4.2.2 The Background

Signal shapes are derived by a data-driven method as we have seen. The backgrounds functions, instead, are modelled as product of an exponential times a polynomial of different order according to the specific sample, if the background is not neglegible:

- for Z reconstructed from two global muons, $Z_{\mu\mu}$, we assume negligible background from MC estimates: we expect $\sim 0.1\%$ of background from non-Z processes, and 0.030% from combinatorial background in Z events producing fake di-muon combinations;

- in the distribution for Z reconstructed from a global muon and a tracker track, $Z_{\mu t}$, the background dominates and we model it in this sample as the product of an exponential times a second order polynomial:

$$b_{\mu t}(m) = N^b_{\mu t}(1 + a_1 m + a_2 m^2)e^{-\alpha m} \ ; \tag{4.12}$$

- also in the last sample, the $Z^{non\ iso}_{\mu\mu}$, background can't be neglected, and it is modelled as the product of an exponential with a first order polynomial:

$$b^{non\ iso}_{\mu\mu}(m) = N^{b\ non\ iso}_{\mu\mu}(1 + b_1 m)e^{-\beta m} \tag{4.13}$$

- in the sample filled from Z reconstructed from a global muon and a standalone muon, $Z_{\mu s}$, the background can be parametrized simply by an exponential:

$$b_{\mu s}(m) = N^b_{\mu s}e^{-\gamma m} \ , \tag{4.14}$$

  but for low integrated luminosity values, it can also be neglected.

In this thesis work the sources of background which are taken into account in the analysis are those Z candidates reconstructed from $W \to \mu\nu$, QCD, and $t\bar{t}$ samples.

Among $W \to \mu\nu$ events, a pair of muons, which can reconstruct a di-muon, can be formed by a muon coming from W decay and another muon coming from the decay of an hadron like B, π or K. In analogous way di-muon pairs are produced by *top* quark decay in $t\bar{t}$ sample and in QCD sample, which includes processes such as pp $\to q\bar{q}j$, pp $\to qgj$ and pp $\to q\bar{q}j$, a muon coming from the jets j can be reconstructed as muons coming from Z decay.

4.2.3 Data samples

In the analysis performed in this work, we have used the data samples of the official, so called "Summer08", Monte Carlo production[1], generated according to the standard CMS generator, simulation and reconstruction chain, assuming a centre of mass energy $\sqrt{s} = 10$ TeV and ideal conditions of the detector. The considered samples are:

[1]For more detail on Summer08 production refer to the ElectroWeak Summer08 page[64]

- $pp \rightarrow Z/\gamma^* X \rightarrow \mu^+\mu^- X$
- $pp \rightarrow W^{\pm} X \rightarrow \mu^{\pm}\nu_{\mu} X$
- QCD jets events containing at least one muon with $p_t > 15\text{GeV}/c$
- $t\bar{t}$.

Table 4.1 shows informations about the data samples used in our analysis. For each one, the number of events, the product of the leading order (LO) cross section (σ_{LO}) times the generator efficiency (ϵ_{filter}) and the equivalent integrated luminosity ($\int L\mathrm{d}t$) are indicated.

Sample	**Events**	$\sigma \times \epsilon_{\text{filter}}$ **(pb)**	$\int \mathcal{L}\mathrm{d}\mathbf{t}(\mathbf{pb^{-1}})$
$pp \rightarrow ZX \rightarrow \mu^+\mu^- X$	1,062,500	627	1694.34
$pp \rightarrow W^{\pm} X \rightarrow \mu^{\pm}\nu_{\mu} X$	1,091,841	8198	133.17
QCD jets, muon $p_t > 15$ GeV/c	5,479,643	121,675	45
$t\bar{t}$	147,000	241.7	608

Table 4.1: Analyzed data samples.

4.2.4 The event selection

We defined selection criteria in order to select signal events and reject background ones.

Muons coming from Z decays have high p_T, as we have seen in the plot of the p_T distribution for signal muons (Figure 4.3c). For this distribution we require, for our selection that, both muon candidates, either global or standalone muons, or tracker tracks, must have a $p_T > 20$ GeV/c.

The muons interesting for by our analysis are produced mainly close to the plane orthogonal at the beam pipe, i.e. for values of η around 0. We choose to set a cut on η in order to select muons which are reconstructed in the region where the tracker is more efficiencient. Figure 2.9 shows a quite constant trend of tracker efficiency for muon track reconstruction until $|\eta| < 2$ for muons, over this region the smaller coverage of pixel forward disks leads to a fast decrease of the global track reconstruction efficiency. Hence, in order to achieve a high reconstruction efficiency and also to avoid edge effects we choose to take muons within $|\eta| < 2$.

In order to better study the background distribution we take a large invariant mass range in our selection: 20 GeV/$c^2 < m_{\mu^-\mu^+} < 200$ GeV/c^2.

A further request is made by introducing a new variable: the *isolation*. We describe it in more detail in Section 4.3, considering both the contributions

coming from the tracker and the calorimeters. At this step of the study we limit the definition of th he isolation variable as the sum of the transverse momenta of the charged particle tracks with p_T greater than a threshold $p_{T\ \mathrm{min}}$, which lie within a cone around the muon momentum direction at vertex of size $\Delta R_{\mathrm{min}} < \Delta R < \Delta R_{max}$, where $\Delta R = \sqrt{(\Delta\phi)^2 + (\Delta\eta)^2}$:

$$I_{tkr} = \sum_{\substack{p_T^{(i)} > p_{T\ \mathrm{min}} \\ \Delta R > \Delta R_{\mathrm{min}}}}^{\Delta R < \Delta R_{\mathrm{max}}} p_T^{(i)} \ . \tag{4.15}$$

We request tracker isolation to be smaller than 3 GeV/c, with isolation variable defined considering $\Delta R_{min} = 0.015$, $\Delta R_{max} = 0.3$ and $p_{T\ \mathrm{min}} = 1.5$ GeV/c. We will see in Section 4.3 how the introduction of a different isolation variable, including calorimeter contributions, leads to an improvement in selection performances.

Events are required to satisfy HLT single-muon criteria. The HLT trigger matching requirement varies according to the definition of each Z category.

The kinematics cuts applied for our analysis are listed in Table 4.2.

Selection cuts
$p_T > 20$ GeV/c
$\eta < 2$
I_{trk} <3 GeV/c
20 GeV/$c^2 < m_{\mu^-\mu^+} < 200$ GeV/c^2

Table 4.2: Summary of the selection cuts applied in order to preserve signal events and reject background ones.

Figures 4.6 to 4.10 show the invariant mass distributions of the selected Z candidates for each category considered in the analysis and previously described. The plots refer to an input data sample of signal plus background events corresponding to an equivalent integrated luminosity of $\int Ldt = 45\ \mathrm{pb}^{-1}$.

Table 4.3 lists the number of selected candidates for signal and background for each category in the rescricted range 60 GeV/$c^2 < m_{\mu^-\mu^+} < 120$ GeV/c^2, where the fit is performed.

4.2.5 Fit Results

The fit strategy adopted, in this thesis work, is based on the determination of the $Z \to \mu^-\mu^+$ yield and the average muon reconstruction efficiencies in

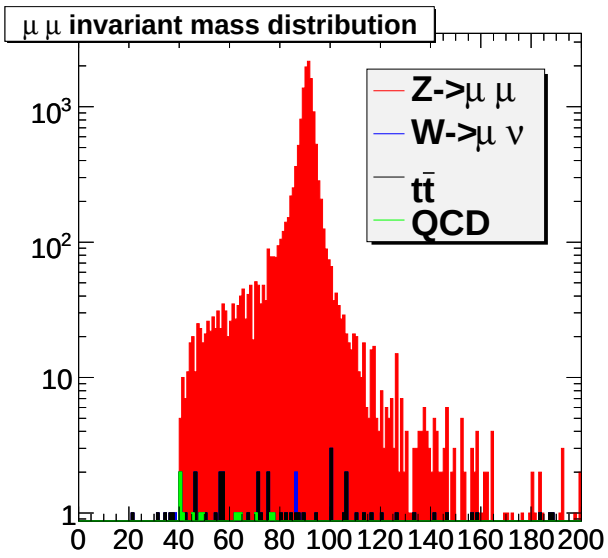

Figure 4.6: Invariant mass distribution of $Z_{\mu\mu}^{2HLT}$ candidates for signal and background events corresponding to an equivalent luminosity of 45 pb^{-1}.

MC sample	$Z_{\mu\mu}$	$\mathbf{Z_{\mu s}}$	$\mathbf{Z_{\mu t}}$	$\mathbf{Z_{\mu\mu}^{non\ iso}}$
$Z \to \mu^+\mu^-$	15870 ± 130	49 ± 7	320 ± 20	640 ± 30
$W^\pm \to \mu^\pm\nu_\mu$	2 ± 1	4 ± 2	320 ± 20	34 ± 6
$t\bar{t}$	24 ± 5	1 ± 1	90 ± 9	40 ± 6
QCD	9 ± 3	1 ± 1	330 ± 20	1090 ± 30
$Z \to \tau^+\tau^-$	19 ± 4	No events	69 ± 8	No events

Table 4.3: Number of candidates in each category after the selection with an invariant mass in the range [60-120] GeV/c^2. Here $Z_{\mu\mu} = Z_{\mu\mu}^{1HLT} + Z_{\mu\mu}^{2HLT}$. The separate contributions from signal and background processes are shown. An integrated luminosity of 45 pb^{-1} is assumed.

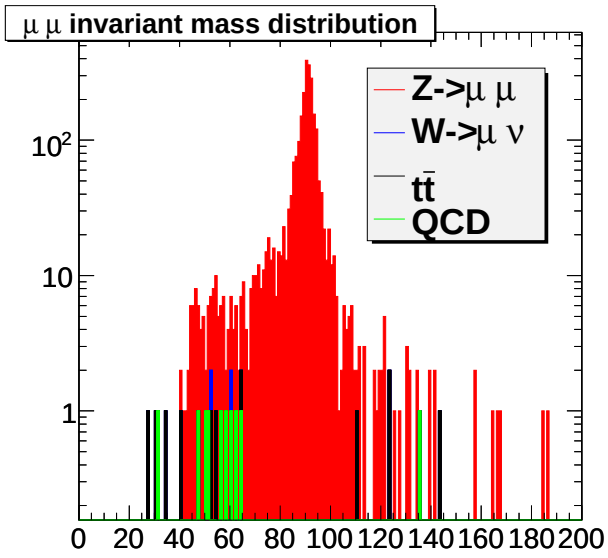

Figure 4.7: Invariant mass distribution of $Z_{\mu\mu}^{1HLT}$ candidates for signal and background events corresponding to an equivalent luminosity of 45 pb^{-1}.

the muon system and in the tracker, and the average efficiencis of isolation cut and HLT, with a simultaneous fit to the invaraniant mass distribution of the five categories of Z candidates. The unknown best fit parameters are obtained throught the least squares method. We construct the **global** χ^2 according to this form:

$$\chi_k^2 = \sum_{i=0}^{N_{bins}^k} \left(\frac{n_i^k - f^k(m_i)}{\sigma_i^k} \right)^2 \tag{4.16}$$

where the k index ($k = 1, 2, 3, 4, 5$) refers to the particular category ($Z_{\mu\mu}^{1HLT}$, $Z_{\mu\mu}^{2HLT}$, $Z_{\mu t}$, $Z_{\mu\mu}^{non\ iso}$ or $Z_{\mu s}$) and the N_{bins}^k is the number of bins in the k-category. The i index labels the particular bin of the histogram which is centred at the mass value m_i, and the n_i^k is the number of entries of the i-th bin. If we want to fit the data with a function of the form $f^k(m)$, hence, the number of entries expected by the theory in the i-th bin is $f^k(m_i)$. At denominator, σ_i^k is the statistical error of the observed number of entries in the i-th bin, according to the Poisson distribution it results $\sigma_i^k = \sqrt{n_i^k}$. If the theory is in good agreement with the data, we expect to have no much difference between n_i^k and $f^k(m_i)$.

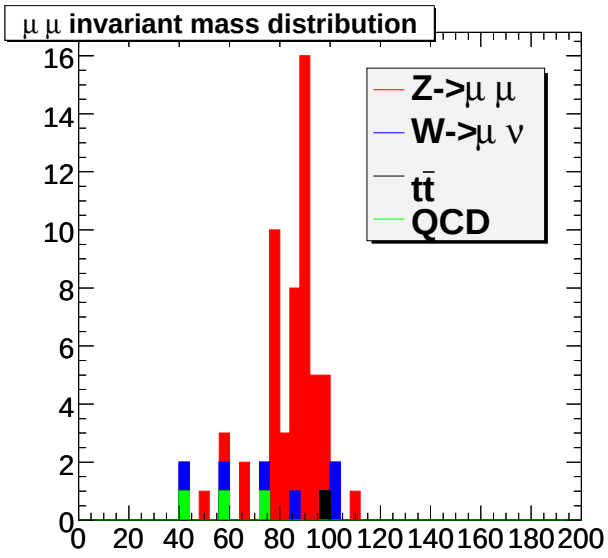

Figure 4.8: Invariant mass distribution of $Z_{\mu s}$ candidates for signal and background events corresponding to an equivalent luminosity of 45 pb^{-1}.

We rewrite the **global** χ^2 making explicit all the terms:

$$\chi^2 = \chi^2_{\mu\mu^{1HLT}} + \chi^2_{\mu\mu^{2HLT}} + \chi^2_{\mu t} + \chi^{2\ non\ iso\ 2}_{\mu\mu} + \chi^2_{\mu s} \tag{4.17}$$

Since we use the di-muon spectrum of the $Z_{\mu\mu}$ category as signal shape model, we remove the first two histograms from the χ^2 form in (4.17) and replace then by the contribution of the total signal yields, $N^{2HLT}_{\mu\mu}$ and $N^{2HLT}_{\mu\mu}$:

$$\begin{aligned}\chi^2 \;=\; & \frac{(N^{2HLT}_{\mu\mu} - N_{Z\to\mu^-\mu^+}\epsilon^2_{HLT}\epsilon^2_{iso}\epsilon^2_{trk}\epsilon^2_{sa})^2}{N^{2HLT}_{\mu\mu}} + \\ & \frac{(N^{1HLT}_{\mu\mu} - 2N_{Z\to\mu^-\mu^+}\epsilon_{HLT}(1-\epsilon_{HLT})\epsilon^2_{iso}\epsilon^2_{trk}\epsilon^2_{sa})^2}{N^{1HLT}_{\mu\mu}} + \\ & \chi^2_{\mu t} + \chi^{2\ non\ iso\ 2}_{\mu\mu} + \chi^2_{\mu s}\ ,\end{aligned}$$

According to this strategy, the fit has been performed on the 45 pb^{-1} signal plus background data sample for both Gaussian and data-driven Z peak shape models for $Z_{\mu s}$ category, already introduced in Section 4.2.1. The fit has been performed in both cases in the mass range 60 GeV/c^2 $< m_{\mu^-\mu^+} <$ 120 GeV/c^2. Figures 4.11 to 4.13 shows the fit results for the new model for

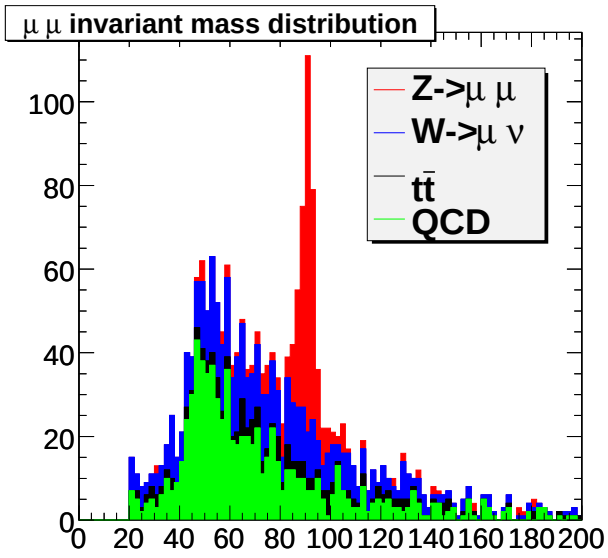

Figure 4.9: Invariant mass distribution of $Z_{\mu t}$ candidates for signal and background events corresponding to an equivalent luminosity of 45 pb^{-1}.

shape of $Z_{\mu s}$ peak, i.e. the pdf extracted by the data, superimposed to the invariant mass distributions of the Z candidates reconstructed in the $Z_{\mu t}$, $Z_{\mu s}$ and $Z_{\mu\mu}^{non\ iso}$ samples. Table 4.4 listed the fit results for the new fit method and also for the old fit method which use a Gaussian to describe the $Z_{\mu s}$ peak shape comparing themselves and with MC truth efficiency values.

We have performed the fit for different statistics, in order to study the performance of the fit at different luminosity scenarios: 5 pb^{-1}, 10 pb^{-1} and 133 pb^{-1}. We list in Table **??** the fit results for different scenarios compared to the fit results of old fit method, i.e that models the Z peak shape as a Guassian. The main fit parameters are also plotted in Figures 4.14, 4.15 and 4.16 for the various considered integrated luminosity values. The fitted cross sections plotted in Figure 4.16 are normalized to the value obtained at the highest luminosity. The parameters determined by the fit are in good agreement with MC truth average values within about 1 to 1.5 σ and they appear to be stable. At 5 pb^{-1}, the fit results are affected by large errors and an initial deviation from the others. This is due to the very low statistics of the $Z_{\mu s}$ sample. An Unbinned Maximum Likelihood fit approach could lead to a better stability as we will see in Section 4.4.

In the following sections we will refer to the fit method as that describing

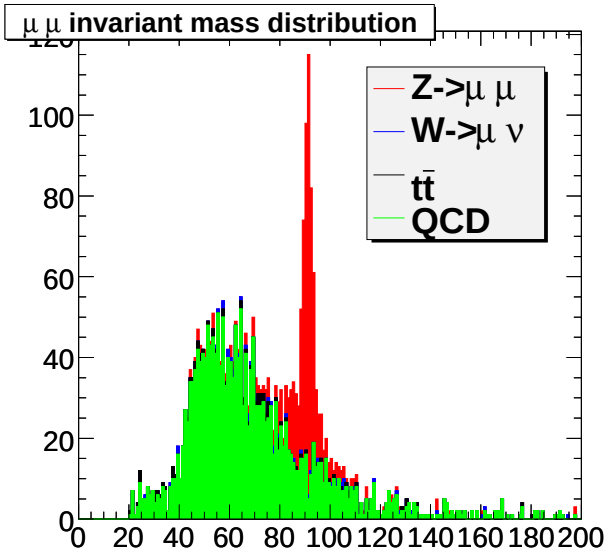

Figure 4.10: Invariant mass distribution of $Z_{\mu\mu}^{non\ iso}$ candidates for signal and background events corresponding to an equivalent luminosity of 45 pb^{-1}.

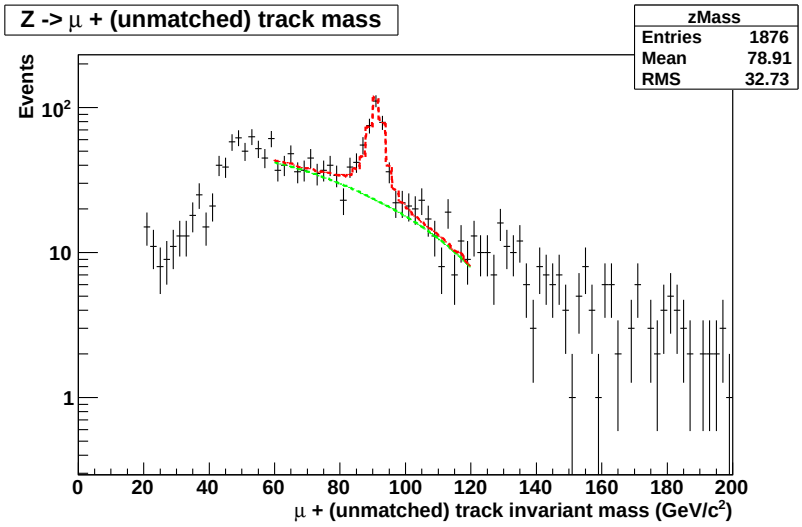

Figure 4.11: Fit curve superimposed to the invariant mass histogram of $Z_{\mu t}$ candidates for a sample corresponding to an integrated luminosity of 45 pb^{-1}.

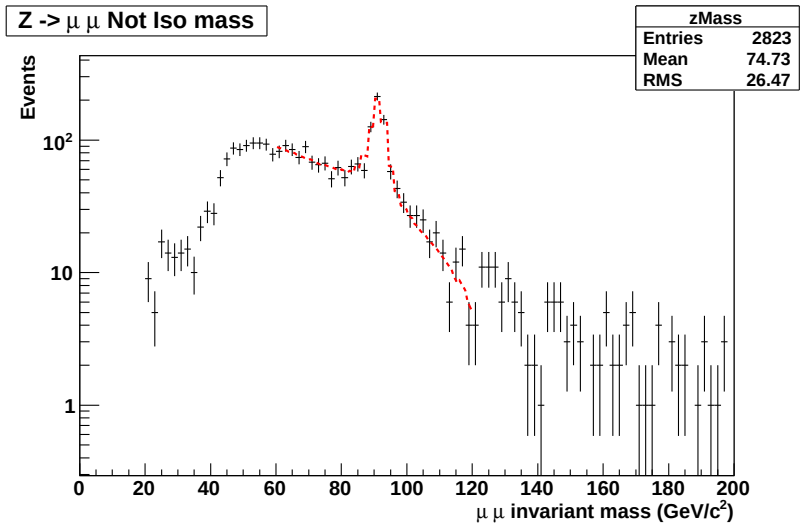

Figure 4.12: Fit curve superimposed to the invariant mass histogram of $Z_{\mu\mu}^{non\ iso}$ candidates for a sample corresponding to an integrated luminosity of 45 pb^{-1}.

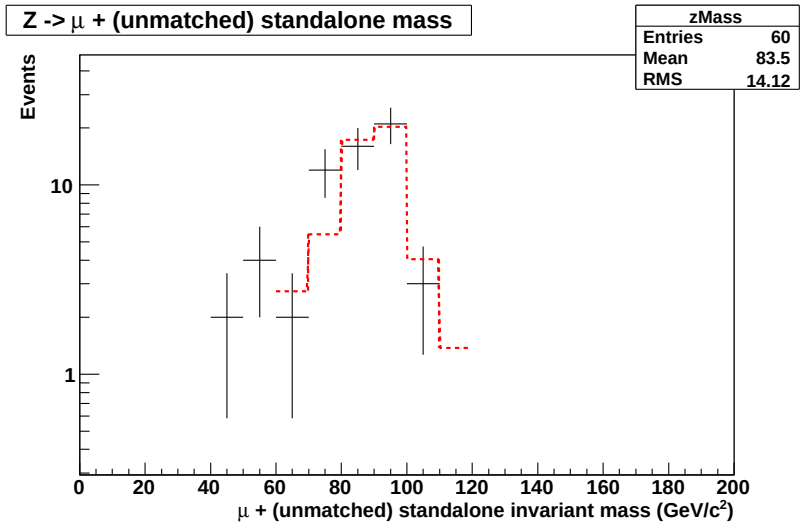

Figure 4.13: Fit curve superimposed to the invariant mass histogram of Z_{μ_s} candidates for a sample corresponding to an integrated luminosity of 45 pb^{-1}.

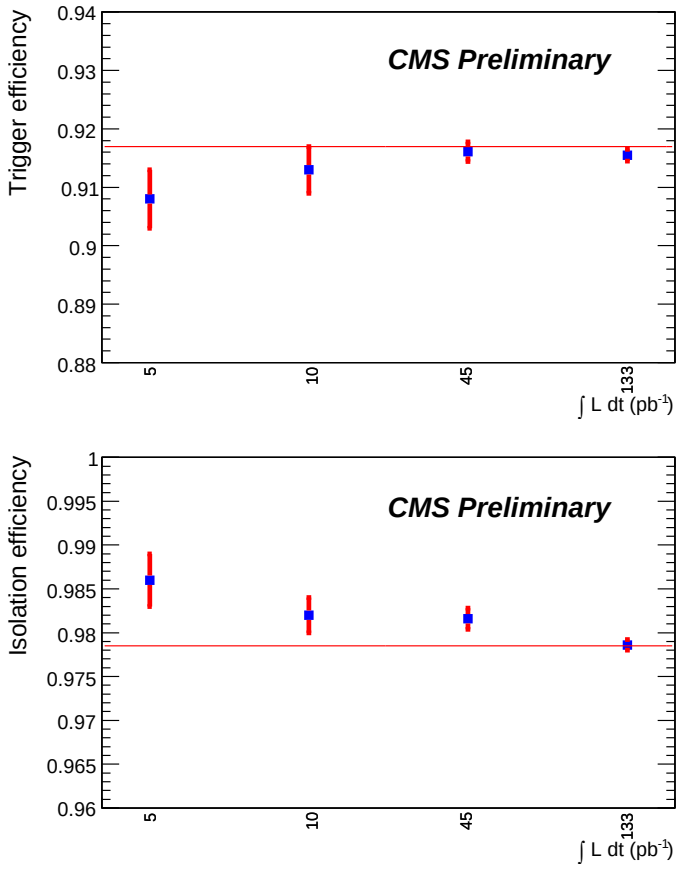

Figure 4.14: Fitted HLT efficiency is reported in the top plot for different integrated luminosity scenarios. In the down plot, fitted isolation efficiency are also reported. The red line shows to the Monte Carlo true value.

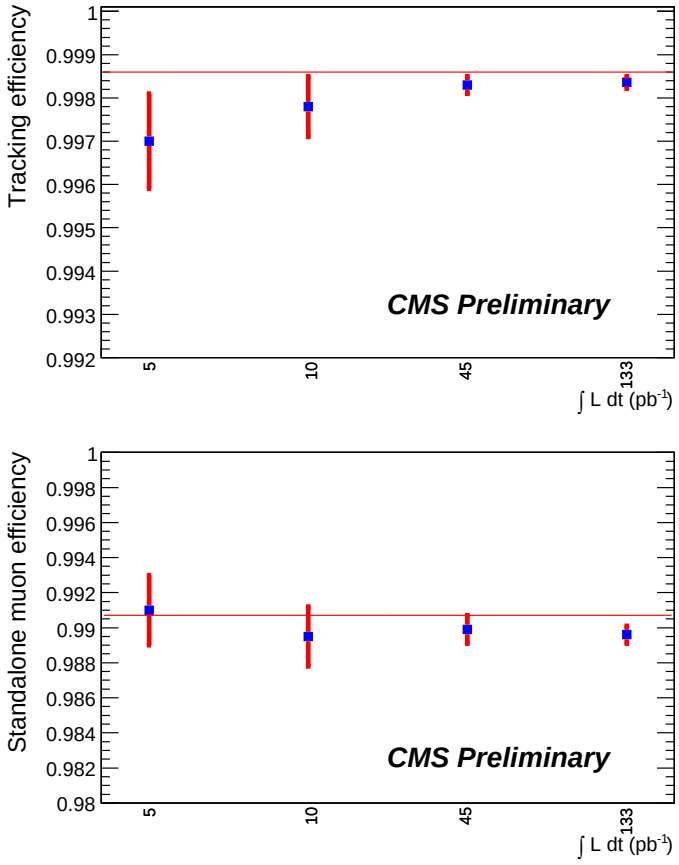

Figure 4.15: Fitted tracker efficiency is reported in the top plot for different integrated luminosity scenarios. In the down plot, fitted standalone efficiency are also reported. The red line refers to the Monte Carlo true value.

	"Data-driven" PDF	Gaussian PDF	MC-truth
$\int Ldt = 45\text{pb}^{-1}$			
ϵ_{HLT}	0.9161 ± 0.0017	0.9161 ±0.0017	0.917 ± 0.002
ϵ_{iso}	0.9816 ± 0.0012	0.9710 ± 0.0012	0.9785 ± 0.0009
ϵ_{sa}	0.9899 ± 0.0008	0.9898 ± 0.0008	0.9907 ± 0.0006
ϵ_{trk}	0.9983 ±0.0002	0.9983 ± 0.0002	0.9986 ± 0.0002
$N_{Z\to\mu^-\mu^+}$	17000 ± 136	17054 ± 136	
χ^2/ndof	1.03708	1.07542	

Table 4.4: Comparison between fit results with the fit model entirly data-driven, described in this work, and the fit model which provide $Z_{\mu s}$ Gaussian peak shape. The fits are performed on a sample corresponding to an integrated luminosity of 45pb^{-1}. MC-truth values of the average efficiencies are also shown for comparison.

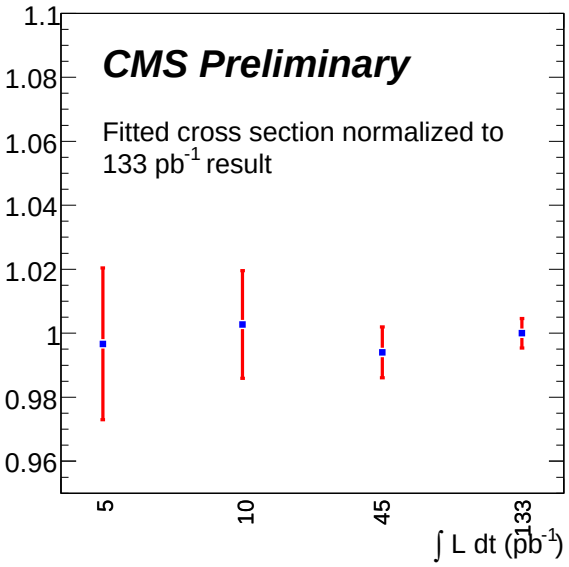

Figure 4.16: Fitted cross sections for different integrated luminosity scenarios. The results are normalized to the 133 pb^{-1} determination.

	"Data – driven" PDF	**"Gaussian" PDF**	**MC – truth**
$\int \boldsymbol{L}\mathbf{d}\boldsymbol{t} = \mathbf{133pb^{-1}}$			
ϵ_{HLT}	0.915 ± 0.001	0.915 ±0.001	0.917 ± 0.002
ϵ_{iso}	0.9787 ± 0.0006	0.9767 ± 0.0007	0.9785 ± 0.0009
ϵ_{sa}	0.9895 ± 0.0005	0.9896 ± 0.0004	0.9907 ± 0.0006
ϵ_{trk}	0.99836 ± 0.00013	0.99874± 0.00013	0.9986 ± 0.0002
$N_{\mathrm{Z}\to\mu^-\mu^+}$	50555 ± 234	50708 ± 233	
χ^2/ndof	1.51032	1.70382	
$\int \boldsymbol{L}\mathbf{d}\boldsymbol{t} = \mathbf{10pb^{-1}}$			
ϵ_{HLT}	0.913 ±0.004	0.913 ±0.004	0.917 ± 0.002
ϵ_{iso}	0.982± 0.002	0.981± 0.002	0.9785 ± 0.0009
ϵ_{sa}	0.9895 ± 0.0017	0.9894 ± 0.0017	0.9907 ± 0.0006
ϵ_{trk}	0.9978 ± 0.0007	0.9981 ± 0.0003	0.9986 ± 0.0002
$N_{\mathrm{Z}\to\mu^-\mu^+}$	3811± 64	3822± 64	
χ^2/ndof	1.4888	1.5299	
$\int \boldsymbol{L}\mathbf{d}\boldsymbol{t} = \mathbf{5pb^{-1}}$			
ϵ_{HLT}	0.908 ±0.005	0.908 ±0.005	0.917 ± 0.002
ϵ_{iso}	0.986± 0.003	0.985± 0.003	0.9785 ± 0.0009
ϵ_{sa}	0.991 ± 0.002	0.991 ± 0.002	0.9907 ± 0.0006
ϵ_{trk}	0.9970 ± 0.0011	0.992 ± 0.003	0.9986 ± 0.0002
$N_{\mathrm{Z}\to\mu^-\mu^+}$	1894± 45	1918± 46	
χ^2/ndof	1.0186	0.982564	

Table 4.5: Comparison between fit results with data-driven signal peak shape and Gaussian peak shape for $Z_{\mu s}$ category. The fits are performed on samples corresponding to an integrated luminosity of 133, 10 and 5 pb^{-1}. MC-truth values of the average efficiencies are also shown for comparison.

the Z peak shape as taken from data, and not as modelled as a Gaussian.

4.3 Muon Isolation

The main sources of muons, in the p_T range of 10÷30 GeV/c, are b and c decays, while low-p_T muons come mostly from K and π decays. Muons coming from these sources are produced in jets and so accompained by nearby particles. For p_T above 30 GeV/c, muons from Z and W producing becomes dominant. These muons are isolated, they haven't nearby particles besides particles from pile-up and from the underlying event.
With the Muon Isolation tool we can distinguish between muons produced in jets and muons coming from heavy particles decays to discriminate signal muons from background ones.
A reduction of events coming from background sources is reached by selecting isolated muons, i.e those muons whose isolation variable is smaller than a cut value, I_{cut}.
The standard tracker isolation (I_{trk}) variable is defined as the Σp_t of tracks inside a cone of size ΔR . Isolation variables in the calorimeters (I_{Ecal} and I_{Hcal}) are defined in the same way but E_t of deposits are considered in the sum.
Figure 4.17 shows the definition of the isolation cone. The axis of the cone is defined as the muon direction at vertex and its geometrical definition is given by the condition:

$$\Delta R_{min} < \Delta R < \Delta R_{max}$$

where ΔR, the distance between the deposit and the cone axis, is defined in pseudorapidity-azimuthal angle space as:

$$\Delta R = \sqrt{(\Delta\eta)^2 + (\Delta\phi)^2}$$

The contribution of p_T and E_T of muon itself is removed by considering a "veto cone" of size ΔR_{min} around the muon trajectory propagated to the calorimeters considering the muon curvature in CMS magnetic field. ΔR_{min} has been fixed at 0.015.

Among the four categories of events with a reconstructed $Z \to \mu^+\mu^-$ candidates, $Z_{\mu t}$ is the one affected by the larger background. The main contributions arise from $W \to \mu^+\nu^-$ and QCD. We have investigated the definition of an optimized isolation variable with better performance in background

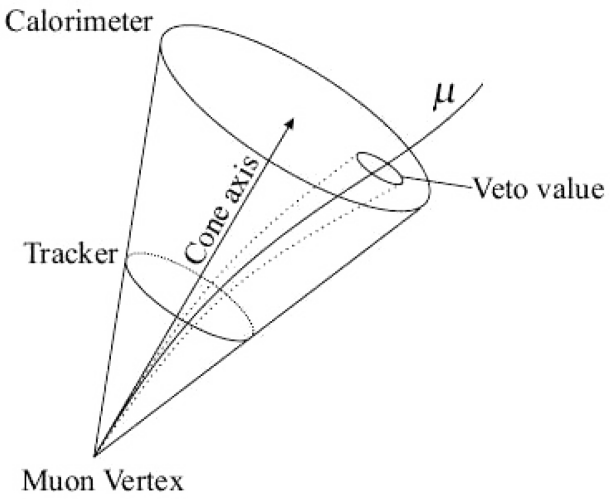

Figure 4.17: Isolation cone with its axis and the veto cone, constructed around the muon trajectory propagated to the calorimeters

rejection than tracker one.
We have first studied the optimal threshold and cone size for each isolation variable. Then we have studied a combined isolation variable using both calorimeter and tracker systems. The optimization procedure has been done optimizing the rejection of $W \to \mu\nu$ and QCD backgrounds in the $Z_{\mu t}$ sample, obtaining identical results. Only those for the former background are shown in the following.

4.3.1 Threshold and cone size optimizations

Z reconstructed from one global muon and one track are taken into account and an the standard event selection is applied on both muon and track as in Section 4.2.4.
Figure 4.18a shows, for each isolation variable, the $W \to \mu\nu$ background efficiency with respect to the $Z \to \mu^+\mu^-$ signal efficiency, applying different selection cuts on I_{trk}, I_{Ecal} and I_{Hcal} for different fixed values of thresholds.
There is no significant variation of the I_{trk} performances with respect to a particular choice of the threshold. We choose to fix p_T threshold at 1 GeV/c, while for I_{Ecal} and I_{Hcal}, E_t thresholds of 0.2 GeV and 0.5 GeV are to be preferred, respectively.
The following step consists of performing the cone-size optimization. Fig-

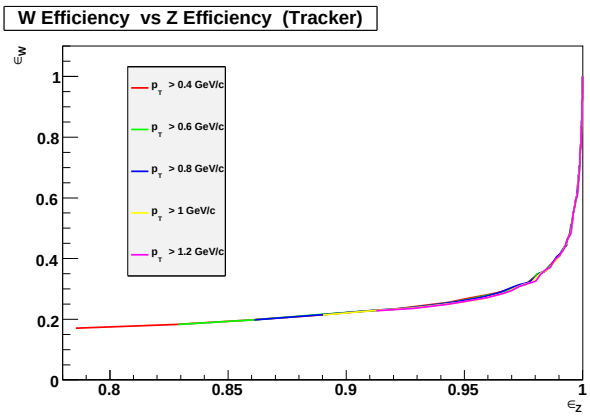

(a) I_{trk}

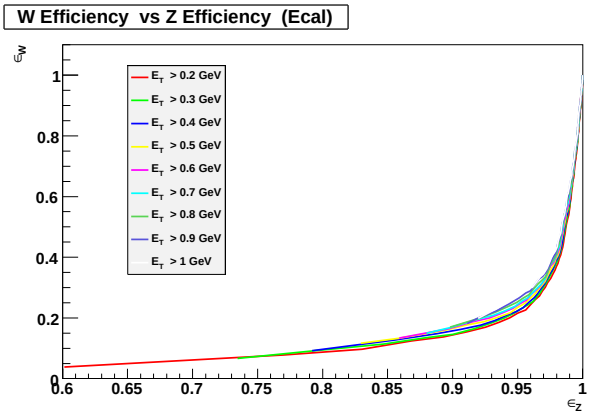

(b) I_{Ecal}

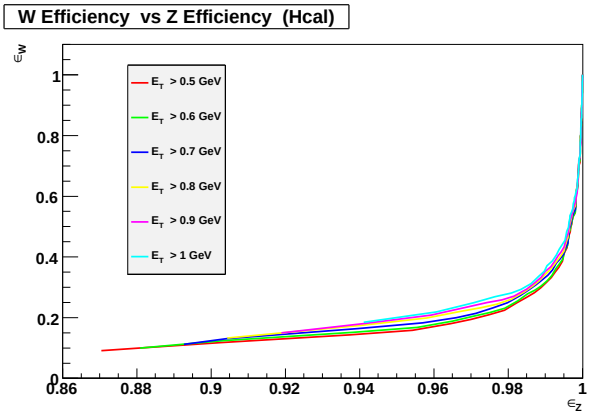

(c) I_{Hcal}

Figure 4.18: $W_{\mu\nu}$ background efficiency vs $Z_{\mu\mu}$ signal efficiency for selection cuts on the variables I_{trk}, I_{Ecal}, I_{Hcal}, at different fixed threshold values and with fixed cone size of $\Delta R_{max} = 0.2$).

ure 4.19 shows, for each isolation variable, the $W_{\mu\nu}$ background vs the $Z_{\mu\mu}$ signal efficiency curves at different fixed cone sizes.

The procedure is the same as for the thresholds choice.

The best performances are reached for $\Delta R_{max} = 0.2$ for I_{trk}, and 0.25 for I_{Ecal} and I_{Hcal}.

4.3.2 Combined isolation

Considering calorimeter selection requirements together with tracker isolation requirements, it is possible to improve background rejection power. The combined isolation variable considered is defined as the weighted sum of the tracker and calorimeter contributions to isolation according the following parametrization:

$$I = \alpha\left[\frac{(1+\beta)}{2}I_{Ecal} + \frac{(1-\beta)}{2}I_{Hcal}\right] + (1-\alpha)I_{Tkr} \tag{4.18}$$

The parameter α is the weight of the calorimeter isolation with respect to the tracker, while β mesures the asymmetry between I_{Ecal} and I_{Hcal} contributions.

In Figure 4.20, the parameter β is fixed at 0 and α varies in the range [0, 1]. It is clear that there is an important difference whether or not to consider the calorimeter contribution: the optimal value of α is 0.75, while using tracker isolation only ($\alpha = 0$, black curve) worsens the background rejection by a factor of about three.

In Figure 4.21 the parameter α is fixed at 0.75 and β varies in the range $[-1, 1]$. It is clear that negative values for β are to be preferred, which means that HCAL plays a dominant role in the background discrimination. This result is related to the particular background which we are optimizing against. Indeed, in the $Z_{\mu t}$ sample, background comes mainly from picking up randomly a charged hadron track. The large hadronic calorimeter contribution in this optimization can be interpret as a content in I of "muon identification" in the calorimeters of the track muon candidate, rejecting track from charged hardons by using the Hcal deposit.

Figure 4.22 shows the distribution of the optimized isolation I for the least isolated muon candidate in the di-muon pairs reconstructed in Z signal and W background events. The same distribution for the standard tracker isolation I_{trk} is also shown.

The background distribution is quite uniform in both plots, while the signal tends to be more peaked at low values of I, leading to a better discrimination

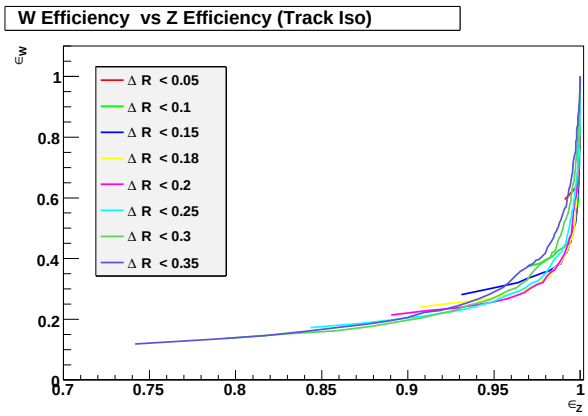

(a) I_{trk}

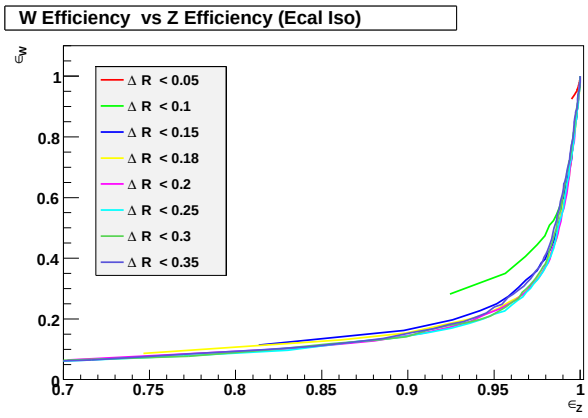

(b) I_{Ecal}

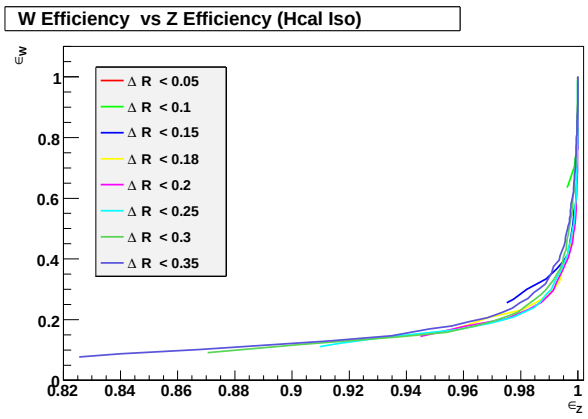

(c) I_{Hcal}

Figure 4.19: $W_{\mu\nu}$ background efficiency vs $Z_{\mu\mu}$ signal efficiency for selection cuts on the variables I_{trk}, I_{Ecal}, I_{Hcal}, at different fixed cone sizes, after having fixed the thresholds at $p_t > 1GeV/c$, $E_t^{Ecal} > 0.2GeV$, $E_t^{Hcal} > 0.5GeV$.

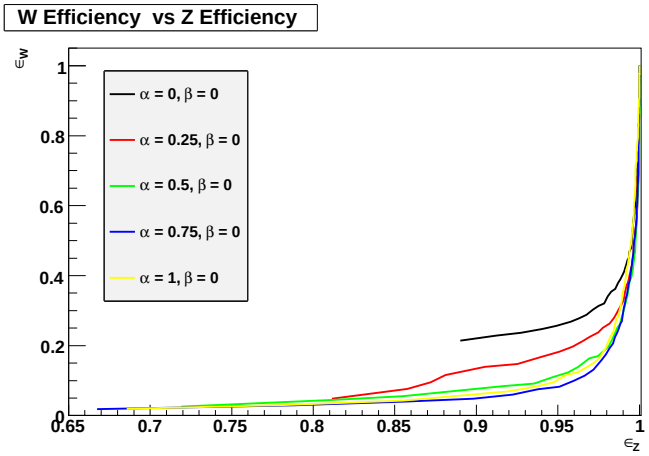

Figure 4.20: $W_{\mu\nu}$ background efficiency vs $Z_{\mu\mu}$ signal efficiency applying a selection on the linear combination of tracker and calorimeters isolation from Eq 4.18, for α values into the range $[0, 1]$. No asymmetry ($\beta = 0$) is assumed between I_{Ecal} and I_{Hcal} isolation.

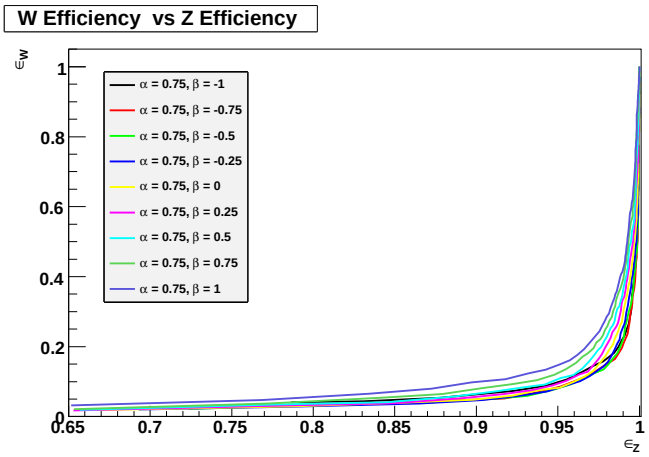

Figure 4.21: $W_{\mu\nu}$ background efficiency vs $Z_{\mu\mu}$ signal efficiency applying a selection on the linear combination of tracker and calorimeters isolation from Eq 4.18, for β values into the range $[-1, 1]$. The parameter α is fixed at the optimal 0.75 value.

between signal and background than with I_{trk}. Moreover, the new isolation variable alows to achieve a better discrimination of signal from backgrounds in the region in which the amount of signal events is larger, i.e. for small values of isolation variable.

4.3.3 Study of the isolation cut

The next step, after the optimization of the isolation performance curve, is the choice of the isolation cut, i.e. the upper value of the isolation variable which defines a muon to be isolated. The adopted procedure consists of changing the isolation cut in a range from $I_{cut} = 0.5$ to $I_{cut} = 2.5$ and performing the fit for all these intermediate cases. The background amount in the samples, in particular in $Z_{\mu t}$ but also in $Z_{\mu\mu}^{non\ iso}$ categories, reduces by lowering the isolation cut value, as in Figures 4.23 and 4.24.

The isolation efficiency improves by increasing of the cut value (Figure 4.25a). Infact, a larger value of isolation cut preservates signal events resulting in an increase of isolation efficiency.

Figure 4.25b shows how the error on ϵ_{sa}, measured by the fit, varies with isolation cut. It decreses with reducing the cut value until it achieves a plateau around and isolation cut $I_{cut} = 1.5$.

From these observations, we choose the cut value $I_{cut} = 1.5$ for our analysis in order to obtain an high isolation efficiency and a reduced error on standalone efficiency.

4.3.4 Relative isolation

We have performed the above optimization procedure also for the relative isolation variables, defined as I_k/p_t^{μ}, where I_k can be tracker or calorimeter isolation. The results of threshold and cone size optimizations are summarized in Table 4.6 and compared with values for absolute isolation. The only difference is that for relative isolation larger cone sizes (0.35) are preferable. No gain in background discrimination is observed by using the relative isolation rather than the absolute one (see Figure 4.26).

Nevertheless if, we consider the relative isolation variable, the distribution of the isolation efficiency with respect to p_T shows a decrease for values of muon p_T below 40 GeV/c (Figure 4.27), that is, instead, constant if we consider the absolute isolation as in Figure 4.28.

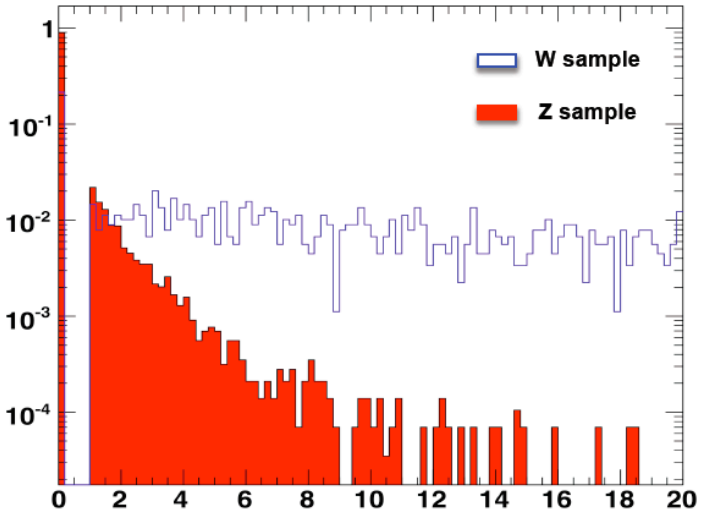

(a)

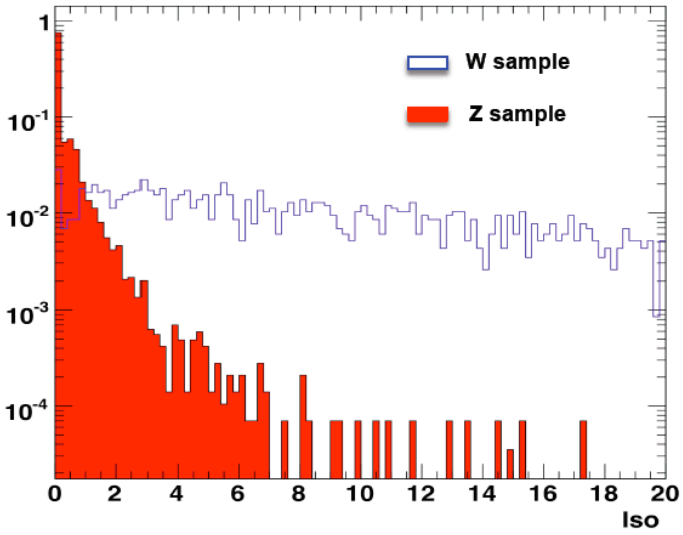

(b)

Figure 4.22: Standard isolation distribution (top plot) and optimized isolation distribution (bottom plot) for the least isolated muon candidate of the global muon plus track di-muon pair, where either both muon candidates come from a Z decay (red histogram) or one of the two comes from a W decay (white histogram).

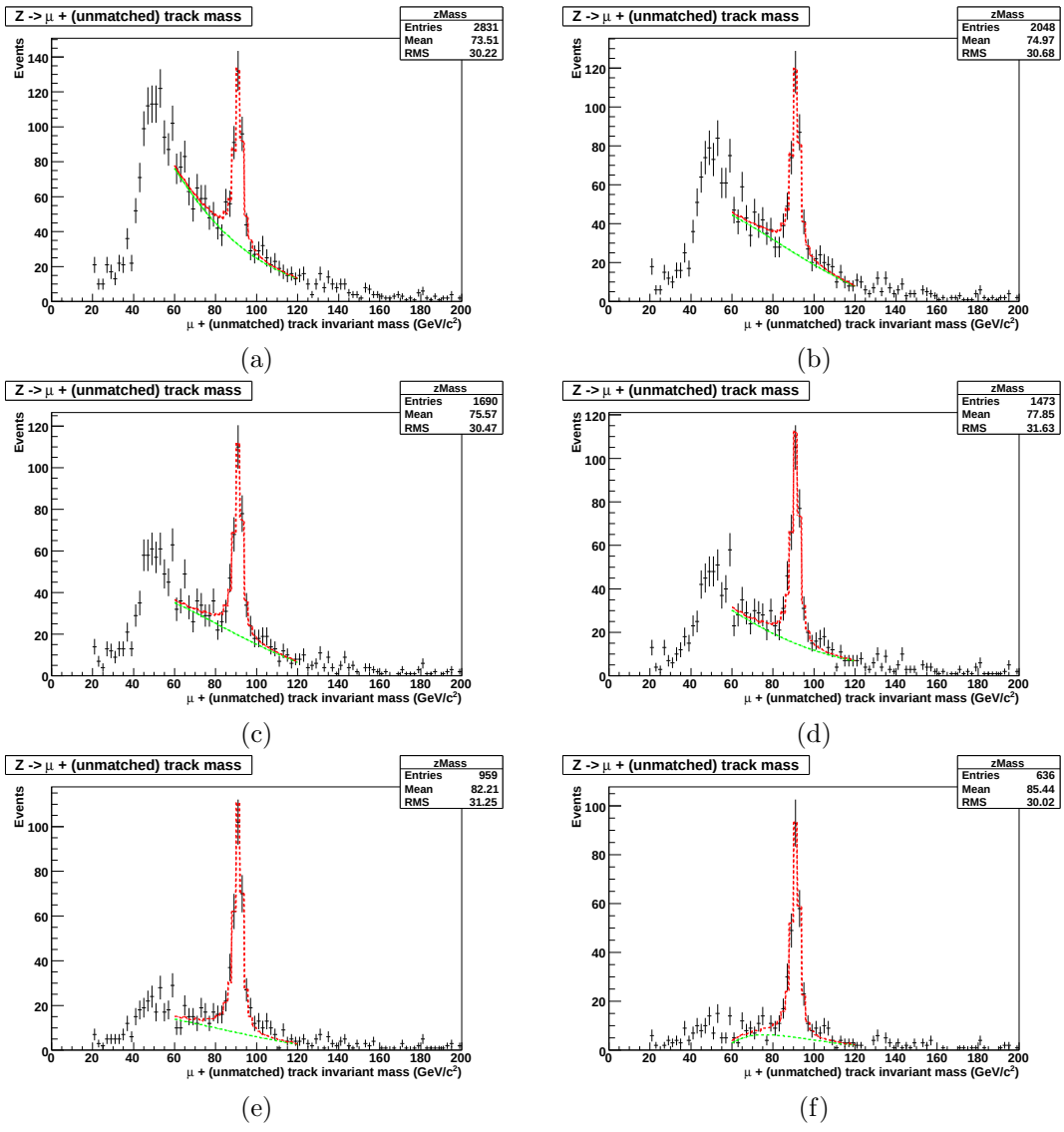

Figure 4.23: The invariant mass distribution of the muon pairs in the category $Z_{\mu t}$ for different isolation cut vaues from $I_{cut} = 2.5$, at the top-left corner, to $I_{cut} = 0.5$ at the bottom-right corner.

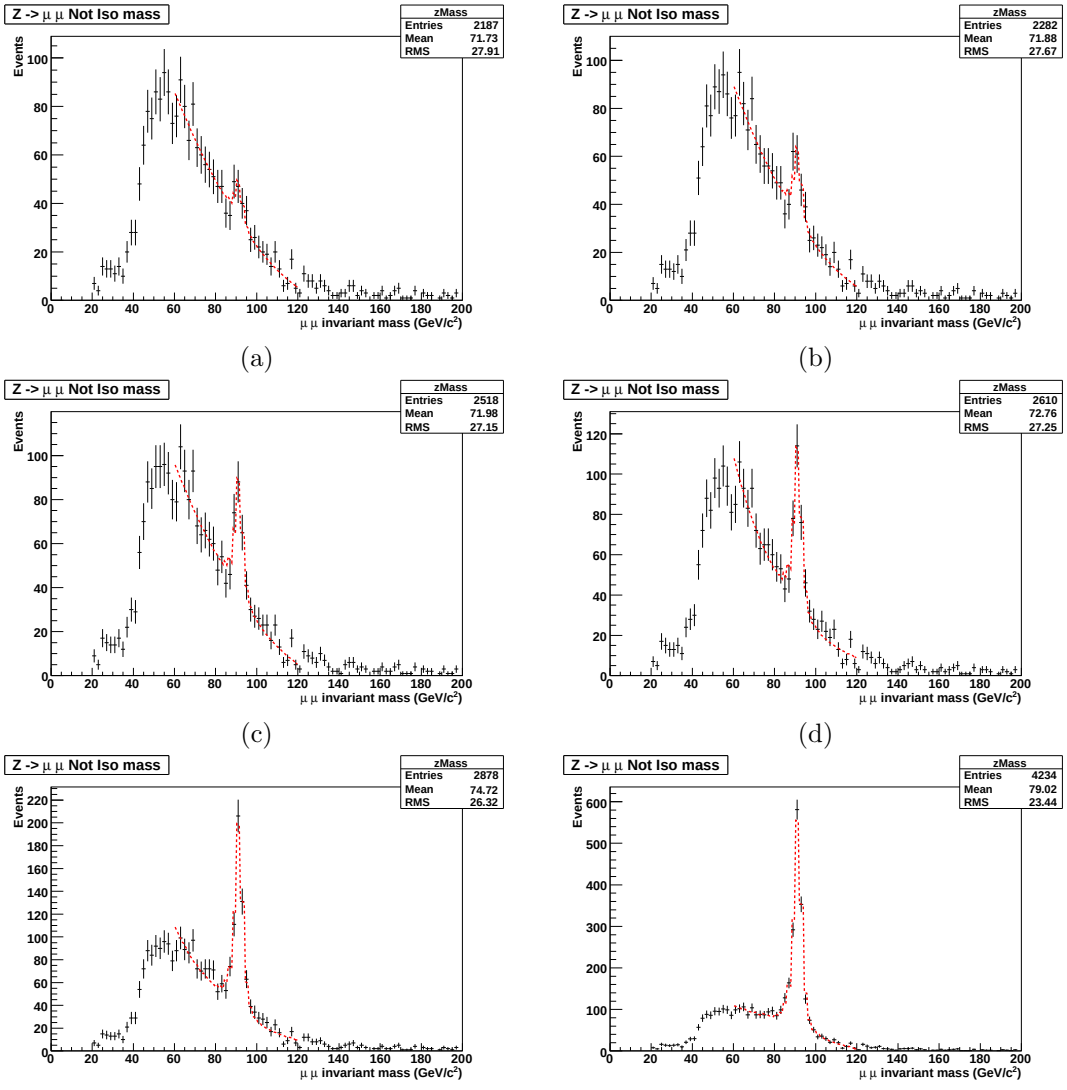

Figure 4.24: The invariant mass distribution of the muon pairs in the category $Z_{\mu\mu}^{non\ iso}$ for different isolation cut vaues from $I_{cut} = 2.5$, at the top-left corner, to $I_{cut} = 0.5$ at the bottom-right corner.

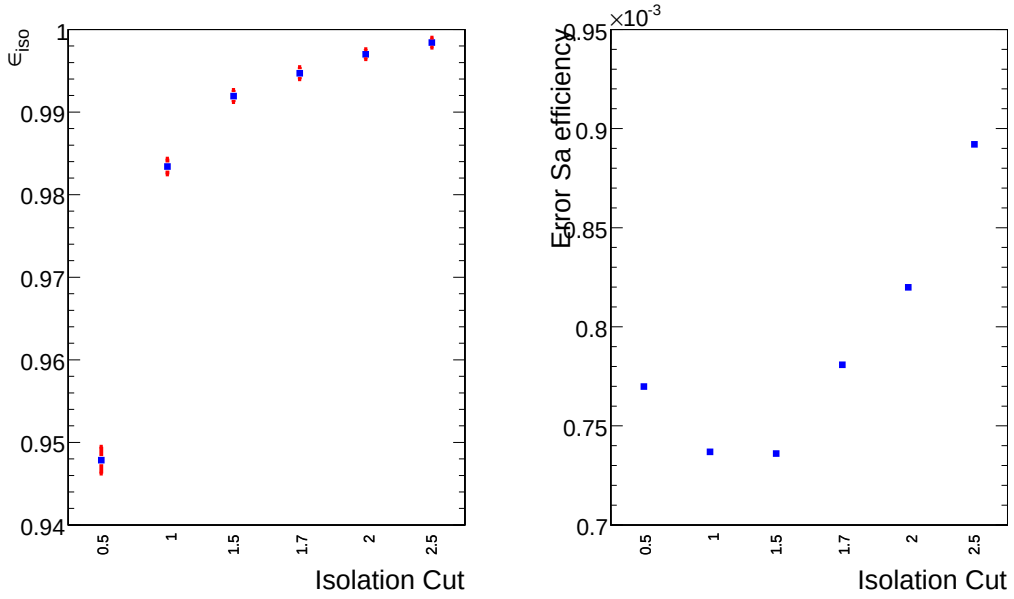

(a) (b)

Figure 4.25: Variation of isolation efficiency, ϵ_{iso} (Figure (a)) and of the error on ϵ_{sa} (Figure (b)), obtained by the fit procedure described in previous sections, as function of isolation cut. The cut values vary in the range $0.5 \div 2.5$.

cut variable		$p_{t,\mathrm{min}}$ (GeV/c) or $E_{t,\mathrm{min}}$ (GeV)	ΔR_{max}
Σp_t	Tracker	1	0.2
ΣE_t	Ecal	0.2	0.25
ΣE_t	Hcal	0.5	0.25
$\frac{\Sigma p_t}{p_t^\mu}$	Tracker	1	0.35
$\frac{\Sigma E_t}{p_t^\mu}$	Ecal	0.2	0.35
$\frac{\Sigma E_t}{p_t^\mu}$	Hcal	0.5	0.35

Table 4.6: Optimized values for p_t and E_t thresholds and for cone size for absolute and relative isolation variables.

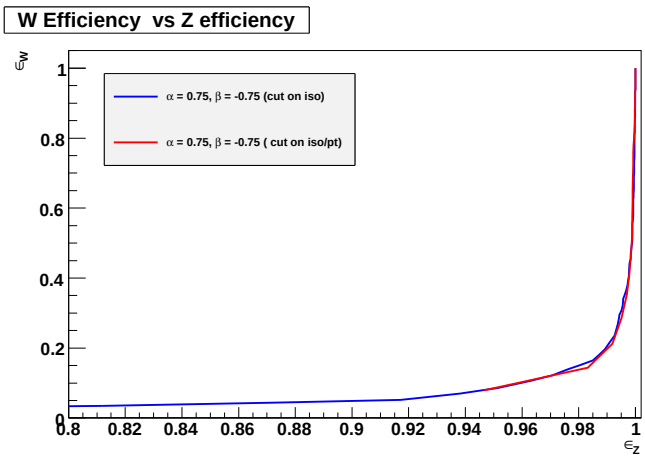

Figure 4.26: Comparison of $W_{\mu\nu}$ background efficiency vs $Z_{\mu\mu}$ signal efficiency for the combined absolute isolation and the combined relative isolation. There is no a significant prevalence of any of them.

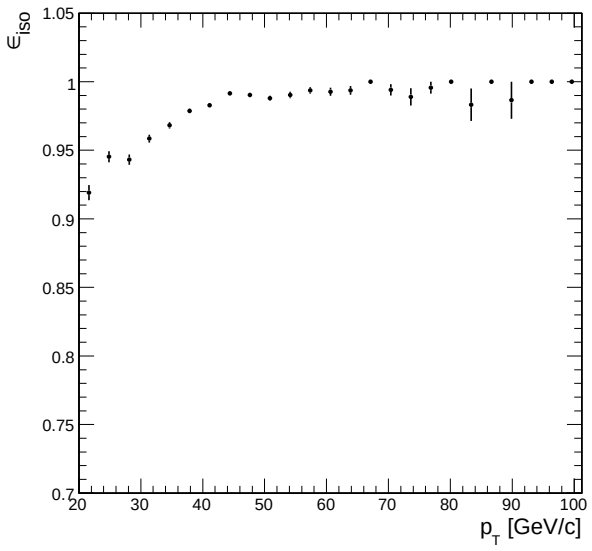

Figure 4.27: Isolation efficiency, for relative isolation selection, with respect to muon p_T.

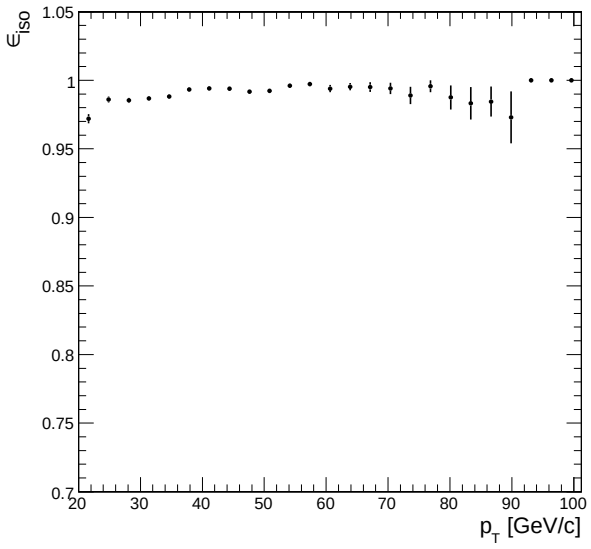

Figure 4.28: Isolation efficiency, for absolute isolation selection, with respect to muon p_T.

4.3.5 Fit results with new isolation

We performed the fit on samples of different luminosities, 5 pb^{-1}, 10 pb^{-1}, 45 pb^{-1} and 133 pb^{-1}, by applying the optimized absolute isolation selection and considering in the selection the isolation cut value chosen through the studies performed in the previous section, i.e Iso$_{cut}$ = 1.5. We report in Figures 4.29a to 4.29c the results of the fit superimposed to the di-muon invariant mass distributions of $Z_{\mu t}$, $Z_{\mu\mu}^{non\ iso}$ and $Z_{\mu s}$ categories for a sample of an equivalent integrated luminosity of 45 pb^{-1}. Comparison with the nominal fit is shown in Table 4.3.5 for all the samples considered. We can observe an increase of the estimated isolation efficiency, from 98.16% to 99.19%, about a percentage point. We have an improvement also on the relative error of ϵ_{iso}, which decreases from $\frac{\delta\epsilon_{iso}}{\epsilon_{iso}} = 0.12\%$ to $\frac{\delta\epsilon_{iso}}{\epsilon_{iso}} = 0.07\%$. as expected. The yield remains constant within the errors confirming the quality of the fit. At the same time, we have a gain in the statistical precision of the yield determination.

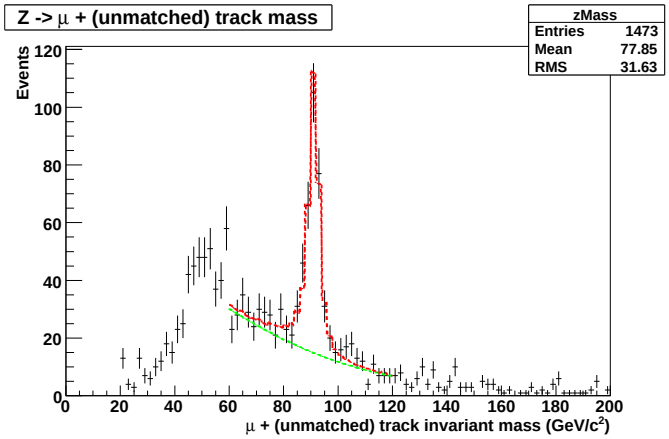

(a)

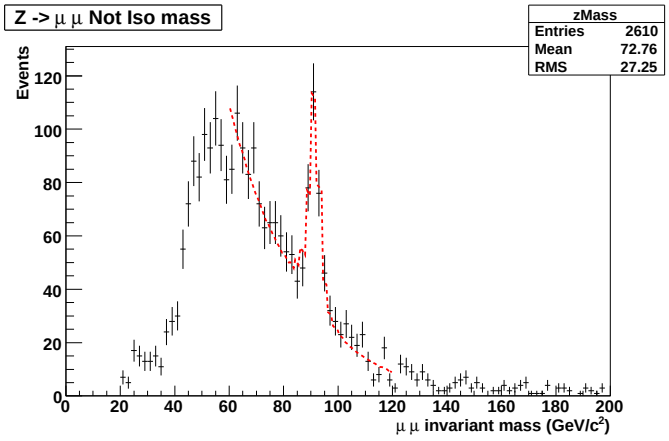

(b)

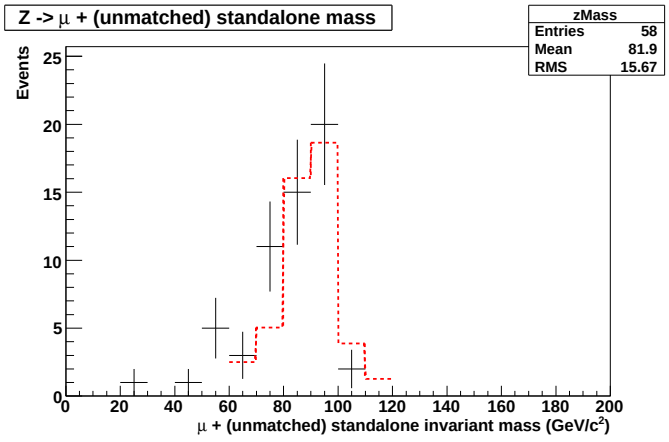

(c)

Figure 4.29: Fit curve superimposed to the invariant mass histogram of (a) $Z_{\mu t}$, (b) $Z_{\mu\mu}^{non\ iso}$ and (c) $Z_{\mu s}$ candidates for a sample corresponding to an integrated luminosity of 45 pb^{-1}. The selection has been made considering the optimized combined isolation variable studied in this section, and with $I < 1.5$.

	Tracker isolation	**Optimized isolation**
$\int \boldsymbol{L}\mathbf{d}\boldsymbol{t} = \mathbf{133pb^{-1}}$		
ϵ_{HLT}	0.915 ± 0.001	0.916 ± 0.001
ϵ_{iso}	0.9787 ± 0.0006	0.9923 ± 0.0004
ϵ_{sa}	0.9895 ± 0.0005	0.9896 ± 0.0004
ϵ_{trk}	0.99836 ± 0.00013	0.9990 ± 0.0001
$N_{\mathrm{Z}\to\mu^-\mu^+}$	50555 ± 234	50384 ± 229
χ^2/ndof	1.51032	1.17339
$\int \boldsymbol{L}\mathbf{d}\boldsymbol{t} = \mathbf{45pb^{-1}}$		
ϵ_{Hlt}	0.9161 ± 0.0017	0.9169 ± 0.0016
ϵ_{Iso}	0.9816 ± 0.0012	0.9919 ± 0.0007
ϵ_{Sa}	0.9899 ± 0.0008	0.9896 ± 0.0007
ϵ_{Trk}	0.9983 ± 0.0002	0.9984 ± 0.0002
$N_{Z\mu\mu}$	17000 ± 136	16964 ± 129
χ^2	1.03708	1.08624
$\int \boldsymbol{L}\mathbf{d}\boldsymbol{t} = \mathbf{10pb^{-1}}$		
ϵ_{HLT}	0.913 ± 0.004	0.915 ± 0.003
ϵ_{iso}	0.982 ± 0.002	0.9934 ± 0.0011
ϵ_{sa}	0.9895 ± 0.0017	0.9885 ± 0.0009
ϵ_{trk}	0.9978 ± 0.0007	0.9985 ± 0.0005
$N_{\mathrm{Z}\to\mu^-\mu^+}$	3811 ± 64	3798 ± 62
χ^2/ndof	1.4888	0.993955
$\int \boldsymbol{L}\mathbf{d}\boldsymbol{t} = \mathbf{5pb^{-1}}$		
ϵ_{HLT}	0.908 ±0.005	0.911 ±0.005
ϵ_{iso}	0.986± 0.003	0.993± 0.002
ϵ_{sa}	0.991 ± 0.002	0.992 ± 0.002
ϵ_{trk}	0.9970 ± 0.0011	0.9979 ± 0.0009
$N_{\mathrm{Z}\to\mu^-\mu^+}$	1894± 45	1883± 44
χ^2/ndof	1.0186	1.0545

Table 4.7: Comparison between fit results on data samples selected by applying the tracker isolation ($I < 3$ GeV/c) and the optimized isolation ($I < 1.5$). The input data samples are equivalent to an integrated luminosity of 133, 45, 10 and 5 pb^{-1}.

4.4 Extended Unbinned Maximum Likelihood

The $Z_{\mu s}$ sample is characterized by a low statistics and with a few inverse picobarns of integrated luminosity it could be quite difficult to perform a global χ^2 fit on the data of this sample. For the very first LHC data-taking an useful alternative could be to perform an *Unbinned Maximum Likelihood* fit, more performing in case of low statistics. This method consists in evaluating the *likelihood* function, $L(\boldsymbol{\theta})$, and in maximazing it. If we consider a random variable x, distributed according to the probability density function $f(x;\boldsymbol{\theta})$, where $\boldsymbol{\theta}$ are the unknown parameters of the theory, given a set of observations of the variable $(x_1, ..., x_n)$, i.e. our data sample, the likelihood function is defined as:

$$L(\boldsymbol{\theta}) = \prod_{i=0}^{n} f(x_i;\boldsymbol{\theta}) \ . \tag{4.19}$$

If the number of observation n is itself a result of the experiment, it is more convenient to perform and *Extended Maximum Likelihood Method* (EMLM), like in this case. The number of observations in the experiment is a Poisson random variable with mean value μ. The likelihood function is defined as the product of the probability of observing a data sample of n events (a Poisson probability) and the x-distribution:

$$L(\mu,\boldsymbol{\theta}) = \frac{\mu^n}{n!}e^{-\mu}\prod_{i=0}^{n} f(x_i;\boldsymbol{\theta}) = \frac{e^{-\mu}}{n!}\prod_{i=0}^{n}\mu f(x_i;\boldsymbol{\theta}) \ . \tag{4.20}$$

The number of observations n is given by:

$$n = N_{\mu s} + N^b_{\mu s} \ , \tag{4.21}$$

where $N_{\mu s}$ has been previously defined in (4.9) and $N^b_{\mu s}$ has been already introduced in Section 4.2.2.

The probability density function, pdf, according to which the x-variable is distributed is:

$$f(x_i;\boldsymbol{\theta}) = N_{\mu s} f^s_{peak} + b_{\mu s} \ , \tag{4.22}$$

in which f^s_{peak} and $b_{\mu s}$ have been already defined in Section 4.2.1.

It is more convenient to consider the logarithm of the likelihood function and minimize $-\ln L(\mu,\boldsymbol{\theta})$, remembering that $-2\ln L(\mu,\boldsymbol{\theta}) = \chi^2$ up to a constant additive term. Moreover, it is related to the variance according to:

$$V(\hat{\mu},\hat{\boldsymbol{\theta}}) = -\left(\frac{\partial^2 \ln L}{\partial\theta^2}\right)^{-1}\Bigg|_{\boldsymbol{\theta}=\hat{\boldsymbol{\theta}}} . \tag{4.23}$$

In this thesis an Unbinned Extended Maximum Likelihood method has been included in order to fit the event distribution in $Z_{\mu s}$ category, simultaneously to the binned χ^2 fit to the other samples by minimizing the following negative log-likelihood function:

$$\begin{aligned} -2\ln L \;=\; & \frac{(N_{\mu\mu}^{2HLT} - N_{\mathrm{Z}\to\mu^-\mu^+}\epsilon_{HLT}^2\epsilon_{iso}^2\epsilon_{trk}^2\epsilon_{sa}^2)^2}{N_{\mu\mu}^{2HLT}} + \\ & \frac{(N_{\mu\mu}^{1HLT} - 2N_{\mathrm{Z}\to\mu^-\mu^+}\epsilon_{HLT}(1-\epsilon_{HLT})\epsilon_{iso}^2\epsilon_{trk}^2\epsilon_{sa}^2)^2}{N_{\mu\mu}^{1HLT}} + \\ & \chi_{\mu t}^2 + \chi_{\mu\mu}^{non\ iso\ 2} - 2\ln L_{\mu s}\ . \end{aligned}$$

Table 4.8 reports the results of the combined $\chi^2 - likelihood$ fit performed on a data sample of integrated luminosity of 5 pb^{-1} and 10 pb^{-1} . Figures 4.30a and 4.30b shows the fit results superimposed to the invariant mass distribution of the Z candidates reconstructed in $Z_{\mu s}$ category, for the two data samples. This kind of fit allows to have a robust fit also with a few statistics, and the results are not worse than ones obtained with a χ^2 fit.

	$\int \boldsymbol{L}\mathbf{dt} = \mathbf{5pb^{-1}}$	$\int \boldsymbol{L}\mathbf{dt} = \mathbf{10pb^{-1}}$
ϵ_{HLT}	0.910 ± 0.005	0.915 ±0.003
ϵ_{iso}	0.988 ± 0.002	0.9922 ±0.0014
ϵ_{sa}	0.993 ± 0.002	0.9902 ±0.0016
ϵ_{trk}	0.998 ±0.0008	0.9986 ±0.0004
$N_{\mathrm{Z}\to\mu^-\mu^+}$	1896 ± 45	3794 ± 63

Table 4.8: Fit results of combined $\chi^2 - likelihood$ fit performed on a sample corresponding to an integrated luminosity of 5pb^{-1} and 10pb^{-1}.

4.5 Cross section results and comparisons

The $Z \to \mu^-\mu^+$ yield extracted from the fit is already corrected by the reconstruction efficiencies in the tracker and in the muon system, and by the isolation and HLT efficiencies. We can measure the inclusive cross section for the pp $\to$ Z + $X \to \mu^-\mu^+ + X$ process according to this relation:

$$\sigma = \frac{N_{\mathrm{Z}\to\mu^-\mu^+}}{\epsilon_{kin}\mathcal{L}}\ . \tag{4.24}$$

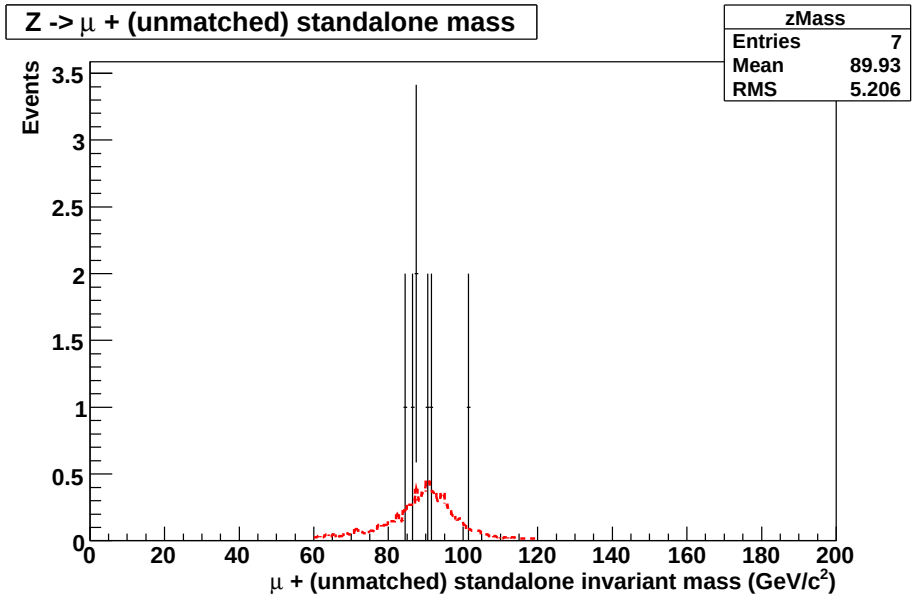

(a) 5 pb^{-1}

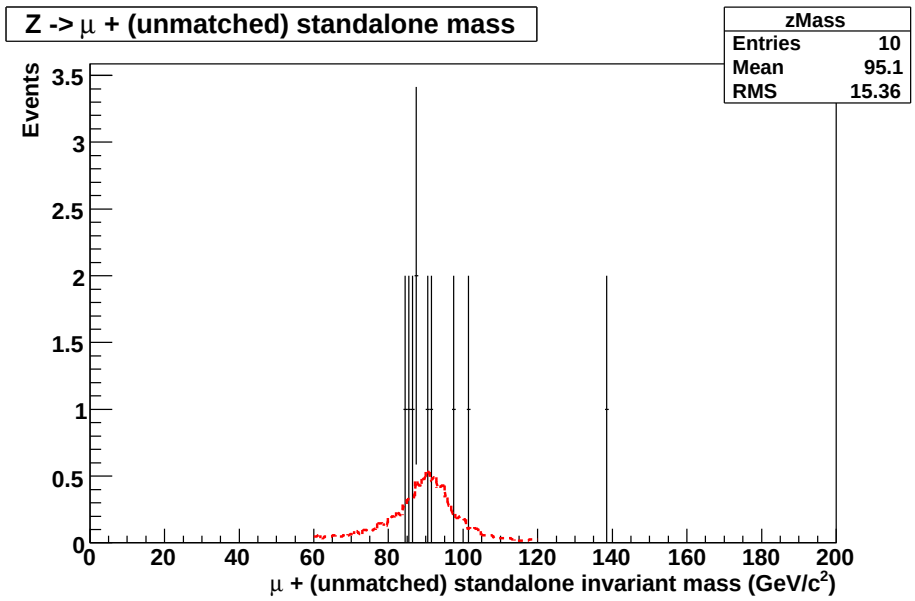

(b) 10 pb^{-1}

Figure 4.30: Combined $chi^2 - likelihood$ fit superimposed to the invariant mass distribution of $Z_{\mu s}$ candidates for a sample corresponding to an integrated luminosity of 5 pb^{-1}, Figure (a), and of 10 pb^{-1}, Figure (a).

In this relation the term ϵ_{kin} refers to the kinematic acceptance of the kinematic selection applied in our analysis; it is the fraction of Z events passing the kinematic selection. It has been evaluated with Monte Carlo[67]:

$$\epsilon_{kin} = 0.6027 \pm 0.0050 \ . \tag{4.25}$$

$\mathcal{L}$ is the integrated luminosity:

$$\mathcal{L} = \int L \mathrm{d}t \ . \tag{4.26}$$

Using the results of the fit performed considering the standard isolation in our selection, i.e. only the tracker isolation, for an integrated luminosity of 45 pb^{-1}, we obtain the following value for cross section measurement:

$$\sigma = 626.8 \pm 5.9 \text{ pb} \ . \tag{4.27}$$

Considering the parameters fitted on a data sample selected with a requirement on the new isolation variable (introduced in Section 4.3), the cross section measurement is:

$$\sigma = 625.5 \pm 5.7 \text{ pb} \ . \tag{4.28}$$

The value of generator cross section, already scaled for the generator efficiency, is 627,1. Therefore the values obtained in this work are in good agreement with the expected value within 1σ.

4.6 Updates and improvements

The method presented in this thesis aim at extracting the parameters of interest, such as the Z yield production, the reconstruction efficiencies and also the isolation and HLT selection efficiencies entirely from the data avoiding extimates affected by MC uncertinties not from MonteCarlo. This allows to reduce the sources of systematic errors in our analysis. The unique parameter that is still extracted from the Monte Carlo is the kinematic efficiency, ϵ_{kin}, that has been used to evaluate the cross section of the process analyzed in this work. It measures the percentage of Z events passing the kinematic and geometric selection. A method to evaluate the contribution of the systemic error due to Monte Carlo is to use different Monte Carlo generators and look at the different efficiency, ϵ_{kin} studies. A study now in progress is studying kinematic efficiency estimates using data sample generated with Pythia6 and MC@NLO. The former generates events at LO, while the latter generates at

NLO. Figure 4.31 shows how the rapidity distribution of on shell Z bosons at the LHC changes at LO, NLO and NNLO (Next-toNext-to-Leading-Order). There is an evident difference between to consider LO and NLO or NNLO. The study on the variation of ϵ_{kin} as a function of the used generator can help us to estimate the systematic error introduced in the analysis by refering to the Monte Carlo for the evaluation of this parameter.

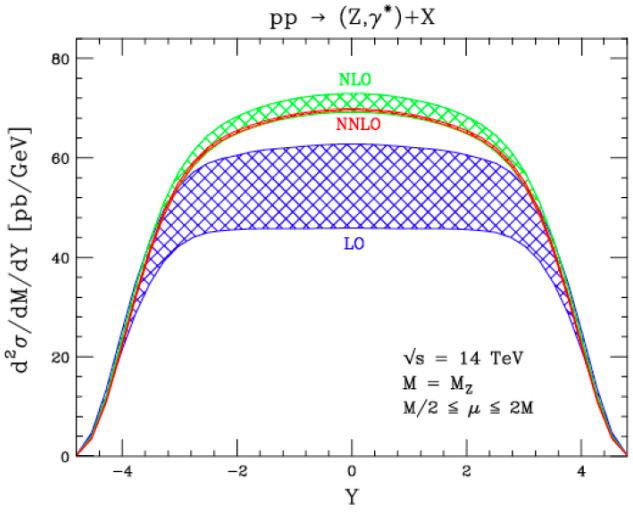

Figure 4.31: Rapidity distribution of on shell Z bosons at LO, NLO and NNLO[69].

Another source of systematic error is the empirical knowledge of the Parton Distribution Function. The PDFs at LHC design energy have been extrapolated from the measurement obtained by CD0 experiment at Tevatron at $\sqrt{s} = 2$ TeV. The uncertainties on the PDFs are source of systematic error. Studies are in program to evaluate quantitatively this effects.

Conclusions

This thesis has presented a study of the inclusive process $pp \rightarrow Z + X \rightarrow \mu^+\mu^- + X$ with the CMS detector at LHC at a centre of mass energy of $\sqrt{s} = 10$ TeV, which will be the initial LHC luminosity. The Z production, with subsequent decay in two muons, has a large cross section, ≈ 2 nb, and it will be studied already with the first data taken at the LHC, thanks also to its very clear signature: two muons in the final state isolated and high-p_T with an invariant mass consistent with the Z boson mass. The machine startup is foreseen for the October 2009.

The analyzed channel is very interesting because it will allow to calibrate the detector, already from the startup of the machine, and to monitor the LHC collider luminosity during all the period of activity. Furthermore it will be very important in the detection of new physics events of new physics characterized by two muons with invariant mass peaking at a given mass resonance.

The originality of the work of this thesis has consisted in completing the development of an entirely data-driven analysis method in collaboration with the CMS Naples analysis group for the first phase of LHC data-taking in which only few inverse picobarns of data will be available. The analysis method presented will allow to measure the yield of signal events and reconstruction efficiencies directly from data, without assumption from Monte Carlo, resulting in a reduction of systematic uncertainties. In Chapter 4 we have described in detail the analysis strategy and the results of a test on the official simulated data samples.

A preliminar study has been performed on the signal sample in order to understand the kinematics of the simulated Z and of two muons in which it decays (Section 4.1). The reconstructed Z are classified in five categories and the yield of each sample is related in different ways to the tracker and muon detector efficiency, and the isolation and HLT efficiencies (Section 4.2.1). The Z peak shape for each category is extracted directly from the data. In particular a different Z peak shape model has been implemented within this work for the last category , where one on the muons is associated to a track

in the tracker, and the other one is a global muon, associated to a track in the tracker and also in the muon detector. The fit results performed with a binned χ^2 have been successful (Section 4.2.5), confirming the goodness of the model.

In order to further reject the background a new combined isolation variable, combining tracker and calorimeters informations, has been investigated and optimized (Section 4.3). We have demonstrated that an event selection including a cut on this variable achieves a larger background rejection, with larger signal efficiency and a reduction of statistical error of the fitted yield (Table 4.3.5).

An Extended Unbinned Maximum Likelihood has been implemented in order to perform a robust fit also on samples of very low statistics (Section 4.4).

A cross section estimate has been obtained considering the fitted yield, the known integrated luminosity of the sample and also the kinematic efficiency, ϵ_{kin} (Section 4.5). This last term is the unique parameter of this analysis known from Monte Carlo. The result is in very good agreement with the expected generator cross section.

A study of systematic uncertainties introduced by the parameter extimated by the Monte Carlo is in progress. Another source of systematic error is the empirical knowledge of the Parton Distribution Function. Studies to evaluate quantitatively these effects are in program.

The work presented in this thesis has been included in a CMS internal note[67] officially accepted by the collaboration[68]. In particular the studies on muon isolation have been presented in a meeting of the electroweak muon group. The full procedures to obtain a cross section measurement with first CMS data will be ready at LHC start-up.

Acknowledgements

In conclusion of this work I would like to thank all those who have accompained me and encouraged during this journey. Without all of them this work wouldn't have seen the end.

I thank all the members of the CMS group of Naples to have welcomed me.

I want to thank professor Sciacca for giving me the opportunity to do this experience and for allowing me to benefit from his teachings.

I am grateful to dr.Luca Lista to have been my guide by offering me a chance to learn a lot from his expertise. Thank to him for the patience with which he answered all my questions and helped in every moment. It was a pleasure for me to collaborate with him.

I also would like to thank dr.Francesco Fabozzi for the support he offered me in solving physical and technical problems from the begin of this work and dr.Davide Piccolo for his attention to all my graphs and results, I thank him for all his suggestions. A thank to dr.Pierluigi Paolucci to have welcomed me in the CMS group of Naples.

I am thankful to dr.Pasquale Noli for the support he provided me from my first days in this group.

I cannot forget all my friends who lived with me the happiest and hardest days of this period. In particular I want to thank two dear friends with whome I shared joies and pains in this years. A thank to Tina for the strong support she provided me during the last nineteen years, for all the time we enjoyed and for all the times we studied together. And thanks to Antonella, for having spent a lot of time with me at university, always with a word of encouragment.

My deepest gratitude is to my parents, Nicoletta and Claudio, and to my brother, Ferdinando. With their love they have supported and encouraged me throught my life and given me the possibility to follow my dreams and take my way.

At last, but not the least, a special thank is for the person who has always believed in me, and who has been by my side during the most difficult moments, making me smile when I needed, and sharing with me this journey

making it pleasant.

Bibliography

[1] F. J. Hasert et al., *Observation of Neutrino-like Interactions without Muon or Electron in the Gargamelle Neutrino Experiment.* Phys. Lett. B 46 138 (1973).

[2] UA1 Collaboration, CERN, *Experimental observation of isolated large transverse energy electrons with associated missing energy at* $\sqrt{s} = 540$ *GeV*, Phys. Lett. B 122 (1983).

[3] S.Glashow, Nucl. Phys. 22 579 (1961).

[4] S.Weinberg, Phys. Rev. Lett. 19 1264 (1967).

[5] A.Salam, *Elementary particle Theory* , Ed. N. Svarholm (1968).

[6] I. Aitchison, A. Hey, Gauge theories in particle physics, Volume I:

[7] I. Aitchison, A. Hey, *Gauge theories in particle physics, Volume II: QCD and the Electroweak Theory*, third edition (2004).

[8] F.Halzen, A.Martin, *Quarks and Leptons, an introductory course in modern particle physics*, J.Wiley Sons (1984).

[9] Particle Data Group, homepage: http://www.pdg.lbl.gov/

[10] Peter Higgs, *Broken Symmetries and the Masses of Gauge Bosons.* Phys. Rev. Lett.3 13, 508 (1964).

[11] W. Pauli, *Rapp.Septime Conseil Phys.Solvay, Brussels 1993* (1934), reprinted in Winter (2000), pp 7,8.

[12] C. S. Wu et al, *Experiment Test of Parity Conservation in Beta Decay* Phys. Rev. Lett. 105, 1413-1415 (1957).

[13] The LEP collaborations, ALEPH, DELPH, L3, OPAL and the LEP W Working Group, LEPEWWG/MASS/2001-02-July 11, 2001, accessible at http://lepewwg.web.cern.ch/LEPEWWG/lepww/mw/Summer01/.

[14] CDF and D0 collaborations, *Tevatron Electroweak Working Group*, http://tevewwg.fnal.gov/wz/

[15] N. Cabibbo, *Unitary Symmetry and Leptonic Decays*, Phys. Rev. Lett., 10(12)531533 (June 1963).

[16] M. Kobayashi and K. Maskawa, *CP-Violation in the Renormalizable Theory of Weak Interaction*, Prog. Theor. Phys., 49(2)65265 (February 1973).

[17] C.N. Yang and R. Mills, *Conservation of Isotopic Spin and Isotopic Gauge Invariance*, Phys. Rev. 96,191 (1954).

[18] A.Djouadi, *The Anatomy of Electro-Weak Symmetry Breaking. I: The Higgs boson in the Standard Model.* Phys.Rept.457 1-216 (2005)

[19] DO Collaboration, Nature 429 (2004) 638

[20] CDF and D0 Collaborations, *Combined CDF and D0 Upper Limits on Standard Model Higgs-Boson Production with up to 4.2 fb^{-1} of Data*, Fermilab-Pub-09-060-E (March 13, 2009).

[21] D.J. Gross, F. Wilczek, Phys. Rev. Lett. 30 1343, (1973).

[22] H.D. Politzer, Phys. Rev. Lett. 30 1346, (1973).

[23] C.Bacci, G. Penso, G. Salvini, B. Stella, R. Baldini-Celio, G. Capon, C.Mencuccini, G.P. Murtas, A. Reale, M.Spinetti (gruppo gg), *Multi-hadronic cross-sections from e+e annihilation at c.m. energies between 1.4 and 2.4 GeV*, Phys.Lett.B38:551-554 (1972).

[24] F. Ceradini, R. Santonico, M. Conversi, L.Paoluzi, M. Grilli, E. Iarocci, P. Spillantini, V. Valente, R. Visentin, M. Nigro, (gruppo mp), *Multiplicity in hadron production by e+e colliding beams*, Phys.Lett.B42:501-503 (1972).

[25] B. Bartoli, B. Coluzzi, F. Felicetti, V. Silvestrini, G. Goggi, D. Scannicchio, G. Marini, F. Massa, F. Vanoli, (gruppo bosone), *Multiple particle production from e+e interactions at c.m. energies between 1.6 and 2 GeV*, Nuovo Cim.A70:615-631, (1970).

[26] M. Bernardini, D. Bollini, P.L. Brunini, E. Fiorentino, T. Massam, L. Monari, F. Palmonari, F. Rimondi, A. Zichichi, (gruppo BCF), *The Energy Dependence of Sigma (e+e) Hadrons) in the Total Center-Of-Mass Energy Range 1.2-GeV to 3.0-GeV*, Phys.Lett.B51:200, (1974).

[27] G.Salvini, *Lurto elettronepositone e le nuove particelle*, Annuario Enciclopedia Scienza e Tecnica, Mondadori (1976).

[28] R. P. Feynman, *Proceedings of the 3rd Topical Conference on High Energy Collision of Hadrons*, Stony Brook, N. Y. (1969).

[29] *The LHC Project. LHC Design Report, Volume I: the LHC Main Ring. Technical Report* CERN-2004-003-V-1, CERN, Geneva, (2004) http://lhc.web.cern.ch/lhc .

[30] *The LHC Project. LHC Design Report, Volume II: The LHC Infrastructure and General Services. Technical Report* CERN-2004-003-V-2, CERN, Geneva, (2004).

[31] *The LHC Project. LHC Design Report, Volume III: The LHC Injector Chain. Technical Report* CERN-2004-003-V-3, CERN, Geneva, (2004).

[32] European Organization for Nuclear Research, http://public.web.cern.ch/public/.

[33] Large Electron-Positron Collider, http://greybook.cern.ch/.

[34] The Compact Muon solenoid, http://cms.web.cern.ch/cms/index.html.

[35] A Toroidal LHC Apparatus, http://atlas.ch/.

[36] The Large Hadron Collider beauty experiment, http://lhcb.web.cern.ch/lhcb/.

[37] A Large Ion Collider Experiment, http://lhcb.web.cern.ch/lhcb/.

[38] CMS collaboration, *CMS Physics Technical Design Report, Volum 1: Detector Performance and Software*, CERN/LHCC, IOP Publishing (February 2006).

[39] CMS collaboration, *CMS Physics Technical Design Report, Volum 2: Physics Perfomance*, CERN/LHCC, IOP Publishing (June 2007).

[40] The CMS Traker, http://cms-tracker.web.cern.ch/cms-tracker.

[41] The CMS Collaboration, *The CMS experiment at the CERN LHC*, JINST 3 S08004 (August 2008).

[42] The CMS Collaboration, *The CMS tracker system project : Technical Design Report* , CERN-LHCC-98-006 ; CMS-TDR-005. - Geneva : CERN (1997), http://cmsdoc.cern.ch/ftp/TDR/TRACKER/tracker_tdr_files.html.

[43] The CMS Collaboration, *The CMS electromagnetic calorimeter project : Technical Design Report* , CERN-LHCC-97-033 ; CMS-TDR-004. - Geneva : CERN (1997), http://cmsdoc.cern.ch/ftp/TDR/ECAL/ecal.html.

[44] The CMS Collaboration, *The CMS hadron calorimeter project : Technical Design Report* , CERN-LHCC-97-031 ; CMS-TDR-002. - Geneva : CERN (1997), http://cmsdoc.cern.ch/ftp/TDR/HCAL/hcal.html.

[45] Kuraray Co., Ltd, "Scintillation Materials", Japan www.icrr.u-tokyo.ac.jp/ tanimoto/t2k/2km-lr/fiber/PSFcatalog.pdf

[46] BICRON BC408 Polyvinyl toluene Plastic Scintillator, http://webh09.cern.ch/ajbell/Documents/Optical_Fibres/BICRON

[47] The CMS Collaboration, *The CMS muon project : Technical Design Report* , CERN-LHCC-97-032 ; CMS-TDR-003. - Geneva : CERN (1997), http://cmsdoc.cern.ch/ftp/TDR/MUON/muon.html.

[48] The CMS Collaboration, *The CMS magnet project : Technical Design Report* , CERN-LHCC-97-010 ; CMS-TDR-001. - Geneva : CERN (1997), http://cmsdoc.cern.ch/ftp/TDR/MAGNET/magnet.html.

[49] The CMS Collaboration, *CMS trigger and data-acquisistion project : Technical Design Report* , CERN-LHCC-2002-026 ; CMS-TDR-006-add-1. - Geneva : CERN (2002).

[50] *Proceedings of the Workshop on Monte Carlo's, Physics and Simulations at the LHC*, arXiv:0902.0293v1 [hep-ph], (February 2009).

[51] Particle Data Group, http://pdg.lbl.gov/2008/hadronic-xsections/hadron.html (COMPAS group, IHEP, Protvino, August 2005).

[52] S.D.Drell and T.M.Yan, *Massive Lepton-Pair Production in Hadron-Hadron Collisions at High Energies,* Phys.Rev.Lett. 25. 316 (1970).

[53] A. Djouadi, J. Kalinowski, M. Spira, *HDECAY: a Program for Higgs Boson Decays in the Standard Model and its Supersymmetric Extension*, arXiv:hep-ph/9704448v1, (1997).

[54] The CMS Collaboration, *Search Strategy for a Standard Model Higgs Boson Decaying to Two W Bosons in the Fully Leptonic Final State*, CMS PAS HIG-08-006 (January, 2009).

[55] The CMS Collaboration, *Search strategy for the Higgs boson in the ZZ* decaychannel with the CMS experiment*, CMS PAS HIG-08-003 (February, 2009).

[56] Stephen P. Martin, *A Supersymmetry Primer*, hep-ph/9709356 (December 2008).

[57] M. Cvetic and P. Langacker, *Implications of Abelian Extended Gauge StructuresFrom String Models*, Phys. Rev. D54 (1996) 35703579, arXiv:hep-ph/9511378.

[58] M. Cvetic and P. Langacker, *New Gauge Bosons from String Models*, Mod. Phys. Lett. A11 (1996) 12471262, arXiv:hep-ph/9602424.

[59] A. Leike, *The phenomenology of extra neutral gauge bosons*, Phys. Rept. 317 (1999) 143250, arXiv:hep-ph/9805494.

[60] C. T. Hill and E. H. Simmons, *Strong dynamics and electroweak symmetry breaking*, Phys. Rept. 381 (2003) 235402, arXiv:hep-ph/0203079.

[61] L. Randall and R. Sundrum, *An alternative to compactification*,Phys. Rev. Lett. 83(1999) 46904693. doi:10.1103/PhysRevLett.83.4690.

[62] L. Randall and R. Sundrum, *A large mass hierarchy from a small extra dimension*, Phys. Rev. Lett. 83 (1999) 33703373. doi:10.1103/PhysRevLett.83.3370.

[63] T. Han, H. Logan, B. McElrath, and L.-T. Wang, *Phenomenology of the little Higgs model*, Phys. Rev. D67 (2003) 095004. doi:10.1103/PhysRevD.67.095004.

[64] Electroweak page of Summer08 production, https://twiki.cern.ch/twiki/bin/view/CMS/TWikiEWKMCInfoSummer08.

[65] L. Lyons, *Statistics for nuclear and particle physicists*, Cambridge University Press (1999).

[66] G. Cowan, *Statistical Data Analysis*, Oxford (1998).

[67] A. de Cosa, M. de Gruttola, S. Di Guida, F. Fabozzi, L. Lista, P. Noli, *Determination of the* $pp \to Z + X \to \mu^-\mu^+ + X$ *inclusive cross section with a simultaneous fit of Z yield, muon reconstruction efficiencies and High Level Trigger efficiency*, CMS AN-2009/005.

[68] *Towards a measurement of the inclusive* $W \to \mu\nu$ *and* $Z \to \mu\mu$ *cross section in pp collisions at* $\sqrt{s} = 10$ *TeV*, CMS PAS-2009/001.

[69] Anastasiou et al., *High-precision QCD at hadron colliders: Electroweak gauge boson rapidity distributions at next-to-next-to leading order*, Physical Review D 69, 094008 (2004).